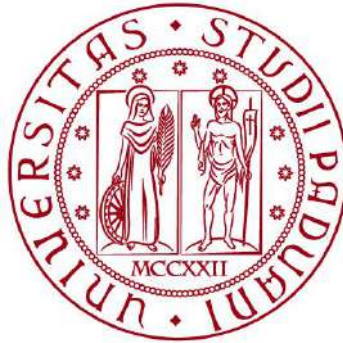


**UNIVERSITÀ DEGLI STUDI DI PADOVA**

*Department Of Civil, Environmental and Architectural Engineering*

Master`s Degree in Environmental Engineering



**MASTER THESIS**

**ANALYSIS OF REAL-TIME GNSS POSITIONING USING NRTK CORRECTIONS FROM VENETO REGION  
AND HEXAGON NETWORKS**

Supervisor: Prof. Massimo Fabris

Candidate:

Victorien Bienvenu Abanda Well  
2122320

**ACADEMIC YEAR 2024-2025**

## Table of contents

<b>1.</b>	<b>INTRODUCTION</b>	
		1
1.1.	Motivation of the work	1
1.2.	Objectives	2
1.3.	GNSS architecture	2
1.3.1.	GNSS Segments	3
1.3.2.	GNSS Signals	12
1.4.	GNSS augmentation systems	18
1.4.1.	Differential GPS	19
1.4.2.	Real Time Kinetics (RTK)	20
1.4.3.	Network Real-Time Kinematic (NRTK)	21
1.4.3.1.	HXGN SmartNet	22
1.5.	Post processing Method	24
1.6.	Classification of topographic method	25
1.6.1.	Geometric Levelling (From the middle)	25
1.6.2.	Total station	25
<b>2.</b>	<b>MATERIAL AND METHODS</b>	<b>27</b>
2.1.	Site presentation	27
2.2.	Material	28
2.2.1.	Instruments for classical topographic survey	28
2.2.2.	GPS survey equipment	29
2.3.	Method for survey	30
2.3.1.	Horizontal distance measurement	30
2.3.2.	Elevation measurement	31
2.3.3.	NRTK GNSS Survey for HXGN	31
2.3.4.	Veneto Region GNSS RTK network	32
2.3.5.	Description of the data	32
2.3.6.	Measurement calculations	34
2.3.7.	Performance evaluation and ranking	34
2.3.8.	Optimal utilization of the NRTK network	35
<b>3.</b>	<b>RESULTS AND DISCUSSION</b>	<b>36</b>
3.1.	Comment on the trend of each graphics	36
3.1.1.	Veneto R.	36
3.1.2.	HXGN trend	42
3.2.	Analysis of the performance between the different NRTK and ranking	70

3.2.1.	CQ1D performance and ranking .....	70
3.2.2.	CQ2D performance and ranking .....	72
3.2.3.	CQ3D performance and ranking .....	74
3.2.4.	Distance difference performance and ranking .....	76
3.2.5.	Elevation difference performance and ranking .....	79
3.3.	Optimization of the utilization of the NRTK network .....	81
4.	CONCLUSION .....	83
	Bibliography .....	85

## List of figures

Figure 1: GPS orbital planes ; Source: <a href="https://www.gps.gov/systems/gps/space/">https://www.gps.gov/systems/gps/space/</a> .....	5
Figure 2: Carrier phase errors; source: (Park et al., 2012) .....	13
Figure 3: Pseudo-range; source: (Im et al., 2013) .....	14
Figure 4: satellite orbit error; source: (Huang et al., 2025).....	16
Figure 5: Ionospheric delay error; source: (Imad et al., 2023) .....	17
Figure 6: Illustration of multipath error; source: (Lau, 2021).....	18
Figure 7: Illustration of Relative position Method; source: (Jamieson & Gillins, 2018).....	19
Figure 8: Illustration of differential GPS applied for sea level measurement; source: (Joseph, 2011) .....	20
Figure 9: Illustration of the transmission of the RTK functioning; source (Keshavarzi et al., 2021) .....	20
Figure 10: Partial view of the Veneto R.; source (Regione del Veneto, 2025) .....	24
Figure 11: Total station ; source : (Sofos et al., 2017).....	26
Figure 12: Presentation of Veneto Region; source: (VENETO R.INFO, 2025).....	27
Figure 13: Presentation of the site; source: (Google, 2025) .....	28
Figure 14: Total station used for the project.....	29
Figure 15: Smart antenna Leica viva GS16 in the field; source: Author and (Leica geosystems, 2021).....	30
Figure 16: Total station positioned at point 1000 (A); location of Point 2000 (B). .....	31
Figure 17: RTK GNSS antenna operating on the site .....	32
Figure 18: CQ values from epoch 1s to epoch 9s at point 1000.....	36
Figure 19: CQ values from epoch 1s to epoch 600s at point 1000.....	36
Figure 20: GDOP values from epochs 1s to epoch 9s.....	37
Figure 21: GDOP values from epochs 1s to epoch 600s.....	37
Figure 22: CQ values from epochs 1s to epoch 9s at point 2000 .....	38
Figure 23: CQ values from epochs 1s to epoch 600s at point 2000 .....	38
Figure 24: GDOP values from epochs 1s to epoch 9s.....	39
Figure 25: GDOP values from epochs 1s to epoch 600s.....	39
Figure 26: Distance difference between point 1000 and 2000 from Epoch 1s to 9s .....	40
Figure 27: Distance difference between point 1000 and 2000 from Epoch 1s to 600s .....	40
Figure 28: Distance difference between point 1000 and 2000 from Epoch 1s to 9s .....	41
Figure 29: Elevation difference between point 1000 and 2000 from Epoch 1s to 600s .....	41
Figure 30: CQ values at point 1000 on 19/03/2025 from Epoch 1s to 9s .....	43
Figure 31: CQ values at point 1000 on 19/03/2025 from Epoch 1s to 600s .....	43
Figure 32: GDOP values at point 1000 on 19/03/2025 from Epoch 1s to 9s .....	44
Figure 33: GDOP values at point 1000 on 19/03/2025 from Epoch 1s to 600s .....	45
Figure 34: CQ values at point 2000 on 24/03/2025 from Epoch 1s to 9s .....	46
Figure 35: CQ values at point 2000 on 24/03/2025 from Epoch 1s to 600s .....	46
Figure 36: GDOP values at point 2000 on 24/03/2025 from Epoch 1s to 9s .....	48
Figure 37: GDOP values at point 2000 on 24/03/2025 from Epoch 1s to 600s .....	48
Figure 38: Distance difference for HXGN as per the data collected on 19/03/2025 and 24/03/2025 from Epoch 1s to 9s.....	50
Figure 39: Distance difference for HXGN as per the data collected on 19/03/2025 and 24/03/2025 from Epoch 1s to 600s.....	51
Figure 40: elevation difference for HXGN as per the data collected on 19/03/2025 and 24/03/2025 from Epoch 1s to 9s.....	52
Figure 41: Elevation difference for HXGN as per the data collected on 19/03/2025 and 24/03/2025 from Epoch 1s to 9s.....	52
Figure 42: CQ values for HXGN as per 02/04/2025 measurements at point 1000 .....	53

Figure 43: CQ values for HXGN as per 02/04/2025 measurements at point 2000 .....	54
Figure 44: GDOP values for HXGN as per 02/04/2025 measurements at point 1000 .....	55
Figure 45: GDOP values for HXGN as per 02/04/2025 measurements at point 1000 .....	56
Figure 46: Distance difference for HXGN as per the data collected on 02/04/2025 from Epoch 1 second to 9 seconds .....	58
Figure 47: Elevation difference for HXGN as per the data collected on 2/4/2025 from Epoch 1s to 9s.....	59
Figure 48: CQ values for HXGN as per the data collected on 28/04/2025 from Epoch 1 second to 9 seconds at point 1000 .....	61
Figure 49: CQ values for HXGN as per the data collected on 28/04/2025 from Epoch 1 second to 9 seconds at point 2000 .....	63
Figure 50: GDOP values for HXGN as per the data collected on 28/04/2025 from Epoch 1 second to 9 seconds at point 1000 .....	65
Figure 51: GDOP values for HXGN as per the data collected on 28/04/2025 from Epoch 1 second to 9 seconds at point 2000 .....	66
Figure 52: Distance difference values for HXGN as per the data collected on 28/04/2025 from Epoch 1 second to 9 seconds .....	68
Figure 53: Elevation difference values for HXGN as per the data collected on 28/04/2025 from Epoch 1 second to 9 seconds .....	70
Figure 54: Box plot analysis of CQ1D measurements at point 1000 .....	71
Figure 55: Box plot analysis of CQ1D measurements at point 2000 .....	72
Figure 56: Box plot analysis of CQ2D measurements at point 1000 .....	73
Figure 57: Box plot analysis of CQ2D measurements at point 2000 .....	74
Figure 58: Box plot analysis of CQ3D measurements at point 1000 .....	75
Figure 59: Box plot of CQ3D at point 2000 .....	76
Figure 60: Box plot of distance difference in F32 .....	77
Figure 61: Box plot of distance difference F32 for Veneto R. and HXGN average values .....	77
Figure 62: Box plot of distance difference F12 .....	78
Figure 63: comparison of average values of HXGN and Veneto R. distance difference for F12 .....	79
Figure 64: Box plot of distance difference for F32 .....	80
Figure 65: Box plot of elevation difference for F12 .....	80

## List of tables

Table 1: Description of GPS constellation as per 11th April 2025.....	4
Table 2: Status of GALILEO Satellite constellation .....	6
Table 3: Location of the Veneto R. ....	23
Table 4: Summary of the data collected during this experiment.....	34
Table 5: Results of scalarization techniques.....	81

## **ACKNOWLEDGEMENT**

I would like to express my deepest gratitude to my mother, Bella Belinga Clementine Yvette, for instilling in me a love for learning and a strong faith in God; to my supervisor, Massimo Fabris, for his unwavering commitment and patience throughout this journey; to my entire family in Cameroon, whose love and support have been indispensable; to my friends from the Cameroonian community in Padova especially Dr. Francine Tchamaleu Pangop, Dan Azimi, Jordan Defo, Amang Francois Kisito, Gergino Chounna, and Dr. Joseph Fotso for their invaluable encouragement and support; to my Italian friends Lorenzo Berlese, Francesco Sanniti, Giacomo, Alessandro, and Nicolas, who greatly facilitated my integration; to my classmates, especially Asad Sandu, Anooja Faustine, Andrea Santaterra, Maddalena Crepaldi, Francesca, Carolina, Giulia Boscaro, Michele Gironimi, and Ilaria Prisco, for their support and camaraderie; and to the Christian communities of Chiesanuova, Monte Cengio, and the Eremitani, who brought me joy and helped sustain my faith during challenging times, with special thanks to Emilio Carraro, Stefania Greggio, Laura, Sonia, Adriano, Loretta, Giacomo, Caterina, Don Florindo, Don David, Don Giancarlo, Maria Gracia, and Don Lucio.

## ABSTRACT

This master's thesis evaluates the **performance of real-time GNSS positioning** using two Network **RTK (NRTK)** services: the Hexagon SmartNet GNSS RTK network and the Veneto Region GNSS RTK network. With the growing demand for **high-precision** positioning in sectors such as surveying, construction, and autonomous navigation, RTK has become an essential technique. However, its reliability is strongly influenced by environmental conditions, satellite geometry, and the configuration of reference station networks—particularly in areas with complex terrain or urban obstructions, such as the Veneto region.

The study compares the accuracy and consistency of the two networks by collecting positioning data at two sites in Padova. Traditional topographic methods, including total station surveys and geometric levelling, were employed to establish precise reference points.

Results show that **Hexagon SmartNet GNSS RTK network** generally offers superior stability and consistency, with lower median values and fewer outliers across Coordinate Quality (CQ) metrics (CQ1D, CQ2D, CQ3D) and Geometric Dilution of Precision (GDOP). While the **Veneto Region GNSS RTK network** delivered acceptable performance, it exhibited greater variability and occasional extreme deviations—particularly during early epochs and under challenging satellite geometry conditions. Interestingly, for distance and elevation differences, the Veneto Region GNSS RTK network outperformed Hexagon SmartNet GNSS RTK network, achieving its best distance precision at 360 seconds and best elevation precision at 6 seconds. In contrast, Hexagon SmartNet GNSS RTK network reached its minimum distance error at 5 seconds and minimum elevation error at 40 seconds. These findings suggest that the Veneto Region GNSS RTK network can offer superior precision in specific aspects, though not always with optimal time efficiency.

An optimal observation time of 7 seconds was identified as the best compromise between precision and temporal efficiency, based on scalarization methods ( $L_1$ ,  $L_2$ , and  $L_\infty$  norms). In conclusion, Hexagon SmartNet GNSS RTK network emerged as the more consistent and reliable network for applications requiring stable performance, while the Veneto Region GNSS RTK network represents a robust alternative—particularly when vertical accuracy is prioritized. Financial considerations also play a role, as the Veneto Region GNSS RTK network is free of charge, whereas Hexagon SmartNet GNSS RTK network requires an annual subscription of approximately €500.

**Keywords:** GNSS, NRTK, RTK, accuracy, performance

## 1. INTRODUCTION

### 1.1. Motivation of the work

The demand for high-precision positioning has grown significantly across various sectors, including surveying, construction, precision agriculture, autonomous navigation, and geospatial monitoring (W. Zhang et al., 2025). Network Real-Time Kinematic (NRTK) GNSS positioning has emerged as a leading technique capable of delivering centimeter-level accuracy in real time, making it indispensable for modern geospatial applications. A substantial body of literature demonstrates the effective application of NRTK in numerous engineering and transportation fields worldwide.

For instance, Pipitone et al. (2023) reports the use of NRTK for monitoring land subsidence, seismic activity, and volcanic deformation. NRTK has proven effective in tracking ground movements and soil subsidence over extended periods within stable reference frames, such as the North China Reference Frame 2016 (NChina16) (J. Yu & Wang, 2017). Similarly, Sánchez & Brunini (2009) highlight the use of NRTK to assess seismic-induced movements by analyzing the stability of the SIRGAS reference frame in Latin America. Murray & Svarc (2017) emphasize the importance of NRTK for precise positioning in dynamic environments, particularly for geological surveys involving GPS-based land subsidence monitoring.

In coastal and tectonically active regions, NRTK has also been applied to monitor plate motion and sea-level rise, as illustrated by J. Yu & Wang (2017) in the Gulf of Mexico. In the field of geotechnics, Glavačević et al., (2025) utilized NRTK to measure soil erosion across various Croatian regions, including Posedarje, Seline, the Santi Peninsula, Gully Santi, and the Metajna Peninsula. In agriculture, Radicioni et al. (2022) demonstrated the use of NRTK for machine control and guidance in Umbria (Italy), leveraging signals from both GPS and GLONASS constellations.

NRTK has also shown promise in water management and transportation infrastructure. (Y. Li et al., 2017) and (J. Yu et al., 2016) explored its effectiveness in monitoring dam deformation and bridge dynamics. Furthermore, Dardanelli & Maltese (2022) and Barreca et al. (2020) highlighted the role of Network RTK in enabling Mobile Mapping Systems (MMS) for evaluating terrain morphology, building conditions, and urban infrastructure in Palermo.

Despite its advantages, NRTK performance is highly sensitive to environmental conditions, satellite geometry, and the configuration of reference station networks. In regions with complex terrain or

urban obstructions—such as the Veneto region in northeastern Italy—these factors can significantly influence the reliability and accuracy of NRTK solutions Tavasci et al., (2024).

This thesis is motivated by the need to assess and compare the real-time positioning capabilities of different NRTK in the Veneto region. By analyzing their performance across multiple test sites, this study aims to provide practical insights into the strengths and limitations of each network. The findings will support infrastructure planning, enhance the reliability of GNSS-based services, and inform best practices for professionals and institutions relying on high-precision positioning in the region (Kizil & Tisor, 2011).

## **1.2. Objectives**

The primary objective of this study is to evaluate the performance and reliability of HEXAGON SmartNet GNSS RTK network (HXGN) and the Veneto Region GNSS RTK network (Veneto R.). The research aims to assess how effectively these networks deliver high-precision positioning under varying environmental and operational conditions. To achieve this, the study is guided by the following specific objectives:

- 1.To analyze the spatial coverage and infrastructure of HXGN and the Veneto R. across two sites located at Padova.
- 2.To acquire positioning data through HXGN and Veneto R.
- 3.To conduct field surveys using traditional topographic methods, including total station surveys and geometric levelling which provide highly precise positioning.
4. To evaluate the positioning accuracy and precision of NRTK GNSS solutions meaning HXGN and Veneto R.
5. To provide recommendations for optimizing NRTK GNSS usage in the Veneto Region, supporting both public authorities and private stakeholders in improving geospatial data acquisition and positioning workflows.

## **1.3. GNSS architecture**

GNSS consists of satellite navigation systems such as GPS, GLONASS, Galileo, and BeiDou, which offer continuous positioning services. GNSS can be categorized into three segments: the space segment, comprising the satellites; the control segment, encompassing all data processing

operations; and the user segment, involving all devices that receive data. Positioning information is transmitted via carrier frequencies, which are unique to each GNSS signal.

### **1.3.1. GNSS Segments**

GNSS segment is composed of three main segments: the space segment, the control or ground segment and the user segment.

#### **1.3.1.1. The space segment**

consists of the satellites themselves, which are responsible for transmitting signals that deliver positioning, navigation, and timing information to users on Earth. These satellites are equipped with high-precision atomic clocks that enable the calculation of the time difference between transmitted and received signals, which is essential for accurate location determination.

### **The Global Positioning System (GPS)**

Originally developed under the NAVSTAR program, it is recognized as the first satellite navigation system. Initially established for military applications, GPS was later opened for civilian use, providing location measurements with an accuracy of approximately 1–2 meters for civil users (Shim & Jeon, 2018). This historical design approach underscores the dual-use nature of the system, which has been maintained and enhanced through successive modernization efforts. GPS has garnered significant attention due to its numerous advantages, including ease of use, successful implementation, and global availability (figure 1). The Veneto R., HXGN Geosystems, and other networks enhance positioning performance by integrating GPS with other satellite-based systems like GLONASS.

A significant aspect of the system's evolution involves the diversification of the pseudorandom noise (PRN) (table 1) codes that modulate the transmitted signals. The legacy L1 C/A code, which remains the primary signal for many civil users, is now complemented by the modernized signals L1C (1575.42 MHz), L2C (1227.6 MHz), and L5 (1176.45 MHz). These additional signals were introduced as part of a strategic modernization program to improve performance, robustness, and multipath resistance of the system for various applications (Shim & Jeon, 2018). In particular, the L2C signal has been transmitted from GPS Block IIR-M satellites since September 2005, and the L5 signal from GPS Block IIF satellites since May 2010, providing enhanced interference mitigation and improved resilience to scintillation effects—specifically, some studies indicate that L5 experiences fewer fading events compared to the L1 C/A and L2C signals (Biswas et al., 2019) . The incorporation of

L1C further enhances interoperability and performance by employing advanced modulation techniques as demonstrated in signal acquisition studies (Shim & Jeon, 2018).

Table 1: Description of GPS constellation as per 11th April 2025

Plane	Slot	SVN	PRN	Block-Type	Clock
B	1	56	16	IIR	RB
C	1	57	29	IIR-M	RB
D	1	61	2	IIR	RB
A	1	65	24	IIF	RB
E	1	69	3	IIF	RB
F	1	70	32	IIF	RB
A	2	52	31	IIR-M	RB
F	2	55	15	IIR-M	RB
B	2	62	25	IIF	RB
C	2	66	27	IIF	RB
E	2	73	10	IIF	RB
D	2	80	1	III	RB
B	3	44	22	IIR	RB
D	3	45	21	IIR	RB
E	3	50	5	IIR-M	RB
A	3	64	30	IIF	RB
F	3	68	9	IIF	RB
C	3	72	8	IIF	RB
A	4	48	7	IIR-M	RB
E	4	51	20	IIR	RB
C	4	53	17	IIR-M	RB
B	4	58	12	IIR-M	RB
D	4	67	6	IIF	RB
F	4	74	4	III	RB
C	5	59	19	IIR	RB
B	5	71	26	IIF	RB
E	5	76	23	III	RB
D	5	78	11	III	RB
F	6	43	13	IIR	RB
D	6	75	18	III	RB
B	6	77	14	III	RB
A	6	79	28	III	RB

Source: <https://www.navcen.uscg.gov/gps-constellation>

Block IIR: These satellites represent the second generation of GPS technology, aimed at enhancing accuracy and reliability.

Block IIR-M: These are upgraded versions of the Block IIR satellites, featuring stronger signals and additional civilian channels.

Block IIF: These satellites bring further improvements, including better precision, a new civilian signal (L5), and a longer operational lifespan.

Block III: The newest generation, equipped with highly accurate atomic clocks, superior anti-jamming capabilities, and more signals for both civilian and military use.

RB: Rubidium Atomic

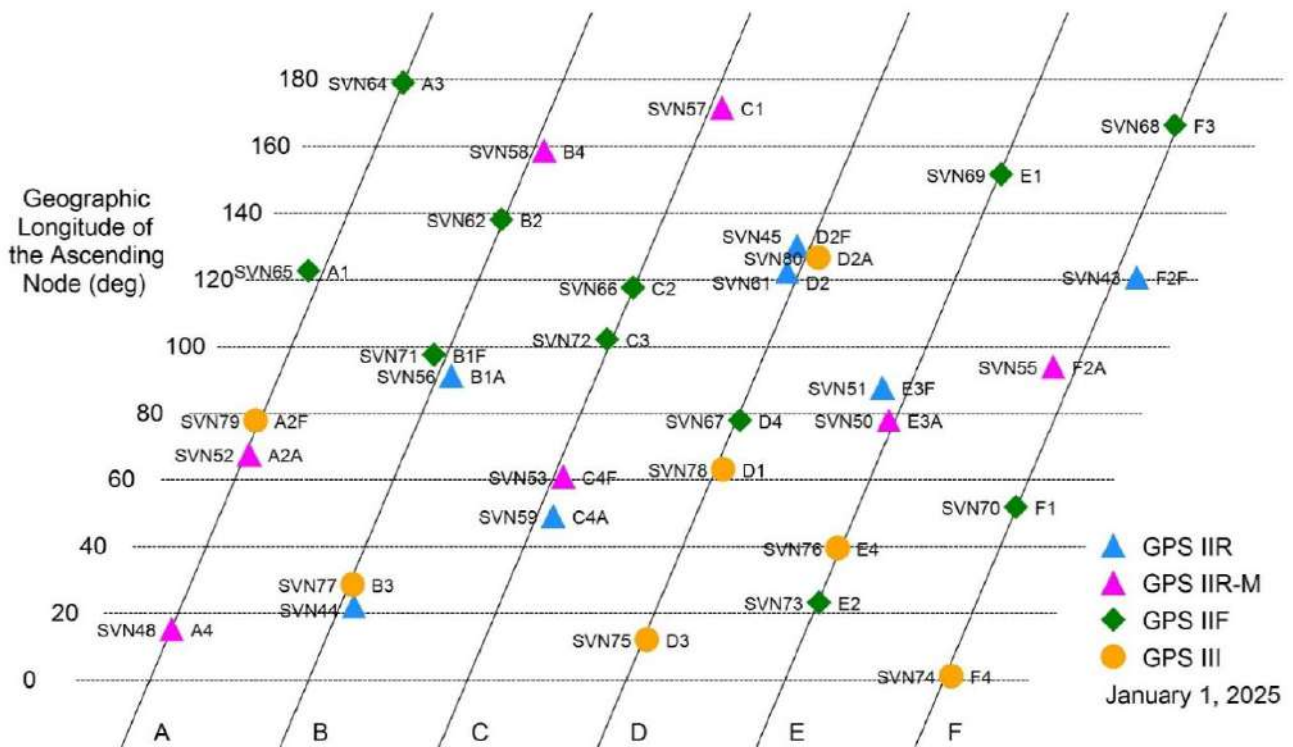


Figure 1: GPS orbital planes ; Source: <https://www.gps.gov/systems/gps/space/>

The continual modernization of the constellation has also led to an expansion in the number of operational satellites. As of April 2024, the GPS constellation comprises 32 satellites. This reflects ongoing efforts to maintain a robust navigation system that meets both military and civil requirements in the modern era (Esenbuğa & Hauschild, 2020) . This expansion not only compensates for aging satellites but also ensures that the system can support emerging applications that demand higher signal integrity and improved geometric configurations, ultimately translating to better accuracy and reliability for users worldwide (Esenbuğa & Hauschild, 2020).

### Galileo

The European Union’s satellite navigation system named Galileo (table 2) plays a crucial role in providing precise location services globally. The system operates in multiple L bands, specifically

utilizing the L1 and L5 frequencies to deliver high-accuracy signals for navigation. The L1 band, centered around 1575.42 MHz, transmits signals designated as "E1," which are used for both Open Service (OS) and Public Regulated Service (PRS) applications. The E5 band is split into two channels: E5a (1176.45 MHz) and E5b (1207.14 MHz), which support high-precision applications, including the Galileo High Accuracy Service (HAS) and other specialized services (Pintor et al., 2023).

The precision of Galileo is one of its foremost advantages, with specifications indicating that it can achieve positioning accuracy at the meter level for standard services, and up to a few centimeters under optimal conditions using multi-frequency and multi-constellation techniques (Bury et al., 2020). The incorporation of signals across different L bands allows for greater signal diversity, thereby improving the system's availability and resilience against multipath errors and signal degradation often experienced in urban environments, compared to traditional systems like GPS (Leclère & Landry, 2019). Moreover, Galileo's innovative Binary Offset Carrier (BOC) modulation technique further enhances its signal processing capabilities, enabling more accurate positioning solutions and facilitating interference rejection (W. Li et al., 2016; Qi et al., 2014).

*Table 2: Status of GALILEO Satellite constellation*

Satellite Name1	SV ID2	Clock3	Status4
GSAT0101	E11	RAFS	<a href="#">USABLE</a>
GSAT0102	E12	RAFS	<a href="#">USABLE</a>
GSAT0103	E19	RAFS	<a href="#">USABLE</a>
GSAT0104	E20	RAFS	NOT AVAILABLE
GSAT0201	E18	PHM	NOT USABLE
GSAT0202	E14	PHM	NOT USABLE
GSAT0203	E26	PHM	<a href="#">USABLE</a>

Satellite Name1	SV ID2	Clock3	Status4
GSAT0204	E22	RAFS	NOT USABLE
GSAT0205	E24	PHM	<a href="#">USABLE</a>
GSAT0206	E30	PHM	<a href="#">USABLE</a>
GSAT0207	E07	PHM	<a href="#">USABLE</a>
GSAT0208	E08	PHM	<a href="#">USABLE</a>
GSAT0209	E09	PHM	<a href="#">USABLE</a>
GSAT0210	E01	RAFS	NOT USABLE
GSAT0211	E02	PHM	<a href="#">USABLE</a>
GSAT0212	E03	PHM	<a href="#">USABLE</a>
GSAT0213	E04	PHM	<a href="#">USABLE</a>
GSAT0214	E05	PHM	<a href="#">USABLE</a>
GSAT0215	E21	PHM	<a href="#">USABLE</a>
GSAT0216	E25	PHM	<a href="#">USABLE</a>
GSAT0217	E27	PHM	<a href="#">USABLE</a>
GSAT0218	E31	PHM	<a href="#">USABLE</a>
GSAT0219	E36	PHM	<a href="#">USABLE</a>
GSAT0220	E13	PHM	<a href="#">USABLE</a>
GSAT0221	E15	PHM	<a href="#">USABLE</a>
GSAT0222	E33	PHM	<a href="#">USABLE</a>
GSAT0223	E34	PHM	<a href="#">USABLE</a>

Satellite Name1	SV ID2	Clock3	Status4
GSAT0224	E10	PHM	<a href="#">USABLE</a>
GSAT0225	E29	PHM	<a href="#">USABLE</a>
GSAT0226	E23	PHM	<a href="#">USABLE</a>
GSAT0227	E06	PHM	<a href="#">USABLE</a>
GSAT0232	E16	PHM	<a href="#">USABLE</a>

Source: <https://www.gsc-europa.eu/system-service-status/constellation-information>

### **The Global Navigation Satellite System (GLONASS)**

Developed by Russia, it serves as a crucial component of the worldwide positioning systems utilized for various applications. The GLONASS constellation currently comprises primarily GLONASS-M and GLONASS-K satellites, which enhance its functionality and service reliability.

GLONASS utilizes the L band for broadcasting its navigation signals, particularly within designated frequencies that facilitate precise operation and signal discrimination among satellites in its constellation. The operational frequencies for GLONASS are defined specifically for use within the L1 and L2 bands, with the L1 band centered around 1.602 GHz and the L2 band at approximately 1.246 GHz. These frequencies are critical for maintaining the integrity and precision of the signals transmitted for positioning applications (Panetier et al., 2023; Teunissen, 2019, Xi et al., 2020).

The GLONASS system implements a unique approach known as Frequency Division Multiple Access (FDMA), which assigns each satellite within the constellation a specific frequency channel. This separation is fundamental in allowing for the identification of signals from different satellites, essential for accurate positioning and navigation (Paziewski, 2020; Teunissen, 2019). Each GLONASS satellite broadcasts on its designated carrier frequency, which is spaced apart by 0.5 MHz, effectively mitigating the potential for interference and enhancing tracking capability (Panetier et al., 2023). For instance, the notation G1 and G2 refers to the GLONASS L1 and L2 bands, respectively (Xi et al., 2020).

Moreover, the introduction of modernized satellites, such as the GLONASS-K series, has expanded the system's functionality by incorporating Code Division Multiple Access (CDMA) on additional

frequencies, like L3 (around 1.202 GHz). This strategic shift not only improves interoperability with other global navigation systems (like GPS and Galileo) but also enhances the overall reliability of the signals due to reduced inter-frequency biases that are prevalent in the traditional FDMA model (Paziewski, 2020; Maciuk, 2018). As such, newer GLONASS satellites can broadcast signals that improve positioning accuracy significantly, especially in environments where signal proximity might otherwise limit performance capabilities (Zaminpardaz et al., 2021).

The pseudo-random noise (PRN) codes used by GLONASS for signal identification further supports its signal integrity. Each GLONASS satellite is assigned a unique PRN code that enables receivers to differentiate signals and minimize co-channel interference while receiving broadcasts from multiple satellites. The characteristic of these codes facilitates effective signal processing essential for accurate positioning solutions (H. Zhang et al., 2023a). Current operational PRNs include R04, R05, R09, R12, R21, and R26 which facilitate not only standard positioning functions but also the recent integration of CDMA signals with the existing FDMA signals and others utilizing dual-frequency signals, allowing for enhanced performance during signal reception (Zaminpardaz et al, 2021), and addressing challenges posed by inter-frequency biases during ambiguity resolution, which is critical for high-precision applications (Maciuk, 2018).

### **The BeiDou**

BeiDou Navigation Satellite System (BDS), developed by China, is a significant global navigation system that operates primarily in the L band (1-2GHz), providing critical services for positioning, navigation, and timing. The system broadcasts signal across multiple frequency bands defined as L1, L2, B1, B2, and B3, with specific emphasis on the L-band channels which are essential for various applications.

L Bands: The BeiDou system utilizes several frequency bands, particularly focusing on the L band, which encompasses L1 at approximately 1561.098 MHz and B1 at about 1575.42 MHz. Additionally, the B2 signal operates around 1207.14 MHz, while B3 operates at approximately 1268.52 (Tao Zeng et al., 2015). The BDS is designed to provide comprehensive coverage not just across the Asia-Pacific region but also globally, reflecting its strategic importance for various applications, including precise point positioning and time synchronization.

Precision: The precision of BeiDou services is critical, with capabilities to deliver positioning accuracy within a few meters for standard service users. Advanced signal processing techniques allow BeiDou

to utilize measurements from multiple satellites to correct for errors, particularly in challenging environments (Cao et al., 2023; H. Zhang et al., 2023a) reports indicate that the BeiDou system can achieve sufficient accuracy, making it reliable for a diverse array of applications, including transportation and disaster management services (Cao et al., 2023).

**Pseudo-Random Noise (PRN) Codes:** Each satellite in the BeiDou constellation is identified by a unique Pseudo-Random Noise (PRN) code, which prevents signal interference and facilitates accurate tracking in multiple applications. As of 2023, the BeiDou constellation comprises approximately 35 satellites, equipped with unique PRN identifiers such as B1I, B1C, and B2, which enhance the signal robustness and allow for multifaceted applications (Thoelert et al., 2019; A. Wang et al., 2019). These codes help distinguish satellite signals in densely populated urban areas, improving the overall reliability of the system.

**Applications:** The BeiDou system has extensive applications beyond simple location services. It offers critical functionalities for mobile communications, agriculture, maritime navigation, geological exploration, and disaster recovery. Additionally, it serves as a pivotal resource for the military, providing secure and reliable navigation capabilities (Cao et al., 2023; Chen et al., 2017). The ability to integrate BeiDou with other GNSS systems, such as GPS and Galileo, enhances the precision and availability of services, broadening its utility across various sectors (W. Chen et al., 2023; Ji et al., 2021).

### **The control or ground segment**

The control or ground segment of a Global Navigation Satellite System (GNSS) is critical for ensuring the continuous, reliable, and high-precision operation of the entire system. This segment is composed of several interrelated functions, each contributing to system integrity and user performance.

Satellite management within this segment encompasses the continual monitoring and management of satellites' statuses, configurations, and performance parameters. A unified strategy between the space and ground segments can provide a more efficient management approach where ground stations with advanced directional antennas interact with satellites to perform real-time status checks and configuration updates (Yan et al., 2022). This integrated management allows the system to promptly detect anomalies and adjust operational parameters, thereby ensuring that each satellite functions optimally.

A core responsibility of the control segment is the precise monitoring of ephemeris data and the performance of onboard atomic clocks. By continuously tracking satellite orbits (ephemeris) and clock behavior, ground stations can detect and mitigate errors that may affect positioning accuracy. Efficient fault detection and exclusion methods have been proposed to address ephemeris-related anomalies, ensuring that only robust data is used in predicting satellite positions (Jiang & Li, 2022). These processes are vital because even minor deviations can propagate significant errors in the navigation solution used by end users.

The maintenance of GNSS timescales is another crucial function performed by the control segment. By leveraging advanced techniques such as two-way satellite time and frequency transfer or multi-satellite precise orbit determination, the ground segment ensures that the GNSS system time remains tightly synchronized and highly precise (Sun et al., 2020). This rigorous timekeeping is fundamental for accurate determination of user positions, as even small timing errors can lead to substantial positional inaccuracies.

Another vital function within the control segment is the timely and accurate update of navigation files, which encapsulate precise orbital and clock information along with system configuration data. Navigation file updates, such as those evaluated in performance studies of broadcast ephemeris, are essential to provide receivers with the latest corrections and parameters needed for high-precision positioning applications (A. Wang et al., 2019). This continuous update process directly supports the overall integrity and reliability of the GNSS service provided to users.

Finally, data correction plays an indispensable role in the ground segment. Base stations collect various observational data which is subsequently used to generate corrective information. This data correction, augmented through methods that predict geocentric corrections even during communication outages, ensures that any discrepancies between the broadcast information and actual satellite conditions are minimized (Janicka et al., 2020). As such, the system's overall accuracy, particularly for critical applications involving safety-of-life considerations, is maintained through these correction processes.

Together, these aspects of the control and ground segment—satellite management, ephemeris and clock monitoring, GNSS timescales maintenance, navigation file updates, and data correction—form an integrated framework ensuring high reliability and accuracy of GNSS operations. This framework not only supports the real-time operational requirements of modern navigation applications but also paves the way for future enhancements in GNSS performance and resilience.

## **The user segments**

The user segment in a satellite navigation system encompasses all the devices and applications that receive, process, and utilize the signals transmitted by satellites to produce practical positioning, navigation, and timing (PNT) information. This segment is the critical interface between the raw data provided by the space and control segments and the end users who depend on accurate and real-time information for a wide variety of applications (Marhoon et al., 2023; Zuo et al., 2018).

GNSS receivers form the backbone of the user segment, acting as the primary hardware that captures satellite signals. These receivers are integrated into a multitude of devices, ranging from smartphones and in-vehicle navigation systems to aircraft avionics and specialized tracking equipment Marhoon et al. (2023). The design of these receivers—inclusive of their front-end circuitry, signal demodulation capabilities, and antenna configurations—critically determines the quality and reliability of the data captured (Hoi et al., 2016). High-performance receivers are designed to operate efficiently in diverse environmental conditions, ensuring that they maintain optimal signal acquisition and tracking capabilities even under challenging circumstances.

In addition to hardware, the user segment includes a broad spectrum of applications that further process and interpret the data received by the GNSS devices. These applications span diverse domains such as vehicle navigation, mapping services, geolocation-based services, and timing synchronization for communication networks and other critical infrastructures (Marhoon et al., 2023; Zuo et al., 2018). The data processing performed by these devices incorporates complex algorithms to correct errors caused by atmospheric disturbances, multipath propagation, and clock discrepancies. Such processing typically involves executing trilateration methods and implementing various filtering techniques to achieve precise determinations of position, velocity, and time.

### **1.3.2. GNSS Signals**

GNSS signals are the radio frequency (RF) signals transmitted by satellites within Global Navigation Satellite Systems (GNSS) that enable receivers on the ground to determine precise positioning, navigation, and timing (PNT) information. These signals are composed of several core components that work together to provide highly accurate PNT data. The main elements of GNSS signals include carrier frequency, ranging code, and navigation data.

### 1.3.2.1. The carrier frequency

The carrier frequency refers to the specific radio frequency at which GNSS signals are transmitted, typically within the L-band range (1–2 GHz), which offers an optimal balance between atmospheric penetration and available bandwidth (Kovář, 2020). This allocation is essential for enabling long-distance transmission with minimal attenuation, ensuring reliable global coverage across diverse environmental conditions. In addition to frequency, GNSS systems utilize carrier phase measurements, which assess the phase of the signal emitted by the satellite relative to the receiver’s signal at the time of reception. This technique allows for centimeter-level accuracy in determining the distance between the satellite and the receiver (Pesce et al., 2022). However, it is subject to errors such as phase ambiguity—difficulty in estimating the exact number of full carrier waves—and cycle slips (figure 2), which occur when continuity in tracking the carrier signal is lost (Guochang Xu, 2007). (Pesce et al., 2022) models the carrier phase as:

$$\Phi = \Phi_R(t_R) - \Phi_T(t_R) + N_R^T \quad (\text{without accounting errors})$$

$$\lambda\Phi = \rho(t_R, t_T) - C(\delta t_R - \delta t_T) + \lambda N_R^T - \delta_{iono} + \delta_{tropo} + \delta_{tide} + \delta_{path} + \delta_{rel} + \varepsilon \quad (\text{with accounting errors}).$$

$t_R$  is the time of the receiver clock,  $t_T$  is the time of the transmitter clock,  $\Phi_R$  is the phase of the receiver,  $\Phi_T$  is the phase of the received signal from the satellite,  $N_R^T$  represents the ambiguity between satellite and receiver,  $\lambda$  is the wave length and  $C$  is the speed of light.  $\rho(t_R, t_T)$  denotes the pseudorange,  $\delta t_T$  is the transmitted clock error,  $\delta_{iono}$  and  $\delta_{tropo}$  represent the error caused by ionosphere and troposphere effect on the transmitted signal respectively,  $\delta_{tide}$  accounts for tidal effects,  $\delta_{path}$  is the multipath error,  $\delta_{rel}$  is the relativistic effect,  $\varepsilon$  encompass all the non-modelled errors.

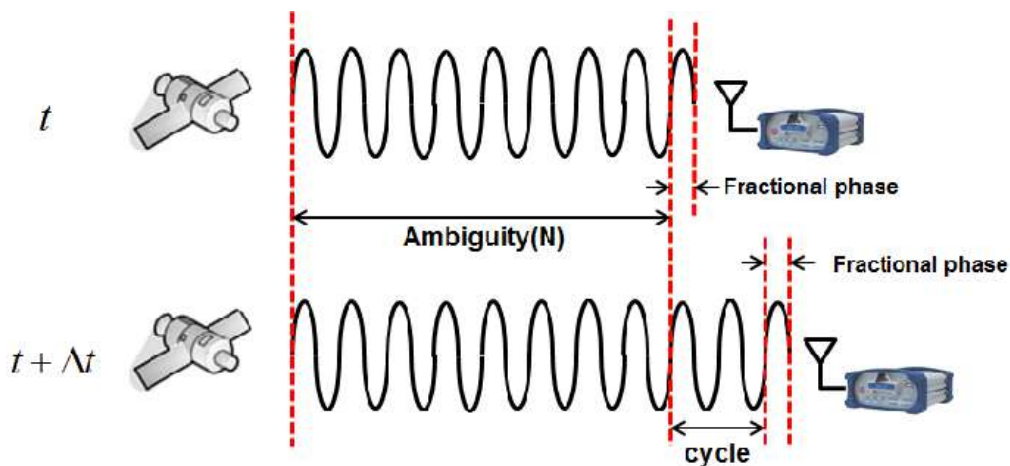


Figure 2: Carrier phase errors; source: (Park et al., 2012)

### 1.3.2.2. The ranging code

A central component of GNSS signals is the ranging code, composed of sequences of 0 second and 1 second known as Pseudo-Random Noise (PRN) codes (Jeong & Kong, 2015). These codes allow the receiver to determine the time delay between the signal's transmission by the satellite and its reception on the ground. By correlating the locally generated PRN sequence with the incoming signal, the receiver can accurately calculate the signal's travel time, which is fundamental for computing the user's distance from the satellite. This process underpins the trilateration algorithm used to determine the user's position. The resulting measurement, known as the pseudo-range (figure 3) represents the distance the signal travels and can be modelled using equations from Pesce et al. (2023):

$$\tilde{\rho} = c(t_R - t_T) = \rho(t_R, t_T)$$

$$\tilde{\rho} = \rho(t_R, t_t) - c(\delta t_R - \delta t_T) + \delta_{iono} + \delta_{tropo} + \delta_{tide} + \delta_{path} + \delta_{rel} + \varepsilon$$

$t_R$  the time,  $c$  the speed of light,  $\delta t$  is the clock errors,  $\delta_{iono}$  and  $\delta_{tropo}$  represent the errors due to the impact of ionosphere and troposphere respectively on the signal,  $\delta_{tide}$  is the error related to the earth tides,  $\delta_{path}$  is the multipath effect and  $\delta_{rel}$  is the relativistic effects.

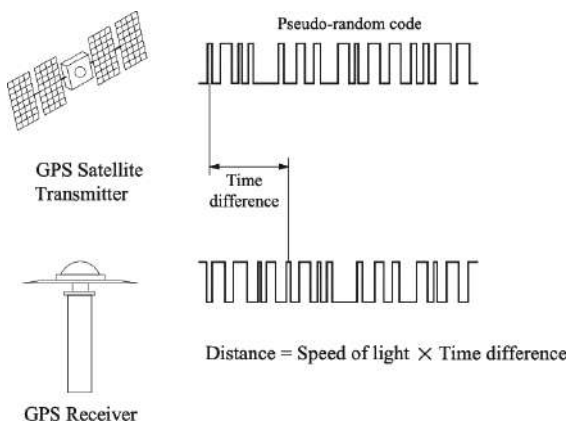


Figure 3: Pseudo-range; source: (Im et al., 2013)

### 1.3.2.3. The navigation data

The navigation data component is a binary-coded message embedded within the signal. It contains vital information such as the satellite's ephemeris (precise orbital position), clock bias parameters, almanac data (a less precise summary of satellite orbits), and the satellite's health status (Revert Calabuig et al., 2023). This information not only allows the receiver to determine the satellite's exact position and operational state at any given moment but also provides necessary corrections to

improve the accuracy of the calculated user position, velocity, and time. Together, these elements enable GNSS receivers to process the transmitted signals through complex algorithms that correct for various error sources, such as atmospheric delays and multipath effects, thereby yielding accurate PNT information. Advanced processing techniques ensure that even when signals are degraded by environmental factors or interference, the integrity of the computed position and time remains uncompromised (Jeong & Kong, 2015; Revert Calabuig et al., 2023).

#### **1.3.2.4. Errors in signal interpretation**

Errors associated with GNSS signals can significantly affect position accuracy. Therefore, a thorough understanding of these errors is crucial for their modelling and their mitigation (H. Li & Li, 2025).

##### **Satellite clock errors**

Clock errors are mainly due to the lack of synchronization between the satellite and receiver clocks. Clock errors are generally modelled using polynomial functions and apply equally to users worldwide extracting data from the same satellite. Clock errors may be exacerbated by environmental factors combined with design imperfections of the satellite's onboard clock (Mansur & Ferreira, 2019). Measuring the position of a point at different epochs can be an option to correct clock errors (H. Li & Li, 2025). This is achieved by subtracting observations of one epoch from those of the subsequent one to cancel clock biases (Zhou et al., 2020). Another alternative is to use the mix-differenced approach, which merges epoch-differenced and undifferenced observations. In practice, this is achieved by combining time-differenced carrier phase and undifferenced pseudorange measurements to improve accuracy (Xi et al., 2020). The mix-differenced approach fits very well with the NRTK method (Y. Chen et al., 2018). By using highly accurate satellite data supplied by the International GNSS Service (IGS) and only carrier phase rather than pseudorange, the Real-time Precise Point Positioning (PPP) method can efficiently reduce time errors (El-Mowafy, 2018) and can be considered as an additional asset to reduce clock errors.

##### **Satellite orbit errors**

The GNSS plays a major role in the accuracy of satellite positioning through continuous monitoring of the location of satellites, calculation of orbit eccentricities, and production of ephemerides. The latter reports any deviations in satellite orbits (figure 4) and enable GNSS receivers to correct some orbital errors. One important factor contributing to orbital errors is gravitational perturbations, which may modify the satellite trajectory. This issue can be addressed only by using highly advanced

models that simulate current orbit perturbations from General Relativity effects such as the Schwarzschild, Lense-Thirring, and de Sitter effects (Sośnica et al., 2021). It is also important to note that the shape of the orbit can enhance errors. In fact, when the orbit of the satellite is slightly elliptical, the satellite is highly influenced by other celestial bodies such as the Moon, which greatly modifies its trajectory and increases uncertainty in predicting its path (Rosengren et al., 2015). Some environmental factors, such as solar photons, also contribute to increased orbital errors. These photons induce the so-called solar radiation pressure (SRP) that brings changes in the semi-major axis, eccentricity, inclination, argument of perigee, and right ascension of the ascending node (Alessi et al., 2018; Pratiwi et al., 2025). For this reason, frequent maintenance of satellites should be performed to maintain the satellite in its original orbit (Pratiwi et al., 2024). Considering that orbit accuracy depends on the GNSS network, as the latter provides more accurate corrected ephemerides for points located in their close vicinity, connecting the GNSS receiver to the same network can be a way to mitigate orbit errors (Sośnica et al., 2021).

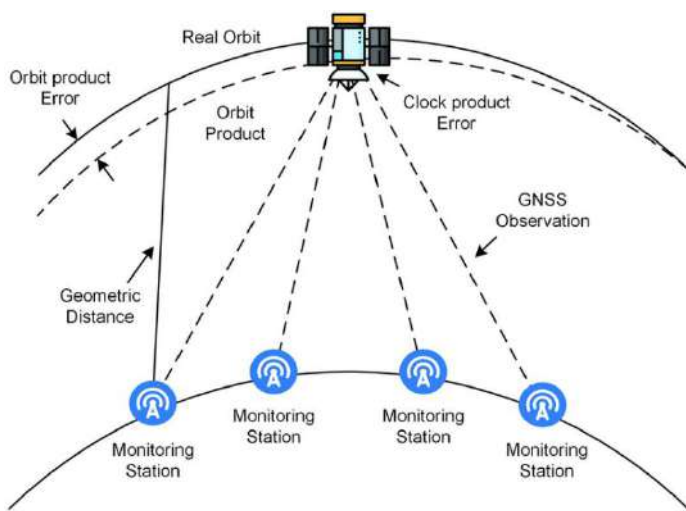


Figure 4: satellite orbit error; source: (Huang et al., 2025)

### Ionospheric delays

When GNSS signals cross the ionosphere (50-1000 km), they encounter delays (figure 5) that are mostly the result of spatial variations in electron density. The ionospheric delay primarily depends on solar activity, time, and location. The dynamics of ionospheric delay are closely linked with atmospheric composition and the rate of extreme ultraviolet radiation (EUV) (Vaishnav et al., 2021). In general, the ionospheric response, which is the time UV takes to interact with the surrounding atmosphere, can be delayed by 5.5 minutes (Chakraborty et al., 2021; Schmölter et al., 2018; Wulansari et al., 2023). To reduce ionospheric delays, ionosphere-float and ionosphere-weighted

models are commonly used for RTK applications (Farah, 2020; X. Li et al., 2023). Some advanced models, such as NeQuick, provide very high accuracy and are suitable for high latitude areas (Farah, 2018).

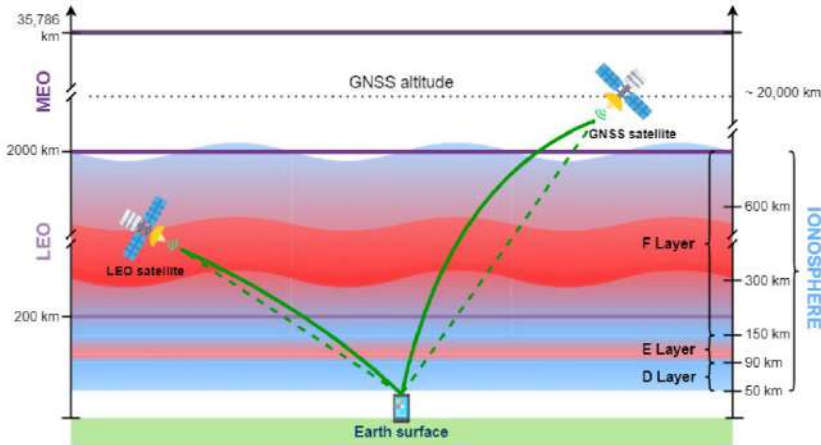


Figure 5: Ionospheric delay error; source: (Imad et al., 2023)

### Multipath errors

Errors in global navigation satellite systems (GNSS) due to multipath occur when signals from satellites interact with objects like buildings or trees before reaching the receiver (figure 6). This interaction alters the signal travel time, leading to location errors that can exceed 50 meters in urban areas. The most significant issues arise in densely populated city environments where line-of-sight conditions are obstructed, exacerbating these errors as signals may bypass direct paths entirely and reflect off multiple surfaces (Gu et al., 2016). These situations highlight the need for improved methods and tools, such as enhanced GNSS receivers and strategically placed antennas, to mitigate these errors (Kaloop et al., 2019; Y. Li et al., 2017). Machine learning and advanced algorithms can also help address multipath issues (Hsu et al., 2016; Quan et al., 2018). Incorporating environmental factors like 3D urban landscapes into algorithms has shown promising results (Gu et al., 2016; Zuo et al., 2018). Additionally, integrating inertial navigation systems with motion sensors and LiDAR technology, which enables 3D scanning of the environment, has proven effective in reducing multipath errors despite the high investment costs associated with these technologies (Lubeigt et al., 2021; Pirsiavash et al., 2018; Suzuki, 2019).

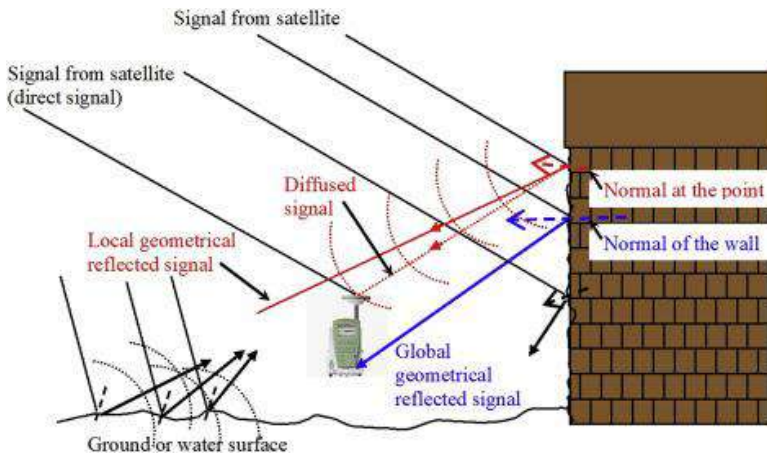


Figure 6: Illustration of multipath error; source: (Lau, 2021)

#### 1.4. GNSS augmentation systems

GNSS augmentation systems are external infrastructures designed to enhance the performance of standard GNSS signals by improving accuracy, integrity, availability, and reliability. These systems include Satellite-Based Augmentation Systems (SBAS), such as WAAS, EGNOS, and MSAS, which provide wide-area corrections and integrity monitoring via geostationary satellites (Walter, 2017). Ground-Based Augmentation Systems (GBAS) are deployed at airports to support precision approach and landing operations by broadcasting differential corrections and integrity data from surveyed reference stations (Hugentobler & Montenbruck, 2017).

Real-Time Kinematic (RTK) offers centimeter-level accuracy by transmitting real-time corrections from reference stations to receivers, and recent research has explored integrating SBAS data to improve RTK reliability in high-performance applications such as autonomous driving and UAV navigation (Y. Wang & Shen, 2024).

Differential GPS (DGPS), a precursor to RTK and GBAS, uses fixed base stations to broadcast correction data that mitigate common GNSS errors over short to medium distances. These augmentation systems, while not part of the core GNSS architecture, are essential for supporting the user segment in applications requiring enhanced precision and integrity.

Some techniques such as relative positioning (figure 7) can be blinded with GNSS augmentation signals to improve position accuracy. In this case, we have two receivers where one is located at a well-known point while the other is in an unknown point. The two points received data from the same GNSS constellation. The error is reduced using this method. In fact, as the distance between the two points is short in comparison with the altitude of the satellites, the effect of atmospheric

disturbance is not perceptible (Y. Li et al., 2017). As the two receivers are relatively close to each other, the error related to satellite clock timings, ionospheric and tropospheric delay is reduced: this consequently enhances the accuracy of the measurement (S. Yu & Liu, 2021). Furthermore, this technic uses carrier measurement instead of pseudorange measurement to calculate the distance, which results in higher precision as seen above. When the two receivers are distant from a few kilometers of magnitude, the positioning can be achieved with an accuracy of the level centimeter (Yeh et al., 2009).

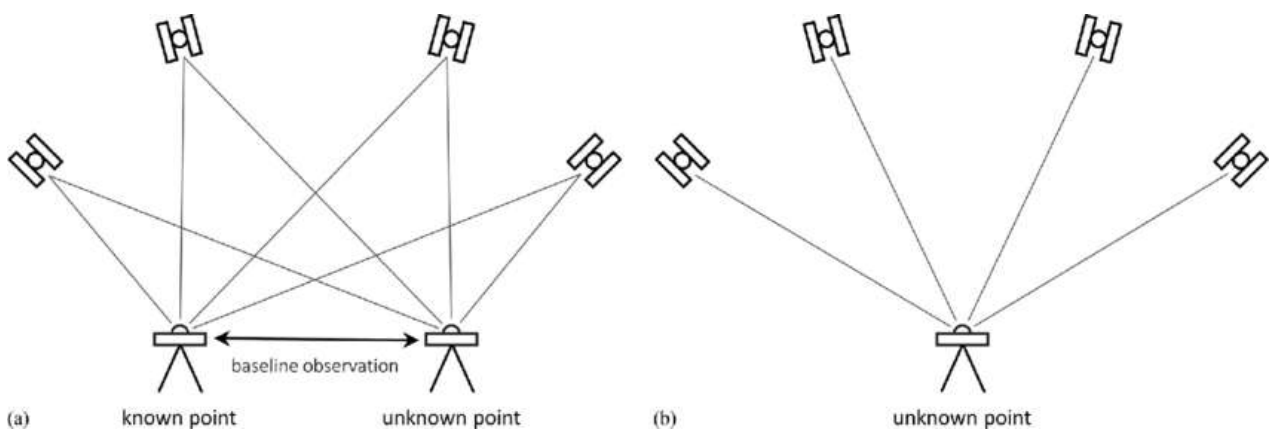


Figure 7: Illustration of Relative position Method; source: (Jamieson & Gillins, 2018)

#### 1.4.1. Differential GPS

The aim of Differential GPS (DGPS) (figure 8) is to improve the accuracy of the position provided by standard GPS. This correction is performed by a reference station, known as the Master, whose position is precisely known. The error in location is determined by comparing the position of the Master with the one obtained from the satellite. This correction is then sent to the mobile receiver, referred to as the Rover, which is in the field. The transmission can occur via the internet, radio waves, or cellular networks (Dunn et al., 2006).

The accuracy of DGPS is generally within a few meters, compared to standard GPS, which typically has an accuracy range of about 10 meters (Baselga, 2010). Thus, this procedure involves three main components: the Satellite, the Master, and the Rover.

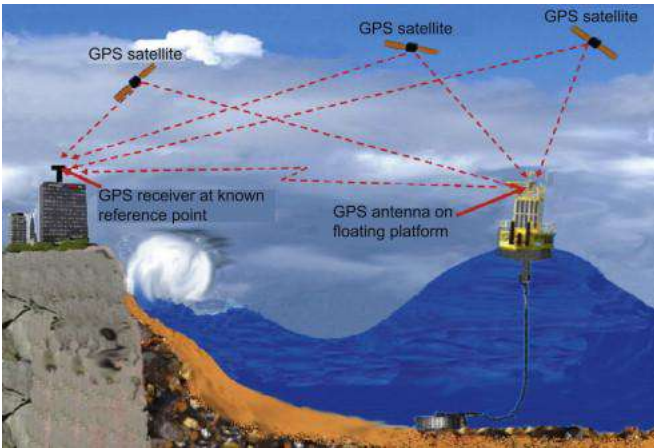


Figure 8: Illustration of differential GPS applied for sea level measurement; source: (Joseph, 2011)

#### 1.4.2. Real Time Kinetics (RTK)

Nowadays RTK, it is the most used method for positioning using GNSS (figure 9) due to its ease of use and accuracy (Căţeanu & Moroianu, 2024). This gain in accuracy is achieved through GNSS signal correction by a reference station (Feng & Wang, 2008). The main components of RTK are the receiver and the reference station. Both the receiver and the reference station receive carrier phase signals from the satellite. The reference station compares the information contained within the carrier phase with its expected position. It then corrects all related errors and transmits the data to the receiver, which adjusts its position accordingly (Valente et al., 2020).

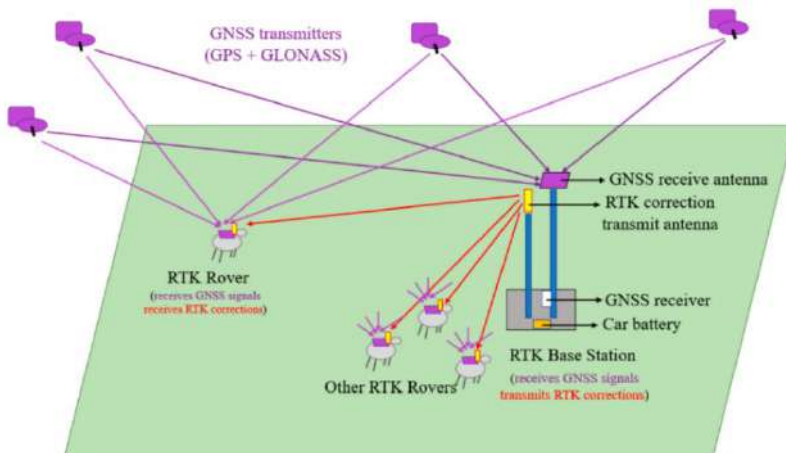


Figure 9: Illustration of the transmission of the RTK functioning; source (Keshavarzi et al., 2021)

The common errors associated with the transmission of the carrier phase are related to the satellite clock, ionosphere layer, troposphere layer, antenna construction, and location (Gümüş & Selbesoğlu, 2019).

### **1.4.3. Network Real-Time Kinematic (NRTK)**

NRTK improves the RTK by eliminating distance dependence thanks to a network of reference station such that if the observation of one reference station is not operational, another one can substitute. There are currently four methods of transmission of the data (Berber & Arslan, 2013) namely: MAX, individualized MAX (I-MAX), FKP and VRS.

Virtual Base Station (VRS): In the VRS method, the rover uses GSM technology to send its approximate coordinates in NMEA format to the data processing center. The center then establishes a virtual reference station at the approximate location. Distance-dependent errors between the main reference station and other reference stations are calculated and interpolated to the position of the virtual reference station. The rover calculates its position using a standard relative positioning method, leveraging observations and corrections from a virtual reference station to achieve centimeter-level accuracy (Gümüş & Selbesoğlu, 2019; Wanninger, 2003).

In the MAX method, the server transmits raw data received from satellites to a single reference station, known as the Master station. Simultaneously, it also sends raw data to auxiliary stations. These auxiliary stations process the data by resolving ambiguities and calculating the relative distance with respect to the Master station. All this information is then sent back to the server (Berber & Arslan, 2013). The data from the auxiliary stations, combined with the refined data from the Master station, provide the system with additional resources to achieve more accurate results. MAX is considered the most precise method in Network Real-Time Kinematic (NRTK) positioning, as it allows the rover to optimize its solution by adapting to atmospheric conditions using the most suitable reference stations (Janssen, 2009)

I-Max: In this method, the user transmits its position to the data processing center. The center identifies the nearest reference station to the user's location as the main reference station. Corrections are then computed using the main reference station and nearby auxiliary reference stations and sent via the internet. The network points are grouped, and corrections are calculated for each zone in the MAC method (Gümüş & Selbesoğlu, 2019).

Flächen Korrektur Parameter (FKP) method: In this method, the position of the rover is not important. The system creates area correction parameters for a well-defined place located around the reference station. This method assumes that the distance depends on error between the rover

and the reference station change linearly (Berber & Arslan, 2013). Meanwhile, interpolation can be used in case of non-linearity (Janssen & Haasdyk, 2011).

#### **1.4.3.1. HXGN SmartNet**

HXGN SmartNet represents a significant advancement in Global Navigation Satellite System (GNSS) technology, specifically within the framework of RTK positioning and reference networks. This network, which includes over 5,300 GNSS reference stations globally, facilitates high-precision positioning. The operational effectiveness of HXGN SmartNet hinges on the continual maintenance and updates necessary to uphold the integrity of its correction services (Matonti, Miller, et al., 2025; Matonti, Wnuk, et al., 2025). Daily solutions are computed using advanced software algorithms and the latest International Terrestrial Reference Frame (ITRF2020) standards, ensuring that users benefit from the most accurate and up-to-date positional information available (Matonti et al., 2023). This routine updating of station coordinates within the network is vital for maintaining its competitive edge in accuracy and service quality, further optimizing positional outcomes for users who rely on precise GNSS data (Matonti, Miller, et al., 2025; Matonti, Wnuk, et al., 2025).

HXGN SmartNet uses signals from Beidou, GPS, Galileo and GLONASS. The types of corrections used to refine the position are Virtual Base Station (VRS), i-MAX RTK: Nearest (Single Base).

#### **1.4.3.2. VENETO REGION GNSS RTK NETWORK**

The Veneto Region GNSS RTK Network constitutes an essential geodetic infrastructure to support topographic and cadastral survey operations across the regional territory (Fabris & Floris, 2025). The network operates with permanent stations active 24 hours a day, 7 days a week. The permanent stations of the Veneto R. (table 3) are provided by institutional entities and private subjects, and the observational data is freely accessible through this portal upon registration.

The network can ensure coverage of the entire regional territory (figure 10) with a redundancy factor of three and a coverage radius of approximately 20 km (Unipd et al., 2008). Such a density of stations is essential to guarantee an adequate redundancy factor, considering that one of the primary objectives is the continuous and systematic provision of a service like the one proposed by the Veneto Region; a density that can therefore ensure, in case of unavailability of one of the network stations, coverage by another nearby station to maintain service continuity. The network is currently managed by the University of Padova, which ensures coverage of about 60% of the regional territory with a radius of 50 km from the stations (Unipd et al., 2008). The University

performs both post-processing of the observation files (RINEX data) and real-time data distribution (RTCM).

Table 3: Location of the Veneto R.

<b>Station</b>	<b>IERS</b>	<b>Location</b>
	<b>Domes</b>	
<b>AFAL</b>	12766M001	Alpe Faloria
<b>ASIA</b>	12714M002	Asiago
<b>BL01</b>	19585M002	Belluno
<b>BOCN</b>	19063M001	Bosco Chiesa Nuova
<b>BORC</b>	19515M001	Borca di Cadore
<b>BTAC</b>	19065M001	Bonavigo
<b>CGIA</b>	19552M001	Chioggia
<b>CITT</b>	19066M001	Cittadella
<b>GRDO</b>	18803M001	Grado
<b>LEG1</b>	19068M002	Legnago
<b>LEG2</b>	19068M003	Legnago
<b>MAVE</b>	19060M001	Monte Avena
<b>MBEL</b>	14626M001	Montebelluna
<b>PADO</b>	12750S001	Padova
<b>PIEV</b>	12743M001	Pieve di Cadore
<b>PRTG</b>	19512M001	Portogruaro
<b>PSAL</b>	19513M002	Venezia Punta Salute
<b>ROVI</b>	12769M001	Rovigo
<b>SAPP</b>	19516M001	Sappada
<b>SCHI</b>	19070M001	Schio
<b>SDNA</b>	19510M001	San Donà

Station	IERS	Location
	<b>Domes</b>	
<b>TAMB</b>	19554M001	Tambre d'Alpago
<b>TEOL</b>	19071M001	Teolo
<b>TGPO</b>	19511M001	Taglio di Po
<b>TRVS</b>	19074M001	Treviso
<b>VELO</b>	19518M001	Velo d'Astico
<b>VENI</b>	18849M001	Venezia Nicelli
<b>VICE</b>	19072M001	Vicenza
<b>VR02</b>	19073M001	Verona

Source: (Regione del Veneto, 2025)

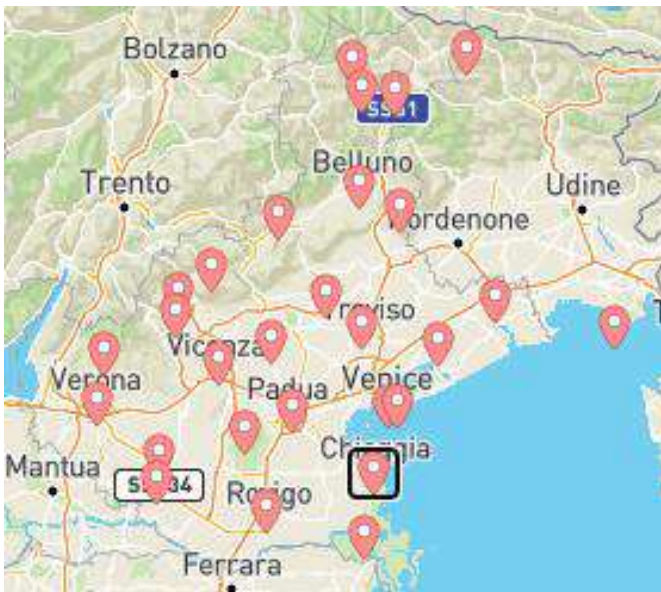


Figure 10: Partial view of the Veneto R.; source (Regione del Veneto, 2025)

### 1.5. Post processing Method

In post-processing, GNSS data are not corrected instantaneously as in the case of RTK. Rather, they are saved in the receiver (RINEX format in the case of Veneto R.) to be processed later by the user. Additional input is also obtained from the ephemerides of the satellite downloaded from NASA's website. Ephemerides associated with the RINEX file are post-processed using HXGN Infinity survey software to compute point positions. This technique is more accurate than NRTK.

## **1.6. Classification of topographic method**

### **1.6.1. Geometric Levelling (From the middle)**

Geometric levelling is a vital technique used to determine the height differences between two or more points. The principles behind geometric levelling relate intimately to the geometric characteristics of the Earth, particularly its curvature and the horizontal plane.

In executing geometric levelling, one fundamental method of establishing accurate height differences is using levelling instruments such as automatic levels, digital levels, or precise theodolites. These instruments measure the line-of-sight distance to a levelling rod held vertically at the point of interest. By achieving a horizontal line of sight, surveyors can ascertain differences in elevation with respect to a datum point (Wardhani et al., 2023).

The precision of geometric levelling is typically influenced by several factors, including instrument calibration, the observer's ability to maintain the horizontal line of sight, and environmental influences such as atmospheric refraction. High-quality instruments can achieve a level of precision down to a few millimetres over short and medium ranges, depending on the method employed (GÜNDÜZ & BULUT, 2017). Seasonal variations in temperature and pressure can also induce measurement errors; therefore, implementing correction factors is essential in high-precision applications.

### **1.6.2. Total station**

A total station (figure 11) is an advanced surveying tool that combines the capabilities of a theodolite and an electronic distance measurement (EDM) device, enabling precise measurements of angles and distances at the same time. It usually includes dual systems for measuring horizontal and vertical angles, making it a versatile instrument for various geodetic tasks (Rysbekov et al., 2019; Šiaudinytė & Grattan, 2016).

A total station typically consists of an electronic theodolite, an EDM, and a microprocessor for processing data. The theodolite measures angles, while the EDM calculates the distance to a point using electromagnetic waves. The device emits a laser or infrared beam towards a target reflector and measures the time it takes for the signal to return, calculating the distance based on the speed of light. Devices that can measure without reflectors are expanding the use of total stations, improving their accuracy and utility in challenging terrains or confined spaces, such as measuring antennas (Guan et al., 2021).

Measurement accuracy of total stations can be affected by various factors, including environmental conditions. For example, excessive sunlight can interfere with the infrared rays emitted by the total station, affecting measurement precision, especially on hot days when heat can scatter or absorb light rays (H. Zhang et al., 2023b). Other factors like atmospheric pressure and humidity can also introduce errors, requiring thorough calibration for applications ranging from construction to environmental monitoring (Lösler et al., 2023; Rysbekov et al., 2019).

In practice, total stations are widely used for monitoring structural deformations in tunnels and bridges, providing highly accurate measurements often within a millimeter range (Yue et al., 2021). For instance, when monitoring tunnel displacements, total stations can achieve accuracies of up to 1 mm, which is crucial for ensuring structural integrity during construction and maintenance (Luo et al., 2016; Yue et al., 2021). They are also used in advanced systems for dynamic measurements, such as tracking the movements of heavy machinery, enhancing geospatial data collection in difficult environments (Felski, 2022).

Recent advancements in total station technology have led to models capable of reflective measurements without prisms, allowing for more flexible surveying in complex environments (Chieu et al., 2023). These innovations enable surveyors to collect data more efficiently while maintaining high accuracy, essential for tasks like environmental monitoring, construction, and infrastructure management (Kim et al., 2017).

Total stations are often compared with other technologies like 3D laser scanning in terms of measurement accuracy and operational efficiency. Studies show that while both technologies offer high precision, the choice between them depends on the operational context, including time constraints and physical access to measurement points (F. Yu et al., 2023).

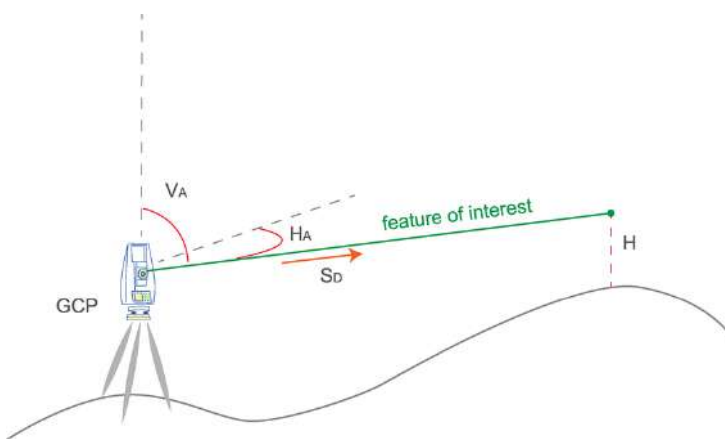


Figure 11: Total station ; source : (Sofos et al., 2017)

## 2. MATERIAL AND METHODS

### 2.1. Site presentation

The test site is located at Padova in the Veneto region (figure 12). The Veneto region is in the Nord-Est of Italy and is surrounded by Lombardy at the West, Trentino south Tyrol at the North, Friuli-Venezia Giulia at the Est and Emilia-Romagna at North.



Figure 12: Presentation of Veneto Region; source: (VENETO R.INFO, 2025)

For the survey, two observation points, namely point 1000 and point 2000, were appointed. The respective coordinates of these points were initially unknown (figure 13). These points were within visible range of each other, approximately 76 meters apart. We opted for two points instead of one because comparing coordinates from different networks at a single point could result in discrepancies due to varying reference systems. By using two points, any differences in elevation and East-North coordinates from different networks should remain consistent, regardless of the reference system.



Figure 13: Presentation of the site; source: (Google, 2025)

## 2.2. Material

To carry out this study, classical topographic method and relative and differential positioning were used. Each of these surveys required specific types of instruments.

### 2.2.1. Instruments for classical topographic survey

Measurement of inclined angles, horizontal and sloped distances, as well as elevation differences, was carried out using a total station that integrates an electronic transit theodolite with an electronic distance meter (EDM). A 360-degree survey prism was employed to reflect the EDM signal, enabling accurate determination of both horizontal and vertical angles. The EDM calculates distance based on the time it takes for the signal emitted by the total station to reach the prism and return. Angular measurements are obtained through the electronic theodolite component of the total station.

For the purposes of this study, the total station used was Leica Flex Line TS10 (figure 14). It has very high accuracy and flexibility. The use of this instrument did not require an assistant to hold to handle the reflector as the previous versions.



Figure 14: Total station used for the project

### **2.2.2. GPS survey equipment**

The GPS receiver used was made up of the following compounds:

GPS smart antenna.

GPS controller with microprocessor.

Data recording system.

#### **2.2.2.1. GPS smart antenna**

The smart antenna used for this study was the Leica Viva GS16 (figure 15), known for its high accuracy. This smart antenna receives radio signals emitted by GPS satellites. The signals are then amplified to restore any loss of signal quality that occurred during transmission. Noise reduction is also performed to ensure high accuracy. After converting the signals into electrical signals, the GPS receiver can precisely determine location, speed, and time.



Figure 15: Smart antenna Leica viva GS16 in the field; source: Author and (Leica geosystems, 2021)

#### 2.2.2.2. GPS controller

The GPS controller Leica Viva CS15 was used to collect the position of the point using the two NRTK networks at various epochs. This device can connect with other equipment for data transfer using 3.5G internet, Bluetooth, Wi-fi and USB.

### 2.3. Method for survey

#### 2.3.1. Horizontal distance measurement

Horizontal distance between the point 1000 and 2000 (figure 16) considered as the reference distance was measured using Leica Flex Line TS10 + instrument and a Leica 360° prism target to ensure local precision and accuracy. The instrument was mounted on a pole with tripod legs, positioned 1.5 meters above the ground. Initially, the total station was set up at Point 1000, while the prism target was placed at Point 2000. After completing the observations, the positions of the total station and the prism were reversed to enable measurements from Point 2000 to Point 1000. For each setup, direct and reverse measurements were performed to ensure consistency. The total station was configured to average two measurements per observation, resulting in an average of four observations per point.



Figure 16: Total station positioned at point 1000 (A); location of Point 2000 (B).

### 2.3.2. Elevation measurement

The geometric levelling from the middle technique also known as central point method was applied to measure altitude of the points. In the case of this study, it is considered as the reference measurement for elevation thanks to its high accuracy. This method involves positioning the levelling instrument equidistant between two survey points, in this case, Point 1000 and Point 2000. By maintaining equal backsight and foresight distances, the setup minimizes systematic errors caused by atmospheric refraction and collimation.

Balancing the sight distances ensures that any residual errors from the instrument or the levelling staff are evenly distributed, thereby increasing the reliability of the height difference measurements. This technique is particularly effective in reducing cumulative errors over short to medium distances and is widely used in high-precision levelling operations.

### 2.3.3. NRTK GNSS Survey for HXGN

The NRTK survey was conducted using two GPS receiver setups as rovers. Each setup included a Leica Viva GS16 smart antenna (figure 17) and a HXGN Viva CS15 controller, both mounted on a 1.1-meter fixed-height pole with tripod legs. One rover was positioned at point 1000 and the other at point 2000. Each receiver was connected to two GPS networks (HXGN and Veneto R.) via the internet. Real-time differential corrections from each network were received at different epochs, achieving centimeter-level of precision.



Figure 17: RTK GNSS antenna operating on the site

#### **2.3.4. Veneto Region GNSS RTK network**

To acquire high-precision GNSS data, the Leica Viva GS16 smart antenna was deployed at Point 1000 and Point 2000, consistently mounted on fixed-height poles. The receiver was connected to the Veneto R. network via an internet-enabled HXGN Viva CS15 controller. Managed by the University of Padova, this network provided real-time differential corrections using RTCM protocols, transmitted from nearby permanent reference stations. This configuration ensured centimeter-level accuracy during data acquisition. Observations were recorded at multiple epochs to assess consistency and precision across the two points.

For post-processing, the University of Padova recorded observational data from its reference stations in RINEX format and made them available for download. These files were processed using Leica Infinity software, which integrates raw GNSS observations with satellite ephemerides—typically sourced from NASA—to refine positional accuracy. This dual approach, combining real-time corrections with post-processed data, ensured robust and reliable GNSS positioning throughout the survey.

#### **2.3.5. Description of the data**

Collection of data (table 4) from terrain were done on six different days: the 19<sup>th</sup> of March 2025, 24<sup>th</sup> of March 2025, 2<sup>nd</sup> of April 2025, 9<sup>th</sup> of April 2025, 28<sup>th</sup> of April 2025 and 30<sup>th</sup> of April 2025. The data were collected through Veneto R. and HXGN at different epochs expressed in seconds. The epoch is the exact time at which satellite measurements were taken by the receiver. Overall, we

have 23 epochs: E1= {1s, 2s, 3s, 4s, 5s, 6s,7s, 8s, 9s} and E2= {10s, 20s, 30s, 40s, 50s, 60s, 120s, 180s, 240s, 300s, 360s, 420s, 540s, 600s}.

Below is the description of the data collected:

**GDOP:** Geometric Dilution of Precision (GDOP) reflects how the relative positions of satellites in the sky affect the accuracy of a GNSS receiver's calculated position and time. It essentially indicates how "good" or "poor" satellite configuration is for accurate positioning. A GDOP value of less than 1 is characteristic of ideal satellite geometry, resulting in highly precise location estimates.

**CQ1D:** It stands for coordinate quality in 1 Dimension. It represents the standard deviation of the vertical (height) component of GNSS measurements at a given point, serving as a statistical indicator of the precision and reliability of altitude data. In a simple way, CQ1D tells how much the height measurements from the GNSS device oscillate up and down when you measure the same spot multiple times. If the wiggle is small, your data is precise and reliable.

**CQ2D:** It stands for Coordinate Quality in 2 Dimensions, and it refers to the horizontal precision of GNSS measurements. It is calculated as the standard deviation of the horizontal (latitude and longitude) position measurements at a given point. In a simple way, CQ2D tells how much the GPS "dot" moves left and right (east-west) or forward and backward (north-south) when you measure the same spot many times.

**CQ3D:** It stands for Coordinate Quality in Three Dimensions. It is a statistical measure that reflects the overall precision of GNSS positioning in all three spatial dimensions: Latitude (X), Longitude (Y), Altitude (Z).

**CQ3D** is typically calculated as the root mean square (RMS) or standard deviation of the combined horizontal and vertical components of GNSS measurements taken at a single point. It gives a single value that summarizes the total spatial accuracy of the position.

F12: Represents the East and North coordinates of a point in UTM\_12.

F32: Represents the East and North coordinates of a point in UTM\_32.

The reference distance was found using total station while the reference elevation was found using digital levelling.

Table 4: Summary of the data collected during this experiment

Date	Point	NRTK
19th March	1000	HXGN
24th March	2000	HXGN
2nd April	1000 & 2000	HXGN
9th April	1000	Veneto R.
28th April	1000 & 2000	HXGN
30th April	2000	Veneto R.

Source: Author

### 2.3.6. Measurement calculations

The distance between Point 1000 and Point 2000 expressed in meters was computed as per the referential using the formulae:

$$D = \sqrt{(X_{1000} - X_{2000})^2 + (Y_{1000} - Y_{2000})^2}$$

The error in distance, referred to as the “distance difference”, was calculated by subtracting the reference distance from the measured distance D.

The error in elevation, referred to as the “elevation difference”, was obtained by subtracting the reference elevation from the elevation measured using NRTK positioning.

### 2.3.7. Performance evaluation and ranking

To assess the performance of GNSS NRTK networks, statistical methods including Interquartile Range (IQR) and Percentile analysis were applied, following the approach of NGUYEN et al. (2025). These methods enable the detection of outliers and the evaluation of measurement consistency and accuracy specifically:

Median: Indicates the central accuracy of positioning; values closer to zero reflect higher precision.

IQR (Spread): Captures the consistency of measurements; smaller values suggest more reliable results.

Whiskers (upper and lower): Represent the range of typical values; narrower ranges imply better control over errors.

Outliers: Reveal instability or anomalies in the network; fewer outliers indicate greater robustness.

All these elements were grasped through boxplot analysis on GDOP, CQ3D, CQ2D, CQ1D, difference in Distance and difference in elevation with respect to the reference value (the one obtained using classical topography).

For each of the parameters studied, the overall score was computed according to the equation:

$$score = 0.4 * |Median| + 0.3 * |IQR| + 0.2 * |upper whiskers| + 0.1(number\ of\ outliers)$$

### 2.3.8. Optimal utilization of the NRTK network

To determine the optimal time at which the elevation and distance differences between the two NRTK networks are minimized as effectively as possible, we applied the Scalarization (or Aggregation) Method (Giagkiozis & Fleming, 2015). This method transforms a multi-objective optimization problem into a single-objective problem by combining all objectives using a function such as:

Weighted Sum norm (L1) for which the main goal is to balance overall error

$$\min (|f_1| + |f_2| + \dots + |f_n|)$$

Weighted Euclidean Norm (L2) that penalizes at best larger deviations as per the following equation

$$\min \sqrt{f_1^2 + f_2^2 + \dots + f_n^2}$$

Weighted Chebyshev Norm (L $\infty$ ) that minimizes the worst metric as per the below equation

$$\min (\max(|f_1|, |f_2|, \dots, |f_n|))$$

In this method, f represents an objective function.

### 3. RESULTS AND DISCUSSION

#### 3.1. Comment on the trend of each graphics

##### 3.1.1. Veneto R.

##### CQ trend at point 1000

The 3D Quality Control (QC3D) metric exhibits an initial value of 0.0173 meter and reaches a peak of 0.0426 meter at 2 seconds (figure 18). As the observation duration increases—particularly beyond 40 seconds—the QC3D progressively decreases and stabilizes, ultimately falling below 0.01 meter and approaching 0.005 meter by the end of the 600 seconds observation period (figure 19). This trend demonstrates a marked enhancement in theoretical positional accuracy with extended observation time. Notably, the CQ2D and CQ1D curves consistently remain lower than the CQ3D, which is expected given that they represent individual components of the overall spatial accuracy (horizontal and vertical components, respectively).

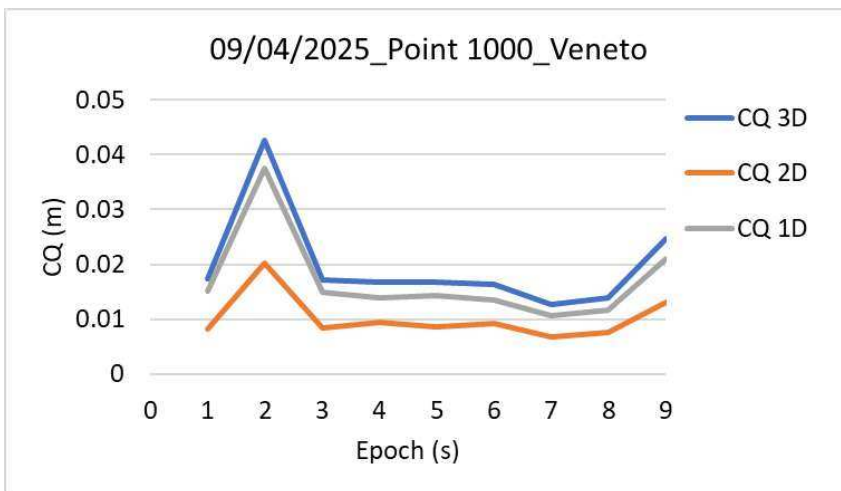


Figure 18: CQ values from epoch 1s to epoch 9s at point 1000

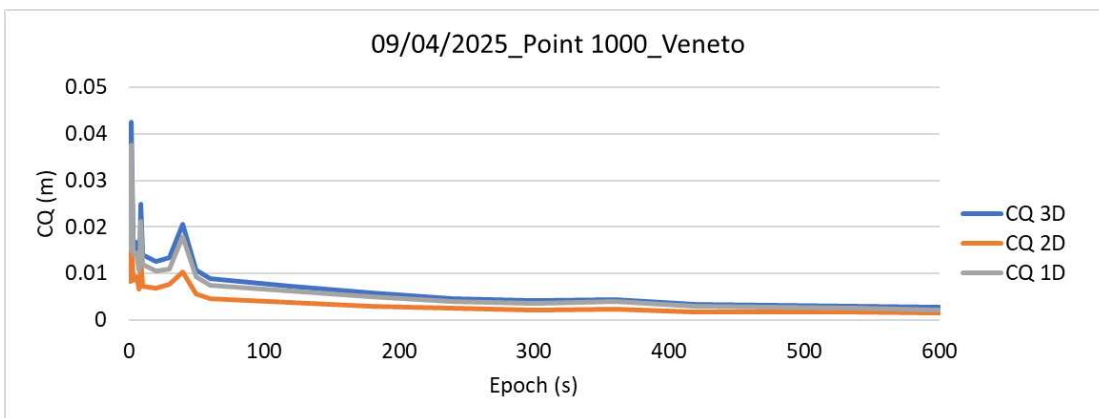


Figure 19: CQ values from epoch 1s to epoch 600s at point 1000

### GDOP trend at point 1000

The Geometric Dilution of Precision (GDOP) begins at a value of 2.8 (figure 20). As the number of epochs increases, GDOP stabilizes around 1.8 between 250 seconds and 550 seconds before slightly increasing to 1.9 at 600 seconds (figure 21). This trend closely mirrors the pattern previously observed in the CQ metric (figure 19).

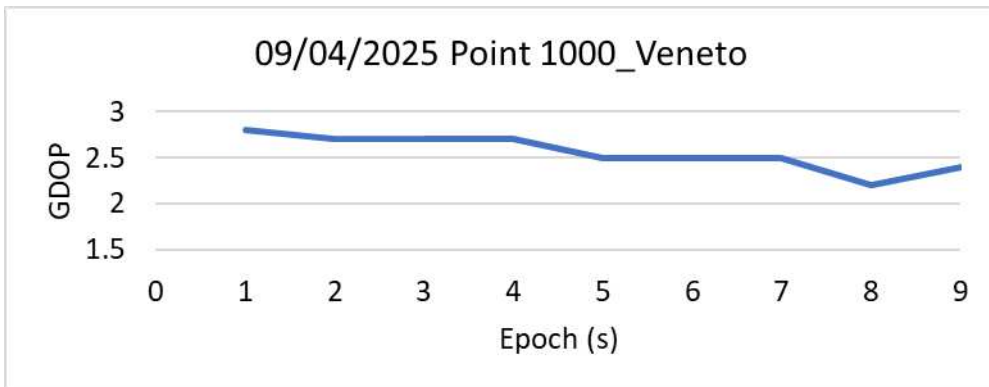


Figure 20: GDOP values from epochs 1s to epoch 9s

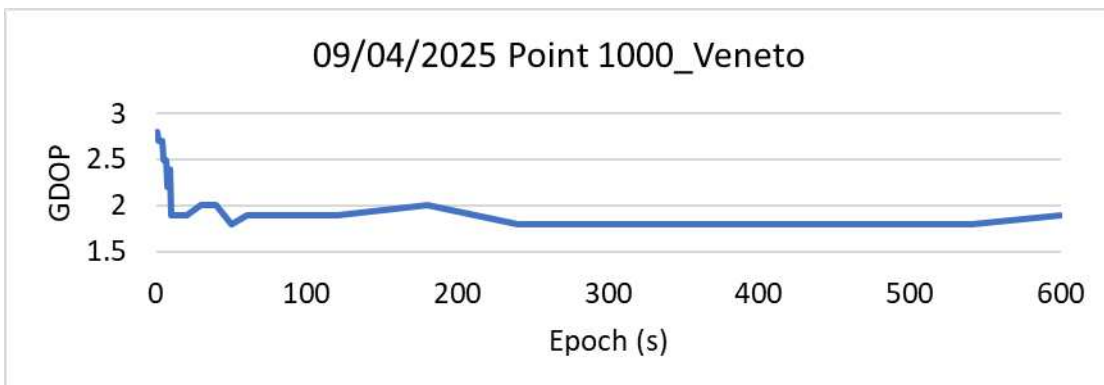


Figure 21: GDOP values from epochs 1s to epoch 600s

### CQ trend at point 2000

Between 1s and 3s, the CQ1D, CQ2D, and CQ3D metrics maintain identical values. A first peak is observed at 4s, after which the values begin to decrease (figure 22). By 9 seconds, CQ2D reaches its minimum value of 0.0091 meter—the lowest recorded for epochs under 10s. Beyond this point, the CQ metrics exhibit a gradual and nearly negligible decline, indicating stabilization. Notably, all three CQ components, along with GDOP, reach their highest value within the first 9 seconds at both Point 1000 and Point 2000. As the number of epochs increases (figure 23), these metrics consistently improve, suggesting that extended observation time enhances positional accuracy.

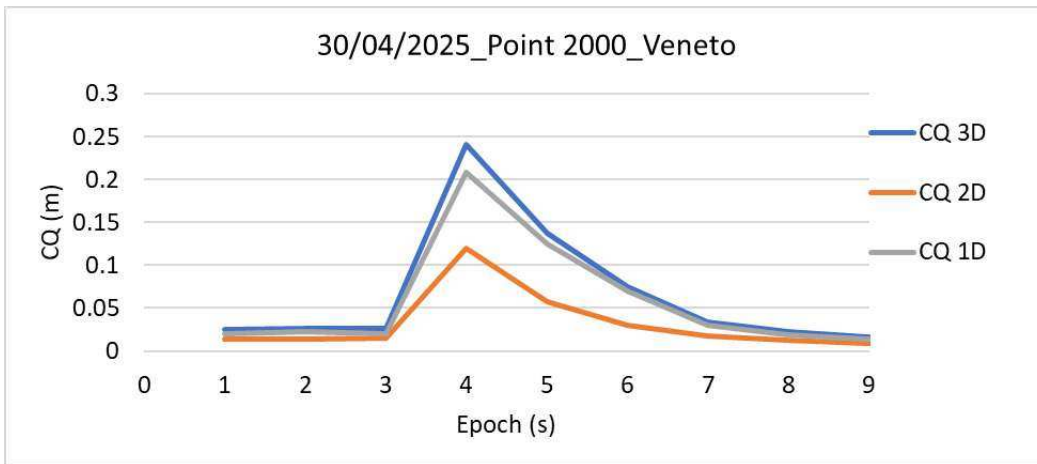


Figure 22: CQ values from epochs 1s to epoch 9s at point 2000

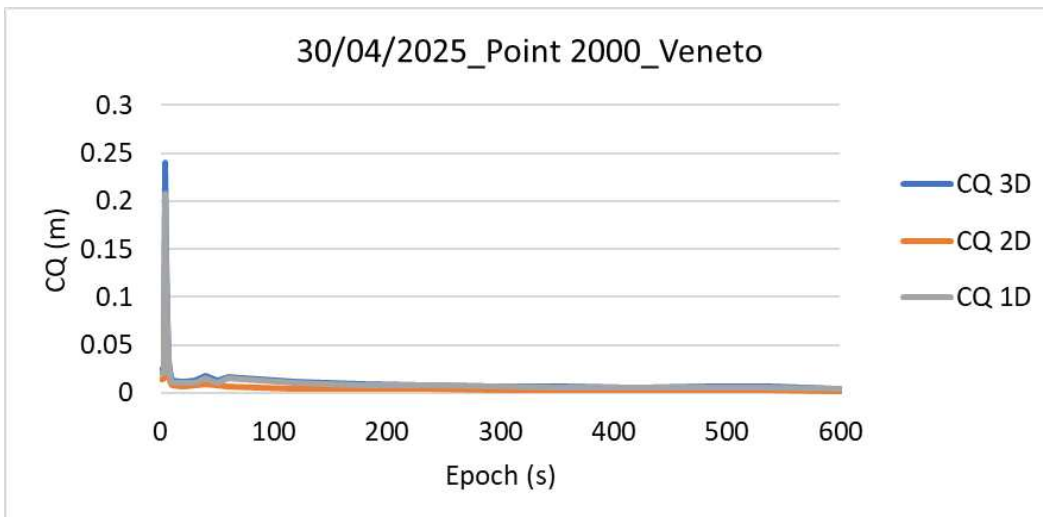


Figure 23: CQ values from epochs 1s to epoch 600s at point 2000

### GDOP trend at point 2000

The GDOP gradually increases over the initial epochs, reaching its maximum value of 12.2 at 6 seconds (figure 24). This high value may be attributed to several factors, including poor satellite geometry due to clustering (i.e., low angular separation), temporary masking of one or more satellites, or a sudden drop in the number of visible satellites. Following this peak, GDOP decreases steadily, reaching its minimum value of 2.2, which suggests a significant improvement in positional accuracy. This value remains relatively stable until approximately 40 seconds (figure 25), when a secondary, though smaller, increase is observed. Beyond this point, GDOP exhibits an alternating pattern, fluctuating between 2.4 and 3.5. In any case, the extension of the observation period seems to benefit the general improvement of the GDOP.

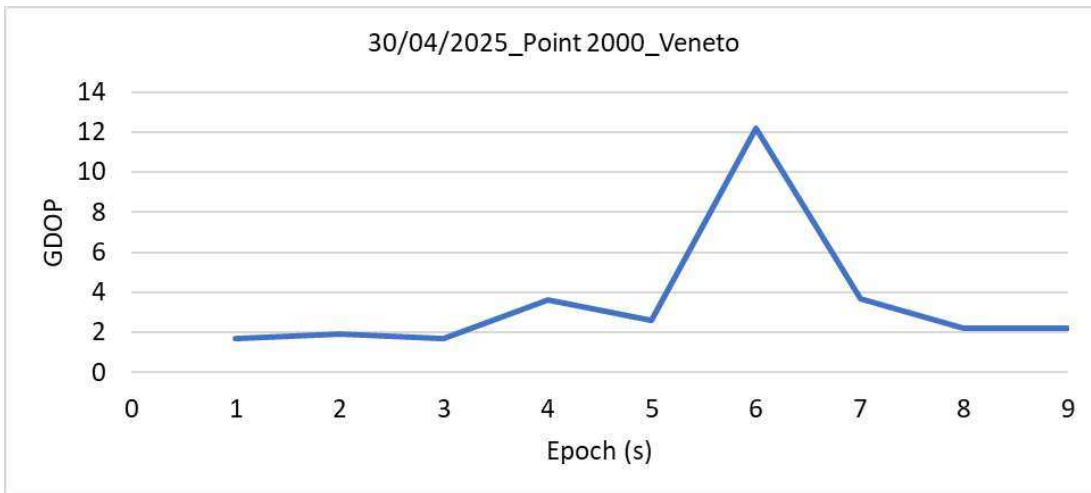


Figure 24: GDOP values from epochs 1s to epoch 9s

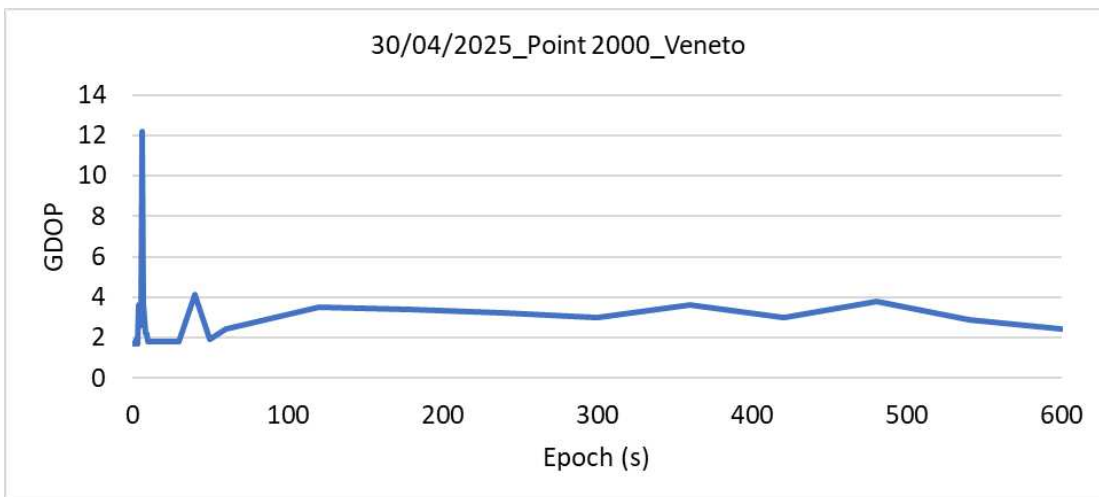


Figure 25: GDOP values from epochs 1s to epoch 600s

### Distance trend

In the short-term interval (figure 26), F12 exhibits a stable and low-amplitude distance difference profile, with values fluctuating narrowly around the zero baseline. This indicates a high degree of short-term consistency, with minimal deviation from the reference distance. Over the extended 600-second interval, this trend persists: F12 continues to demonstrate limited variation, with no significant drift or abrupt changes. The long-term stability (figure 27) reinforces the reliability of F12 for applications requiring sustained positional accuracy, confirming that its short-term precision is maintained over time.

Conversely, F32 shows greater variability in both the short-term and long-term graphs. In the 1–9 second window, F32 fluctuates more widely than F12, with deviations reaching up to  $\pm 0.03$  meter. This pattern is amplified in the long-term graph, where the distance difference ranges from

approximately  $-0.03$  to  $+0.05$  meter. The broader amplitude and more frequent oscillations suggest that F32 is more sensitive to dynamic changes or may be subject to higher measurement noise. While it captures the same general motion trend as F12, its reduced stability over time may limit its suitability for high-precision or long-duration tracking tasks.

The comparative analysis confirms that F12 maintains superior consistency and alignment with the reference trajectory across both short and long durations. F32, while responsive to the same motion patterns, exhibits greater variability, which may reflect differences in sensor calibration, filtering, or environmental sensitivity. These findings highlight the importance of evaluating both short- and long-term behavior when assessing the reliability of positioning systems.

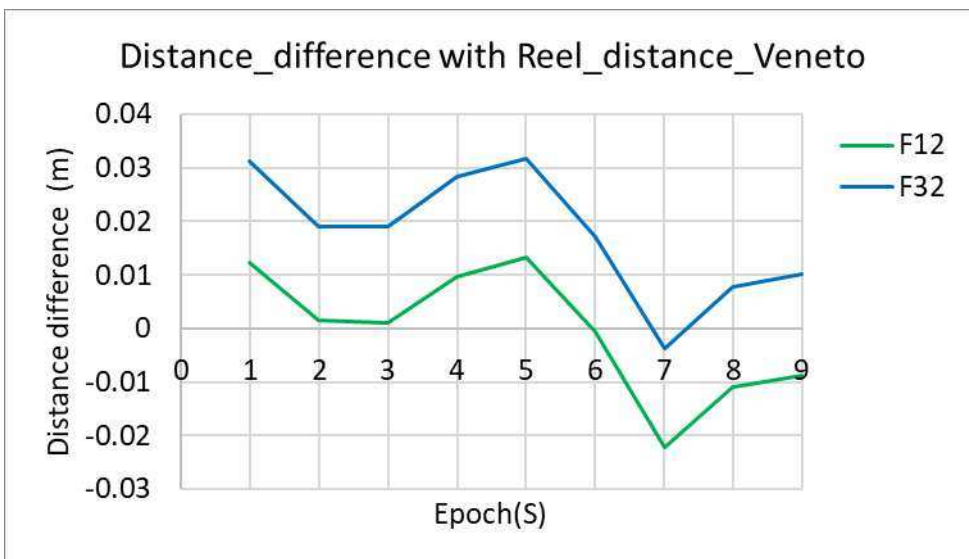


Figure 26: Distance difference between point 1000 and 2000 from Epoch 1s to 9s

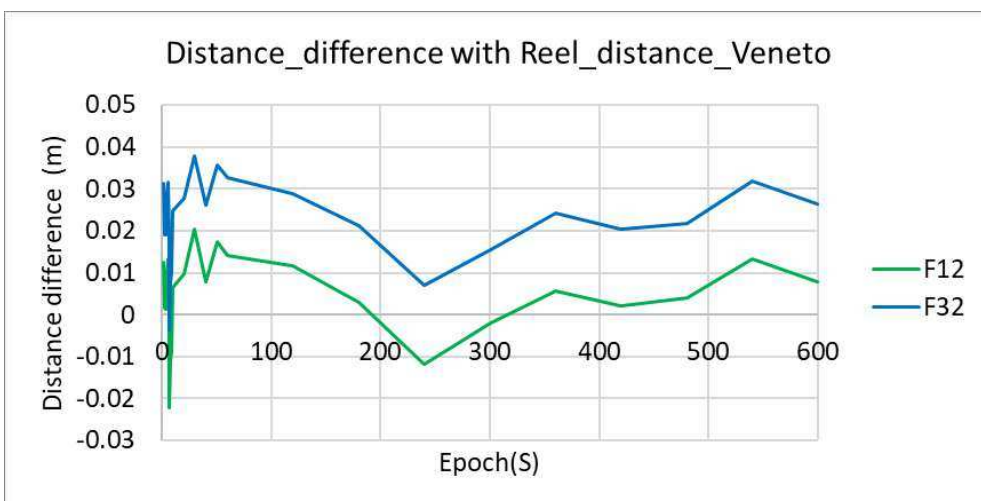


Figure 27: Distance difference between point 1000 and 2000 from Epoch 1s to 600s

## Elevation trend

The evolution of the elevation difference (figure 28) closely mirrors that of the distance difference, following a similar overall trend. On average, the magnitude of the elevation difference is approximately 0.0169 m, indicating a high level of accuracy, but worse than horizontal positioning.

The error was in the order of 3 cm with observations acquired up to 240 seconds (figure 29). In the longest observation periods, the maximum error was 2 cm.

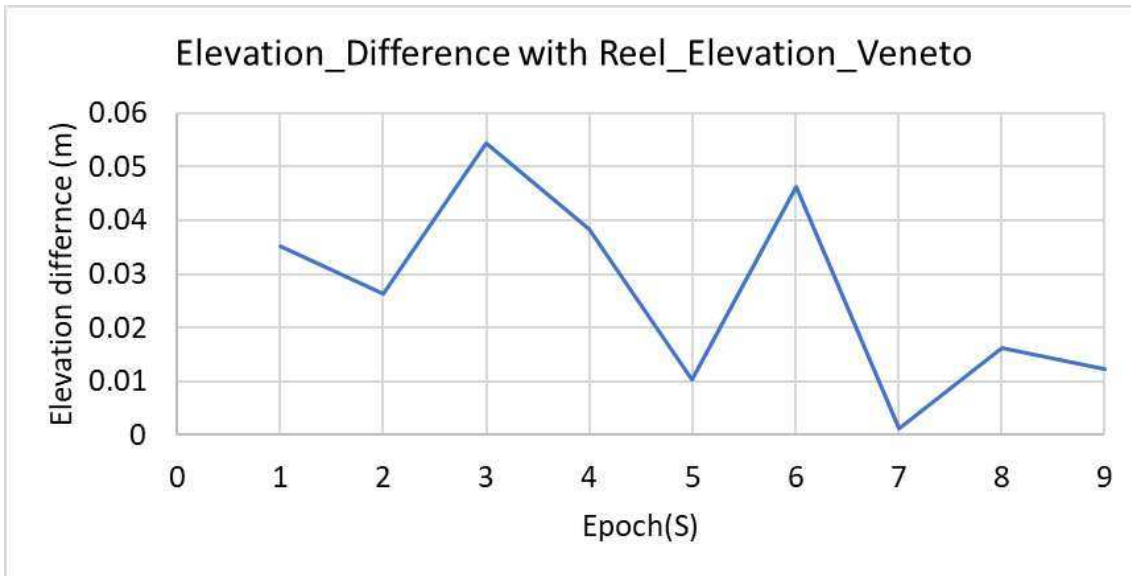


Figure 28: Distance difference between point 1000 and 2000 from Epoch 1s to 9s

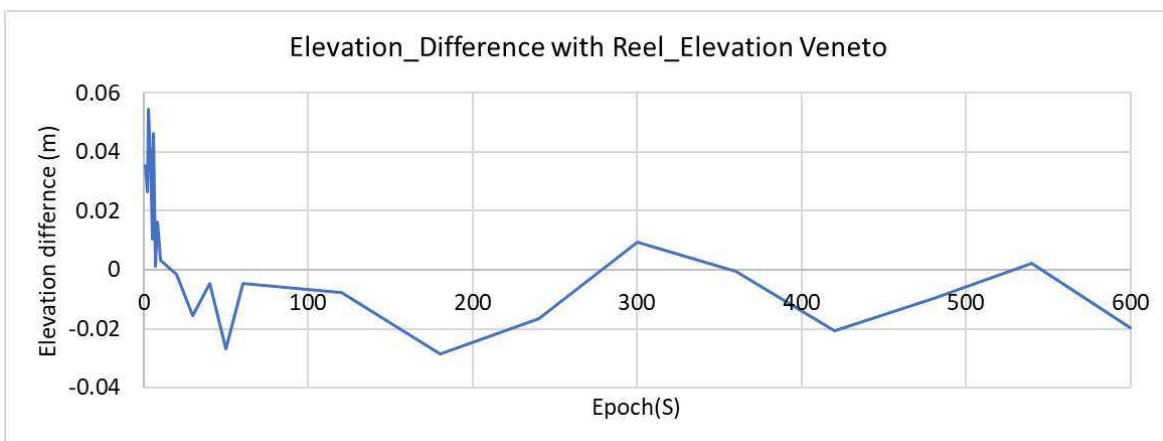


Figure 29: Elevation difference between point 1000 and 2000 from Epoch 1s to 600s

### **3.1.2. HXGN trend**

#### **3.1.2.1. HXGN trend for measurements carried out on 19<sup>th</sup> March 2025**

##### **CQ**

###### **Trend at point 1000**

The CQ metrics exhibit a similar temporal pattern, with CQ3D consistently showing the highest values, indicating the lowest accuracy among the three components. Four major peaks are observed, the most prominent occurring within the first 50 seconds: 0.0144 meter at 3 seconds (figure 30) and 0.0138 meter at 30 seconds. Between 30 and 300 seconds, a steady improvement in accuracy is noted. The remaining two peaks appear at 360 seconds (0.0078 meter) and 540 seconds (0.0121 meter) (figure 31). Following the latter, the CQ reaches its minimum value of 0.0024 m, signifying optimal theoretical positioning accuracy.

###### **Comparison with Veneto R. at the point 1000**

The comparative analysis of CQ values across 3D, 2D, and 1D dimensions between HXGN measurements in March and Veneto R. reveals both consistent trends and notable divergences. Overall, the CQ values from Veneto R. tend to be slightly higher, with mean differences of +0.0035 meter in 3D, +0.0017 meter in 2D, and +0.0030 meter in 1D. Despite these differences in magnitude, the temporal evolution of the CQ values across epochs exhibits a largely parallel trend between the two datasets. Both March and Veneto R. data show a general decline in CQ values over time, reflecting improved precision or reduced variability in later epochs. However, specific intervals—particularly around Epochs 2 seconds, 9 seconds, and 13 seconds—highlight sharp increases in Veneto R. values compared to March, suggesting localized deviations possibly due to environmental or instrumental factors. Conversely, in the final epochs, the CQ values converge more closely, indicating a stabilization in measurement quality. These findings underscore a shared underlying trend in spatial quality metrics, while also emphasizing the importance of monitoring localized anomalies that may influence geospatial reliability.

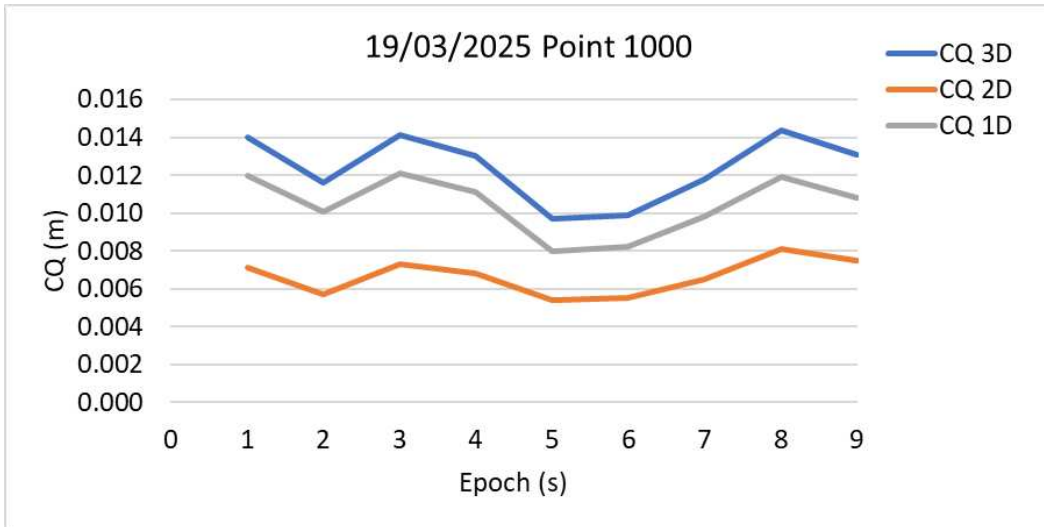


Figure 30: CQ values at point 1000 on 19/03/2025 from Epoch 1s to 9s

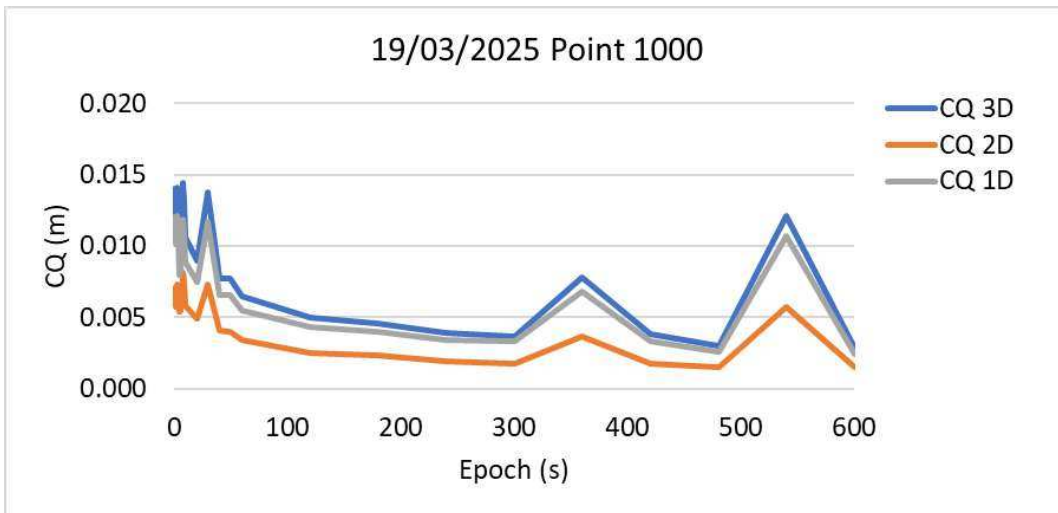


Figure 31: CQ values at point 1000 on 19/03/2025 from Epoch 1s to 600s

**GDOP**

**Trend at point 1000**

The GDOP reaches its maximum value of 2.2 at 1 second (figure 32), followed by a decrease to 1.7 at 2 seconds. After 50 seconds, two prominent peaks of equal magnitude (1.9) are observed—first at 180 seconds and again at 540 seconds (figure 33). Following the latter, GDOP decreases to its minimum value of 1.4, indicating the highest level of positional accuracy within the observation period.

### Comparison with Veneto R. at point 1000

The GDOP values for both the Veneto R. and HXGN GNSS networks exhibit a broadly similar temporal trend characterized by an initial decline followed by stabilization, reflecting the typical behavior of satellite geometry optimization over time. However, notable differences emerge in the magnitude and consistency of these trends. The Veneto R. datasets begin with higher GDOP values, peaking at 2.8, and although it gradually decreases, it remains relatively elevated and variable throughout the epochs. In contrast, HXGN starts with a lower GDOP and demonstrates a more rapid and consistent decline, stabilizing around 1.7 with minimal fluctuation. This suggests that HXGN achieves optimal satellite geometry more efficiently and maintains it more reliably than Veneto R.; despite these differences, both networks converge toward a steady-state performance in later epochs, indicating comparable long-term stability. The resemblance in trend shape underscores shared underlying GNSS dynamics, while the divergence in GDOP magnitude and variability highlights HXGN's superior geometric configuration and operational consistency.

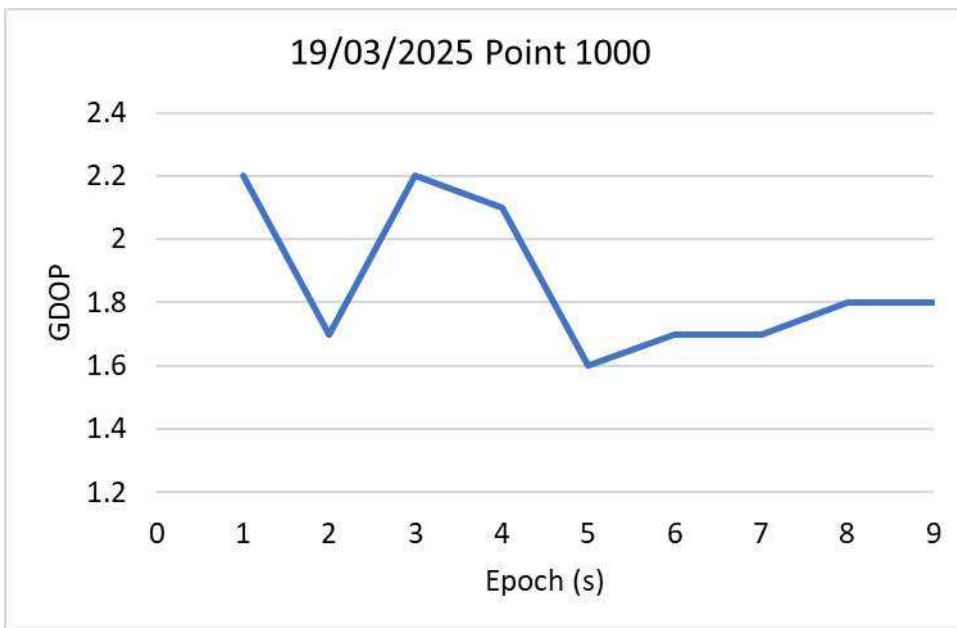


Figure 32: GDOP values at point 1000 on 19/03/2025 from Epoch 1s to 9s

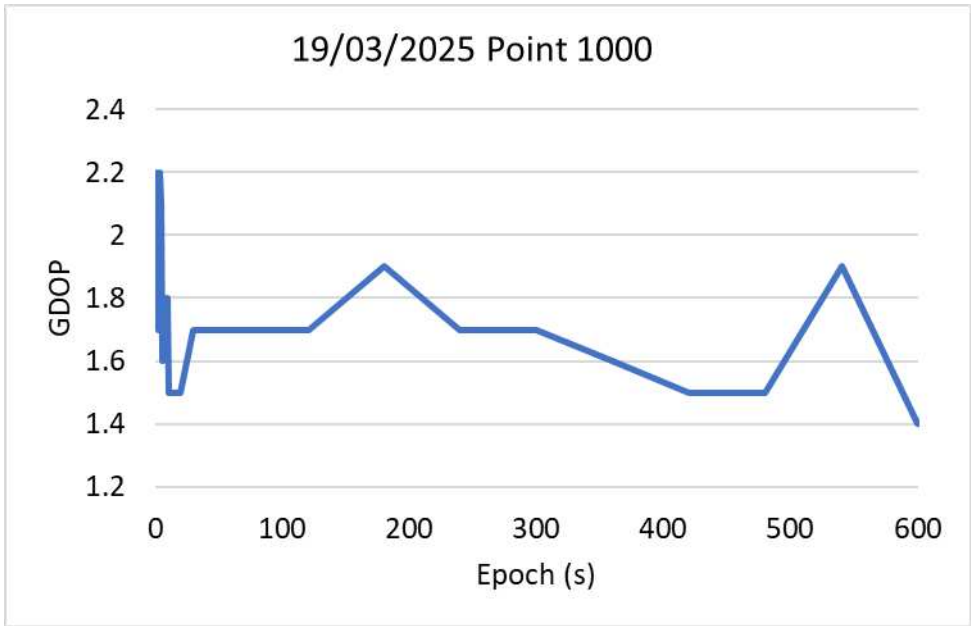


Figure 33: GDOP values at point 1000 on 19/03/2025 from Epoch 1s to 600s

**CQ**

**Trend at point 2000**

The short-duration plot provides a magnified view of the initial 9 seconds (figure 34), during which all CQ metrics appear more stable. CQ 3D, CQ 2D, and CQ 1D remain within a narrow band, indicating consistent coordinate quality during the early phase of data acquisition. This stability may reflect favorable satellite visibility and minimal environmental interference at the start of the observation period.

In the long-duration plot (figure 35), all three CQ metrics exhibit fluctuations over time, with CQ 3D generally showing higher variability compared to CQ 2D and CQ 1D, as expected. The CQ 3D values range up to approximately 0.0120 meter, indicating periods of reduced positional precision in three-dimensional space. CQ 2D and CQ 1D maintain relatively lower and more stable values, suggesting better consistency in horizontal and vertical positioning, respectively. These fluctuations may be attributed to changes in satellite geometry.

Overall, the CQ metrics demonstrate a dynamic but generally improving trend in theoretical coordinate precision over time. The lower and more stable CQ values in the long-duration plot suggest optimal conditions for initial positioning, while the short-duration plot highlights the importance of monitoring CQ variations for sustained accuracy in GNSS applications.

### Comparison with Veneto R. at point 2000

A comparative evaluation of CQ values at point 2000 between March measurements through HXGN and Veneto R. across 24 epochs reveals a consistent trend of higher positional uncertainty in the Veneto R. dataset across all dimensions. The average CQ values in Veneto R. exceed those in March by approximately 0.0246 meter in 3D, 0.0116 meter in 2D, and 0.0215 meter in 1D, indicating a systematic elevation in measurement variability. Despite these differences in magnitude, both datasets exhibit a similar downward trend over time, reflecting progressive improvements in spatial precision or stabilization of measurement conditions. However, Veneto R. data show pronounced spikes in CQ values at early epochs—most notably at epochs 4 seconds and 5 seconds—where 3D values reach 0.2404 meter and 0.1376 meter respectively, contrasting sharply with March values below 0.012 meter. Beyond these anomalies, the convergence of CQ values in later epochs suggests a harmonization in measurement quality, underscoring both the temporal consistency and episodic divergence in spatial accuracy between the two datasets.

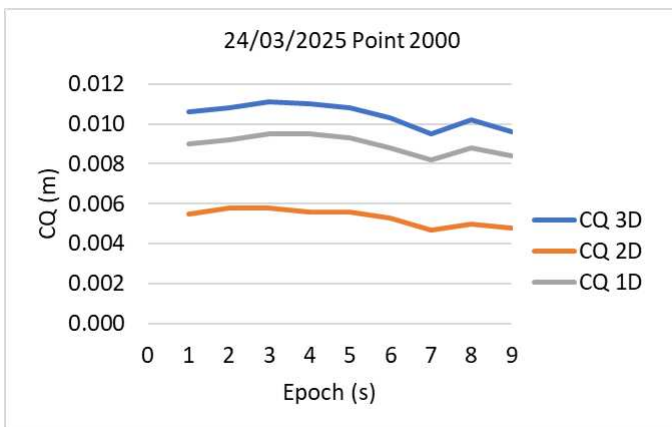


Figure 34: CQ values at point 2000 on 24/03/2025 from Epoch 1s to 9s

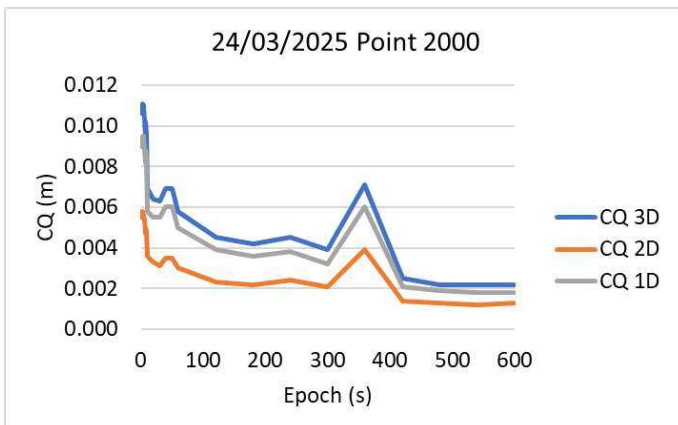


Figure 35: CQ values at point 2000 on 24/03/2025 from Epoch 1s to 600s

## **GDOP**

### **Trend at point 2000**

The short-duration plot (figure 36) provides an overall mapping of the initial 9 seconds, capturing the transient dynamics of GDOP during system initialization or satellite acquisition. The GDOP decreases from 1.7 to 1.5 within the first two seconds, followed by minor fluctuations between 1.4 and 1.6. This behavior is characteristic of the receiver's rapid adaptation to changing satellite visibility conditions.

In the long-duration plot (figure 37), the GDOP initially registers a value of approximately 1.7, indicating suboptimal satellite geometry. A rapid decrease is observed within the first few seconds, stabilizing around 1.4. This suggests a swift improvement in satellite configuration, likely due to the acquisition of additional satellites or favorable changes in their spatial distribution. Between 360 and 400 seconds, a moderate increase in GDOP to ~1.5 is noted, followed by a steady decline to approximately 1.2 by the end of the observation period. This final value reflects a highly favorable satellite geometry, conducive to high-precision positioning.

### **Comparison with Veneto R. trend**

The GDOP values across the two datasets from Veneto R. at point 2000, and HXGN at point 2000—exhibit distinct patterns in terms of accuracy and stability. Veneto R. at point 2000 displays the highest variability, with a mean GDOP of 3.10 and a standard deviation of 2.04, indicating significant fluctuations in satellite geometry. This dataset also contains the most pronounced peak, reaching 12.2 at epoch 6 seconds, suggesting a moment of severely degraded positional precision. In contrast, HXGN at Point 2000 demonstrates the most consistent and reliable performance, with the lowest mean GDOP of 1.46 and a standard deviation of 0.08, peaking modestly at 1.7 at epoch 1 second. All two datasets exhibit a general trend of stabilization over time, but the magnitude and timing of their peaks—especially the sharp spike in Veneto R. at Point 2000—highlight the superior geometric configuration and operational stability of the HXGN.

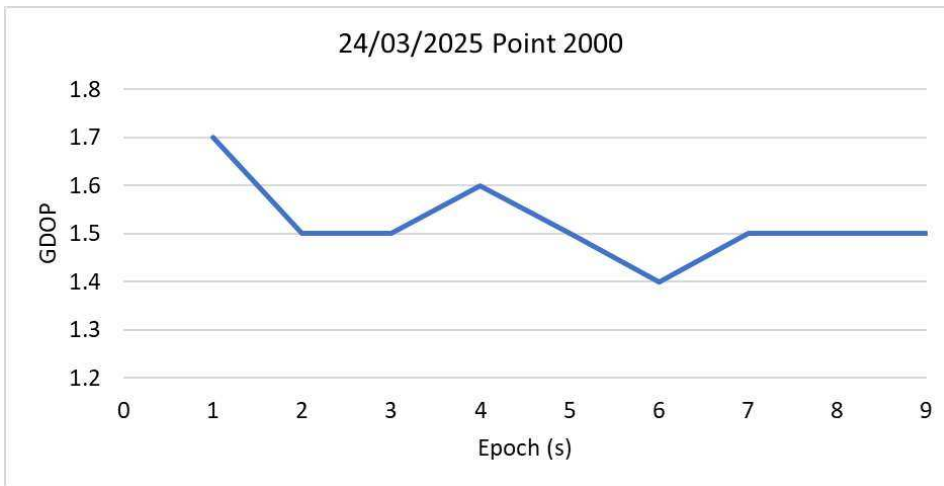


Figure 36: GDOP values at point 2000 on 24/03/2025 from Epoch 1s to 9s

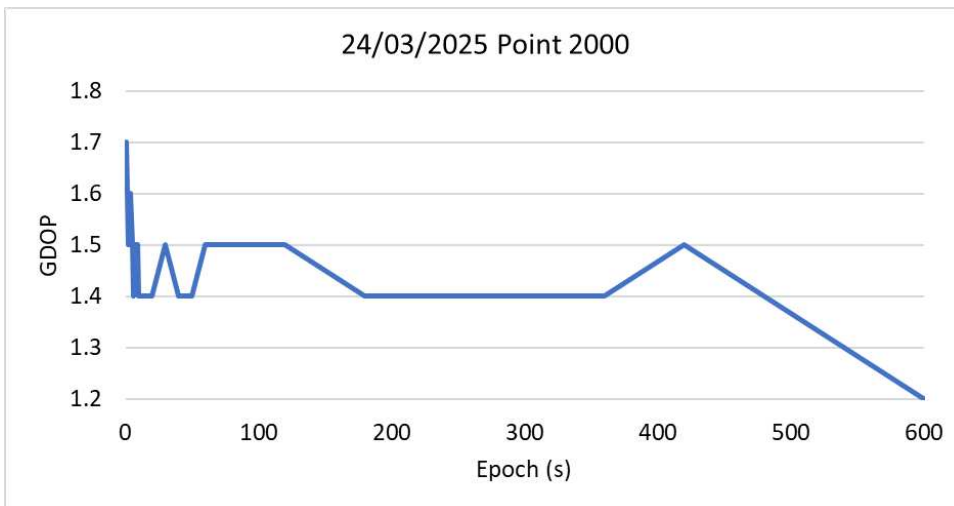


Figure 37: GDOP values at point 2000 on 24/03/2025 from Epoch 1s to 600s

### Distance difference

#### Overall trend

During the short-duration interval (1–9 second), the F32 baseline exhibits significantly higher distance differences compared to F12 (figure 38), with a mean of 0.02528 meter and a standard deviation of 0.00296 meter, versus F12’s mean of 0.00703 meter and standard deviation of 0.00281 meter. These results indicate that F32 not only maintains larger deviations but also demonstrates slightly greater variability in its measurements. Both baselines reach their respective peaks at epoch 4 seconds, where F12 records a maximum deviation of 0.01067 meter and F32 peaks at 0.02877 meter, suggesting a shared moment of increased positional discrepancy. The consistently elevated values of F32 across all epochs point to structural or geometric differences in the baseline configurations, with F32 likely spanning a longer or more complex path, thereby accumulating

greater measurement deviations. Despite these differences, the parallel trend and synchronized peak imply that both baselines are influenced by similar temporal or environmental factors affecting HXGN's performance.

The reduced temporal scale facilitates a clearer comparison of short-term consistency, where F12 appears slightly more stable than F32. Notably, when using the Zone 12 reference system (F12), horizontal distance errors remain within 1 centimeter, which is considered a highly accurate result (figure 38).

Over the long-duration interval (10–600 seconds) (figure 39), the F12 baseline exhibits a mean distance difference of  $-0.00322$  meter with a standard deviation of  $0.01885$  meter, indicating a slight overall contraction and moderate variability. In contrast, the F32 baseline shows a positive mean of  $0.01506$  meter and a comparable standard deviation of  $0.01891$  meter, suggesting a general expansion trend with similar fluctuation. Both baselines reach their maximum deviations at epoch 360 s, where F12 peaks at  $-0.05854$  meter and F32 at  $0.07748$  meter, marking a significant and synchronized anomaly. This shared peak likely reflects a common external influence—such as atmospheric disturbances or satellite geometry shifts—affecting both baselines simultaneously (Lu et al., 2025). While F32 consistently maintains higher values than F12, the presence of negative deviations in both series, particularly in F12, highlights periods of contraction or measurement reversal. Overall, F32 demonstrates a more consistently positive and expansive behavior, whereas F12 reflects a more oscillatory pattern with a slight bias toward negative deviations.

### **Comparison with Veneto R. Distance difference trend**

The comparative analysis of distance differences across the HXGN and Veneto R., specifically for baselines F12 and F32, reveals both converging patterns and notable divergences in measurement behavior. A common feature among all four baselines is the presence of temporal variability, with fluctuations in distance differences observed across epochs. Each baseline exhibits a distinct peak, indicating moments of maximum deviation. Notably, both HXGN F12 and F32 reach their highest values at epoch 360 seconds (approximately 6 centimeters), coinciding with the peaks in CQ metrics for Points 1000 and 2000, despite favorable GDOP conditions. Excluding this anomaly, horizontal distance errors remain within 3 centimeters for observation periods between 50 and 240 seconds. For longer durations, the maximum error is limited to 2 centimeters, aligning with the performance observed in the Veneto R. for horizontal distances. Similarly, Veneto R. F12 and F32 both exhibit a peak at epoch 30 seconds, indicating a synchronized but earlier response within that network. This

alignment of peak epochs within each network suggests internal consistency in how each system responds to environmental or operational factors.

Despite these structural similarities, the baselines differ significantly in magnitude and stability. HXGN F32 shows the highest mean distance difference (0.01506 meter) and the most pronounced peak (0.07748 meter), reflecting a more expansive and variable measurement profile. In contrast, HXGN F12 has a slightly negative mean ( $-0.00322$  meter), indicating a tendency toward contraction, and exhibits the widest range of fluctuation, with values spanning from  $-0.04542$  meter to 0.05854 meter. The Veneto R. baselines demonstrate greater stability: Veneto R. F12 maintains a modest mean of 0.00437 meter with the lowest standard deviation (0.00986 meter), while Veneto R. F32 records the highest average among all baselines (0.02259 meter) but with relatively low variability. Furthermore, negative values are more prevalent in the HXGN baselines, particularly F12, whereas Veneto R. F32 remains consistently positive, suggesting a more uniform expansion behavior.

The analysis of distance differences also reveals a non-linear and dynamic behavior for both F12 and F32, with F32 consistently exhibiting larger and more variable deviations. This pattern indicates that F12 offers a more stable and reliable alignment with the reference system, particularly in applications demanding high-precision positioning. The observed discrepancies are primarily attributed to cartographic distortions inherent in the coordinate systems. Specifically, Zone 12 (F12) functions as a reference system that is free from significant cartographic deformations within the Veneto R., particularly in the area surrounding Padova. In contrast, UTM Zone 32 (F32) is subject to systematic cartographic distortions throughout the same region. As a result, the increased positional errors associated with F32 are consistent with expectations based on its geodetic characteristics.

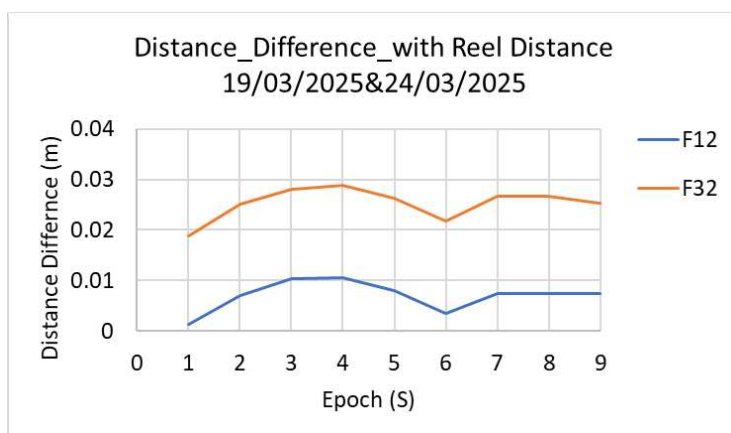


Figure 38: Distance difference for HXGN as per the data collected on 19/03/2025 and 24/03/2025 from Epoch 1s to 9s

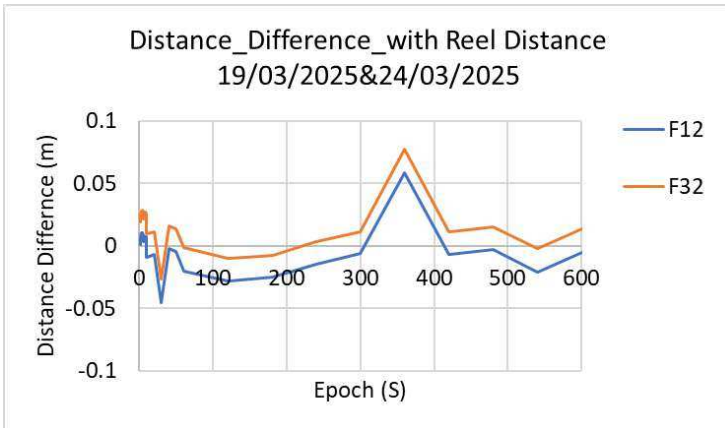


Figure 39: Distance difference for HXGN as per the data collected on 19/03/2025 and 24/03/2025 from Epoch 1s to 600s

### Elevation difference

#### Overall trend

In the analysis of elevation differences using precise data, the maximum value is observed at 30 seconds, reaching 0.0763 meter, while the minimum value of  $-0.0027$  meter occurs at 5 seconds (figure 40). The variation over time is characterized by a series of alternating peaks, fluctuating between positive and negative values. This pattern suggests dynamic changes in vertical positioning accuracy, potentially influenced by satellite geometry, signal quality, or environmental factors. The graphic suggests very good accuracies with observations acquired for at least 480 seconds (figure 41). Accuracies obtained with Veneto R. were better (3 centimeter with observation acquired in at least 7 seconds).

#### Comparison with Veneto R. trend

The comparative analysis of elevation differences between the HXGN and Veneto R. reveals both clear resemblances and significant divergences in vertical positioning behavior across specific epochs. A key resemblance between the two networks is the presence of alternating positive and negative elevation values, reflecting similar environmental or geometric influences. This similarity is particularly evident at epoch 1 second, where HXGN and Veneto R. record nearly identical elevation differences of 0.034 meter and 0.035 meter, respectively, with a minimal difference of 0.001 meter. Other epochs showing close alignment include epoch 2 seconds (difference of 0.005 meter), epoch 10 seconds (0.007 meter), epoch 20 seconds (0.010 meter), epoch 40 seconds (0.002 meter), epoch 180 seconds (0.001 meter), and epoch 600 seconds (0.001 meter). These instances suggest moments of consistent vertical measurement behavior between the two networks. In contrast, the networks

diverge significantly at several epochs, indicating differences in sensitivity or response to external conditions. The most pronounced divergence occurs at epoch 30 seconds, where HXGN records a peak elevation of 0.076 m while Veneto R. shows  $-0.016$  m, resulting in a substantial difference of 0.092 m. Other notable divergences include epoch 6 seconds (difference of 0.063 meter), epoch 300 seconds (0.068 meter), epoch 3 seconds (0.039 meter), epoch 8 seconds (0.031 meter), epoch 240 seconds (0.032 meter), and epoch 420 seconds (0.034 meter). These discrepancies highlight moments where the HXGN exhibits sharper peaks or deeper troughs compared to the more moderate behavior of the Veneto R.

In summary, while both networks share a common pattern of elevation fluctuation and occasional alignment, the HXGN demonstrates greater variability and more extreme deviations, particularly at epochs 30s and 300s. The Veneto R. network, by contrast, maintains more consistent and balanced elevation measurements, with closer alignment to HXGN at several epochs, especially early and late in the observation period.

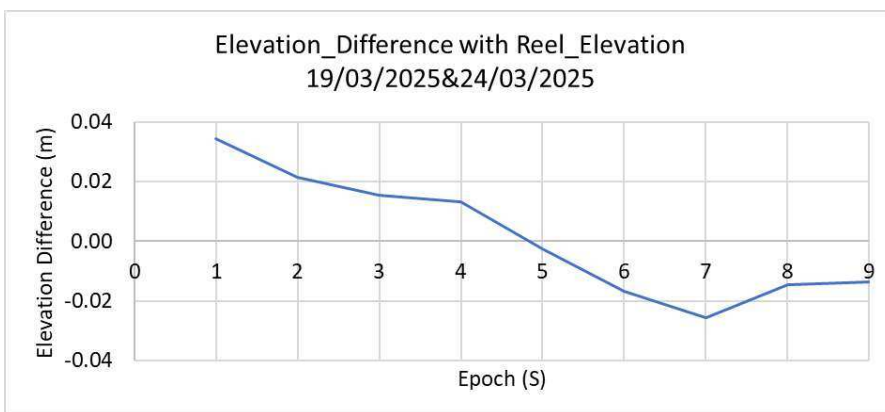


Figure 40: elevation difference for HXGN as per the data collected on 19/03/2025 and 24/03/2025 from Epoch 1s to 9s

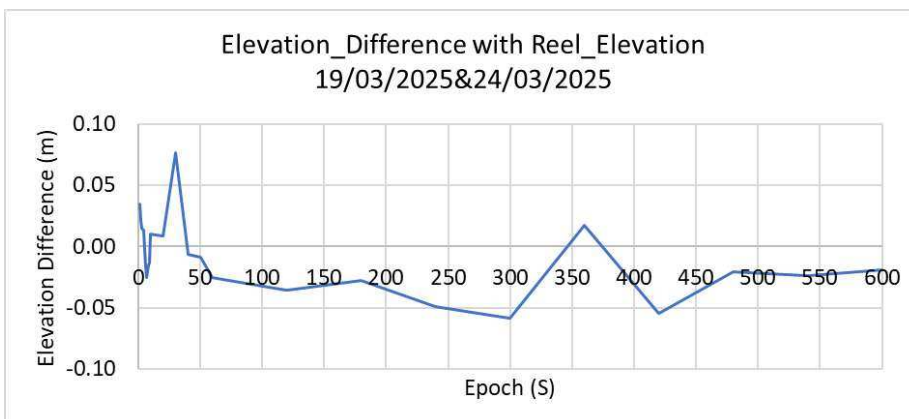


Figure 41: Elevation difference for HXGN as per the data collected on 19/03/2025 and 24/03/2025 from Epoch 1s to 9s

### 3.1.2.2. HXGN trend for measurements carried out on 2<sup>nd</sup> April 2025

#### CQ

##### Trend at the point 1000

As shown in the previous representation of CQ values, CQ2D consistently demonstrates the highest precision, followed by CQ1D and CQ3D (figure 42). This ordering aligns with expectations, as horizontal dilution of precision is generally less affected by ionospheric and tropospheric delays compared to vertical components (Setti, et al., 2025). Additionally, the CQ values at Point 1000 exhibit a more pronounced oscillatory pattern, with relatively high amplitude variations, whereas Point 2000 shows a smoother evolution with lower amplitude fluctuations. The highest CQ values for point 1000 are observed at 8 seconds, reaching 0.0144 meter, 0.0119 meter, and 0.0081 meter for CQ3D, CQ1D, and CQ2D, respectively. Conversely, the lowest values occur at 5 seconds across all components, corresponding to 0.0097 meter (CQ3D), 0.0080 meter (CQ1D), and 0.0054 meter (CQ2D).

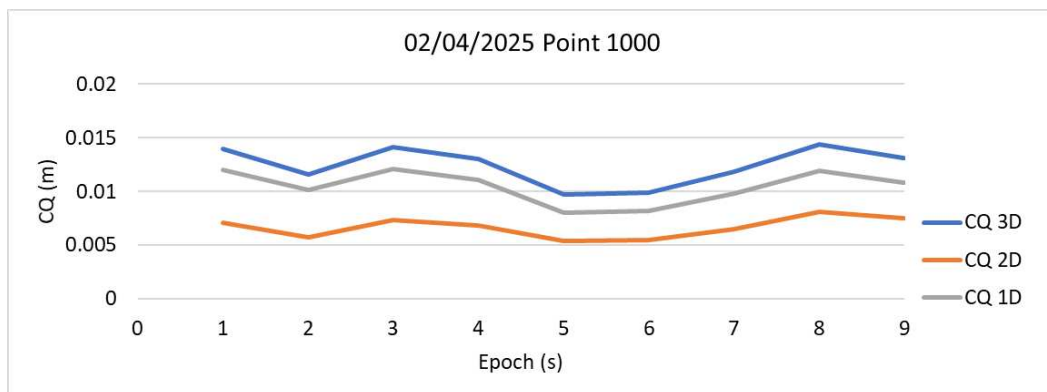


Figure 42: CQ values for HXGN as per 02/04/2025 measurements at point 1000

##### Comparison with measurements conducted with Veneto R. at point 1000

The trend analysis of HXGN and Veneto R. measurements conducted on the 2<sup>nd</sup> of April reveals both clear resemblances and distinct differences in their temporal evolution across nine epochs. In terms of resemblance, both datasets exhibit smooth and consistent progression in CQ 3D, CQ 2D, and CQ 1D values, with similar curve shapes and gradual changes over time, indicating stable measurement conditions. For instance, both HXGN and Veneto R. show rising values around Epochs 1 second and 3 second, followed by a slight dip near Epochs 5 seconds and 6 seconds, and a recovery toward Epoch 8 seconds. However, the differences are marked in magnitude and variability. HXGN measurements remain tightly clustered, with CQ 3D peaking at 0.0144 m in Epoch 8 seconds and

maintaining low variability throughout. In contrast, Veneto R. displays significantly higher values and greater fluctuation, most notably at Epoch 2 seconds where CQ 3D and CQ 1D spike to 0.0426 meter and 0.0375 meter respectively—far exceeding the HXGN range and indicating a potential anomaly. Overall, while the temporal patterns of both datasets align in structure, HXGN demonstrates superior consistency and lower magnitudes, whereas Veneto R. shows higher dispersion and episodic deviations.

## CQ

### Trend at the point 2000

The analysis of CQ values reveals a consistent trend of improving measurement precision across all dimensions—3D, 2D, and 1D. Initially, the CQ 3D values show a slight increase, peaking at 0.0111 meter, followed by a gradual decline to 0.0096 meter, indicating stabilization in spatial accuracy (figure 43). CQ 2D values follow a similar pattern, starting at 0.0055 meters and decreasing steadily to 0.0048 meters, suggesting enhanced planar precision over time. CQ 1D values also exhibit a downward trend, from 0.009 meters to a low of 0.0082 meters, with minor fluctuations. This overall decline in CQ values across all dimensions suggests that the measurement system experienced initial variability—possibly due to environmental or instrumental factors—before reaching a more stable and precise state.

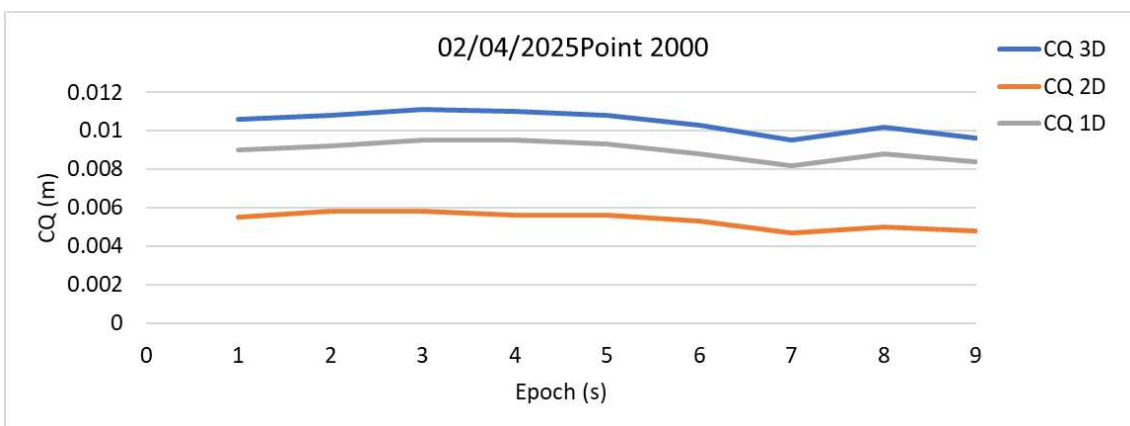


Figure 43: CQ values for HXGN as per 02/04/2025 measurements at point 2000

### Comparison with measurements conducted with Veneto R. at point 2000

The comparative analysis between HXGN and Veneto R. measurements reveals a shared downward trend across CQ 3D, CQ 2D, and CQ 1D dimensions over the nine epochs, indicating a general resemblance in temporal behavior. Both datasets show decreasing values from epoch 1 second to

Epoch 9 seconds, such as CQ 3D dropping from 0.0106 meter to 0.0096 meter for HXGN and from 0.0246 meter to 0.0162 meter for Veneto R.; however, the differences are pronounced in magnitude and variability: HXGN measurements remain consistently low and stable, with CQ 3D values ranging narrowly between 0.0095 meter and 0.0111 meter, while Veneto R. exhibits significant fluctuations, particularly at Epochs 4 seconds and 5 seconds where CQ 3D spikes to 0.2404 meter and 0.1376 meter, and CQ 1D reaches 0.2082 meter and 0.1251 meter respectively—values far exceeding HXGN’s range. These peaks in the Veneto R. dataset contrast sharply with HXGN’s steady trend, highlighting the superior precision and consistency of HXGN measurements versus the higher dispersion and episodic anomalies observed in Veneto R. dataset.

## GDOP

### Trend at point 1000

The GDOP measurements at point 1000 (figure 44), recorded across nine sequential epochs, exhibit a clear declining and stabilizing trend. During the initial epochs (1 to 3 seconds), GDOP values fluctuate between 2.2 and 1.7, indicating unstable satellite geometry and reduced positional reliability. From Epoch 4 seconds onward, the values begin to decrease, reaching a minimum of 1.6 at Epoch 5 seconds, and then stabilize between 1.7 and 1.8 through Epochs 6 seconds to 9 seconds. This progression reflects a transition from higher to lower geometric dilution of precision, suggesting that satellite configuration improved over time, resulting in more favorable conditions for accurate GNSS positioning.

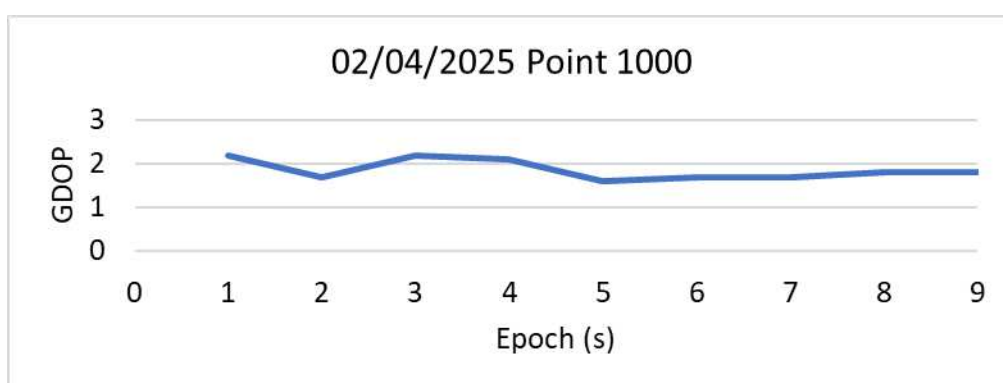


Figure 44: GDOP values for HXGN as per 02/04/2025 measurements at point 1000

### Comparison with measurements conducted through Veneto R. at point 1000

The comparison of GDOP values between HXGN and Veneto R. across nine epochs reveals a shared downward trend in geometric precision, with both datasets showing decreasing values from Epoch

1 second to Epoch 8 seconds—HXGN from 2.2 to 1.8 and Veneto R. from 2.8 to 2.2—indicating a common temporal pattern. However, the differences are evident in magnitude and consistency: Veneto R. consistently exhibits higher GDOP values, especially between Epochs 2 seconds and 4 seconds where it remains at 2.7, while HXGN fluctuates between 1.7 and 2.2. The smallest gap occurs at Epoch 8 seconds, where HXGN records 1.8 and Veneto R. 2.2, yet the disparity persists. Overall, while both systems follow a similar trend, HXGN demonstrates superior geometric precision with lower and more stable GDOP values, whereas Veneto R. shows consistently higher and less precise readings throughout the observed period.

## GDOP

### Trend at point 2000

The CQ values recorded across nine epochs (figure 45) reveal a distinct trend of initial increase followed by gradual decline and stabilization in measurement precision. CQ 3D values profile rises slightly from 0.0106 to a peak of 0.0111 by epoch 3 seconds, then progressively decreases to 0.0096 by epoch 9 seconds, indicating improved spatial consistency. CQ 2D values follow a similar pattern, peaking at 0.0058 in Epochs 2 seconds and 3 seconds before declining to 0.0048, reflecting enhanced planar accuracy. CQ 1D values also show a peak of 0.0095 in Epochs 3 seconds and 4 seconds, followed by a steady decrease to 0.0084. This overall downward trend across all dimensions suggests a transition from higher variability to more stable and precise measurements, likely due to improved environmental conditions or system calibration over time.

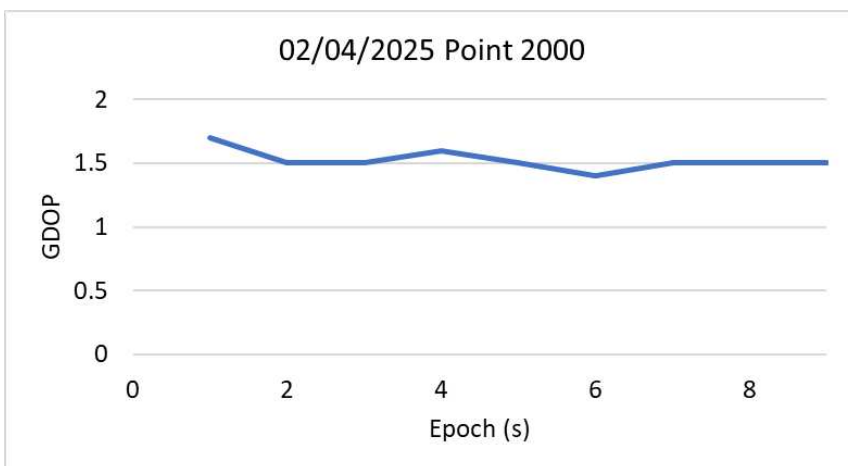


Figure 45: GDOP values for HXGN as per 02/04/2025 measurements at point 1000

### **Comparison with measurements using Veneto R.**

Both datasets follow a similar downward trajectory, with GDOP values decreasing from Epoch 1 second to Epoch 8 seconds—HXGN from 2.2 to 1.8 and Veneto R. from 2.8 to 2.2—indicating a common temporal pattern in improving geometric precision. However, the differences are striking. Veneto R. consistently records higher GDOP values at every epoch, reflecting greater dilution of precision. This is especially evident at Epochs 2 seconds to 4 seconds, where Veneto R. maintains a GDOP of 2.7, while HXGN ranges between 1.7 and 2.2. Even at Epoch 8 seconds, where both datasets approach their lowest values, Veneto R. still exceeds HXGN by 0.4 (2.2 vs. 1.8). These consistent disparities underscore HXGN’s superior geometric configuration and measurement stability, while Veneto R.’s higher values suggest less favorable satellite geometry or measurement conditions. Thus, while the trend is similar, the precision and reliability of the two systems differ significantly.

### **Distance difference**

#### **Overall trend**

The HXGN baselines (F12 and F32) exhibit a stable and gradually increasing trend (figure 46). For F12, the values begin at 0.00131 meter and rise steadily to 0.00749 meter, maintaining a consistent trajectory with minimal fluctuation. Similarly, F32 starts at 0.01883 meter, peaks at 0.02877 meter by epoch 4 seconds, and then stabilizes around 0.025–0.026 meter through the remaining epochs. This smooth progression reflects a high degree of temporal stability and measurement reliability in the HXGN system.

### **Comparison with HXGN measurements conducted using HXGN NRTK in March**

The trend analysis of distance differences between HXGN measurements taken in March and on the 2nd of April for baselines F12 and F32 reveals a pattern of remarkable consistency, particularly in the F12 baseline, and subtle variation in F32. For F12, the trend is identical across both datasets. At each epoch from 1 second to 9 seconds, the distance differences remain unchanged between March and April, starting at 0.001 meter at epoch 1 second, rising gradually to a peak of 0.011 meter at epoch 4 seconds, and then stabilizing around 0.007 meter through epochs 7 seconds to 9 seconds. This flat and repeatable trend indicates a high level of temporal stability and measurement repeatability in the HXGN system for this baseline. In contrast, the F32 baseline shows a nearly identical but slightly more dynamic trend. The values in April closely follow those in March, with differences only in the fourth or fifth decimal place. For example, at epoch 1 second, the distance

difference is 0.019 meter in March and 0.01883 meter in April; at epoch 4 seconds, it is 0.029 meter in March and 0.02877 meter in April. Despite these minute differences, the overall trend remains the same: a steady increase from epoch 1 second to 4 seconds, followed by a slight decline and stabilization through epochs 5 seconds to 9 seconds.

**Comparison with Veneto R. measurements**

The comparative analysis of the distance difference trends for HXGN F12, HXGN F32, Veneto R. F12, and Veneto R. F32 across nine epochs reveals distinct behavioral patterns between the two GNSS networks, both in terms of consistency and variability.

The main resemblance between the networks lies in their initial upward trends during epochs 1 second to 4 seconds, where all baselines show increasing distance differences, likely reflecting similar geometric or environmental conditions. Both F32 baselines peak around epoch 4 seconds, with HXGN F32 at 0.02877 meter and Veneto R. F32 at 0.02849 meter, indicating a shared response to satellite geometry or signal quality.

However, the main differences emerge from epoch 5 seconds onward. HXGN maintains a stable and positive trend, while Veneto R. begins to show sharp fluctuations and negative values, especially in F12. The divergence is most pronounced at epoch 7 seconds, where HXGN F12 remains at 0.00749 meter, but Veneto R. F12 drops to -0.02216 meter, and Veneto R. F32 to -0.00378 meter, contrasting sharply with HXGN F32’s 0.02666 meter.

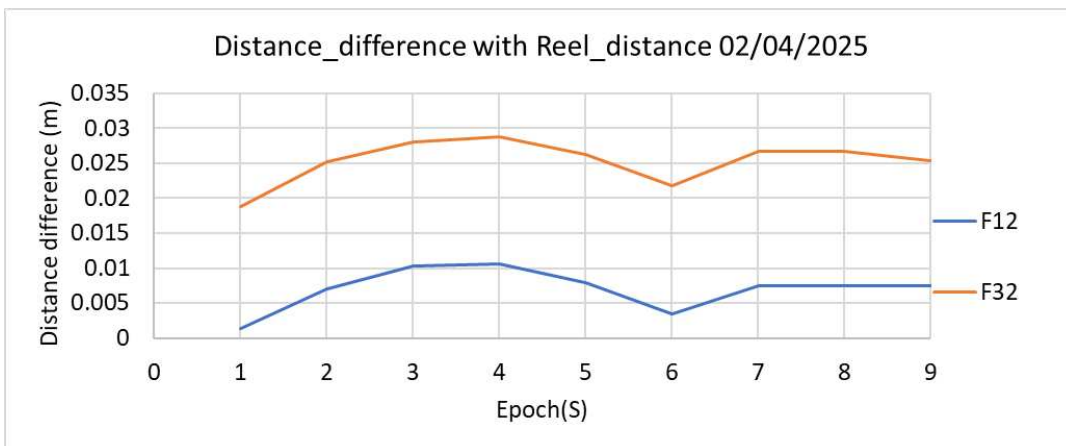


Figure 46: Distance difference for HXGN as per the data collected on 02/04/2025 from Epoch 1 second to 9 seconds

## Elevation difference

### Overall trend

At 1 second, the elevation difference begins at approximately +0.033 meter, indicating a positive deviation from the reference elevation (figure 47). Over the subsequent epochs, the elevation difference exhibits a steady downward trend, reaching a minimum of approximately  $-0.025$  m at epoch 7 seconds. This transition reflects a net vertical displacement of nearly 6 centimeters over the observed interval. Following this minimum, the elevation difference shows a slight upward correction, ending at a value closer to  $-0.015$  meter by epoch 9 seconds. This behavior may be attributed to transient satellite geometry changes, atmospheric effects, and quality of corrections received from HXGN, influencing the vertical positioning accuracy.

The overall pattern suggests a systematic drift in elevation estimation during the initial epochs, followed by partial stabilization. Such trends are critical to monitor in high-precision GNSS applications, particularly in contexts where vertical accuracy is essential (e.g., geodetic surveying, structural monitoring, or autonomous navigation). In this way, the acquisition of observations and corrections up to 9 seconds do not guarantee high accuracies.

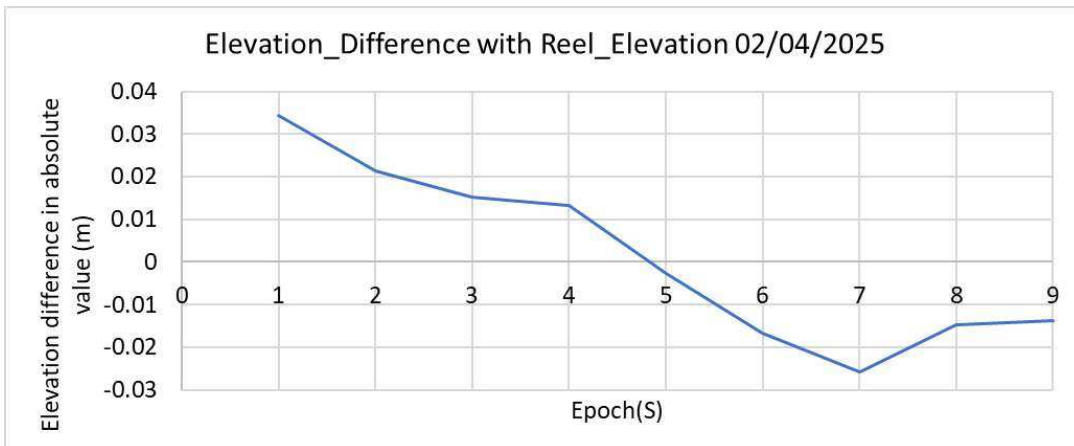


Figure 47: Elevation difference for HXGN as per the data collected on 2/4/2025 from Epoch 1s to 9s

### Comparison with measurements as per Veneto R.

Temporal Similarities are observed at several epochs where the distance differences between the two networks are minimal. For instance, at epoch 1 second, both HXGN and Veneto R. record nearly identical values (0.03430 meter vs. 0.03530 meter), resulting in a negligible difference of 0.001 meter. Similar convergence is also noted at epoch 9 seconds, where the difference is just 0.026

meter, and at epoch 5 seconds, with a difference of 0.013 meter. These points suggest that under certain conditions, both networks respond similarly to spatial and environmental factors.

However, distinct divergences emerge at other epochs. The most pronounced difference occurs at epoch 3, where Veneto R. records 0.05430 meter compared to HXGN's 0.01530 meter, yielding a maximum deviation of 0.03900 meter. This sharp contrast indicates a significant discrepancy in measurement behavior, possibly due to network-specific geometric configurations or correction models. Another notable divergence is seen at epoch 6 seconds, where Veneto R. shows 0.04630 meter while HXGN drops to  $-0.01670$  meter, resulting in a difference of 0.06300 meter—the largest observed in the dataset.

Overall, the Veneto R. maintains a consistently positive and expansive trend, while HXGN exhibits more oscillatory behavior, including several negative values that suggest contraction or reversal in positional measurements. These differences highlight the Veneto R.'s greater stability and uniformity, particularly in epochs with high deviation in HXGN data.

### **3.1.2.3. HXGN measurements carried out on 28<sup>th</sup> April 2025**

Measurements in points 1000 and 2000 were repeated on 28<sup>th</sup> April 2025 using corrections from HXGN and observations acquired from 1 second to 9 seconds. In this way, a comparison between data related to different days, but acquired with the same settings and using corrections from the same network, can be performed.

## **CQ**

### **Trend at the point 1000**

CQ 3D begins at approximately 0.009 meter (figure 48), fluctuates slightly, and returns to a similar value by epoch 9 seconds. This indicates consistent theoretical three-dimensional positioning precision with no significant degradation or improvement.

CQ 2D remains the most stable, starting and ending near 0.005 meter, with minimal variation. This reflects highly consistent theoretical horizontal positioning quality.

CQ 1D starts at around 0.007 meter, shows minor fluctuations, and ends close to its initial value, indicating stable theoretical vertical positioning performance.

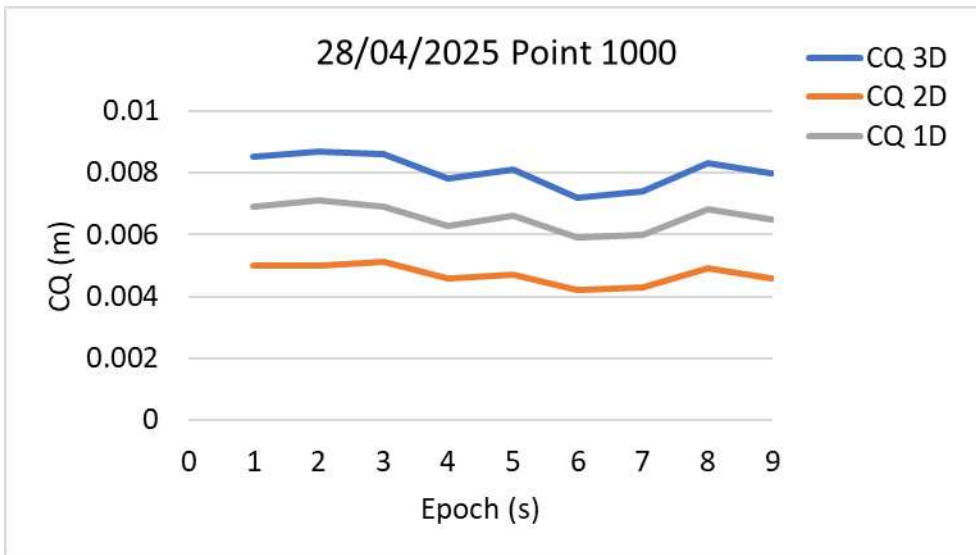


Figure 48: CQ values for HXGN as per the data collected on 28/04/2025 from Epoch 1 second to 9 seconds at point 1000

#### Comparison with March measurements at point 1000 using HXGN

The comparison of HXGN CQ measurements from March and April 28<sup>th</sup> across nine epochs reveals a shared trend structure with notable differences in magnitude, and specific epochs where values closely resemble each other. Both datasets follow a generally stable pattern in CQ 3D, CQ 2D, and CQ 1D values, with slight fluctuations across epochs. However, March consistently shows higher magnitudes: for instance, CQ 3D peaks at 0.0144 meter in Epoch 8 seconds, while April’s highest is only 0.0087 meter at Epoch 2 seconds. Similarly, CQ 1D values in March range from 0.0080 meter to 0.0121 meter, whereas April ranges from 0.0059 meter to 0.0075 meter. Despite these differences, Epochs 5 seconds and 6 seconds show similar trend shapes, with both datasets dipping in CQ 3D and CQ 1D values—March at 0.0097 meter and 0.0080 meter, April at 0.0081 meter and 0.0066 meter respectively—indicating a resemblance in behavior. Overall, while the temporal patterns align, March measurements reflect higher and more variable values, whereas April demonstrates greater consistency and lower magnitudes, suggesting improved precision or different measurement conditions.

#### Comparison with Veneto R. measurements at point 1000

The comparison of CQ measurements between HXGN and Veneto R. across nine epochs reveals a shared trend structure with distinct differences in magnitude and variability, as well as specific epochs where resemblances are observed. Both datasets follow a generally decreasing pattern in CQ 3D, CQ 2D, and CQ 1D values, indicating a common temporal behavior. Notably, Epochs 1 second

to 3 seconds show the closest resemblance in trend, where both HXGN and Veneto R. exhibit gradual declines: for instance, CQ 3D values in HXGN range from 0.0085 meter to 0.0086 meter, while Veneto R. ranges from 0.0246 to 0.0257—though the magnitudes differ, the shape of the trend seems to be identical. Similarly, CQ 2D and CQ 1D values in these epochs follow parallel trajectories, with HXGN values around 0.005 meter and 0.007 meter, and Veneto R. values around 0.0141 meter and 0.02 meter respectively. However, from Epoch 4 seconds onward, the differences become pronounced, especially at Epoch 4 seconds, where Veneto R. spikes dramatically (CQ 3D = 0.2404 meter, CQ 2D = 0.1201 meter, CQ 1D = 0.2082 meter), contrasting sharply with HXGN’s stable values (CQ 3D = 0.0078 meter, CQ 2D = 0.0046 meter, CQ 1D = 0.0063 meter). These anomalies persist through Epochs 5 seconds to 7 seconds, though both datasets resume a downward trend toward Epoch 9 seconds. Overall, while the trend shapes align in early epochs, HXGN maintains lower and more consistent magnitudes, whereas Veneto R. shows greater dispersion and episodic instability, especially in mid-epochs.

## **CQ**

### **Trend at the point 2000**

over nine epochs, CQ values demonstrate a general downward trend followed by partial recovery, indicating changes in measurement precision over time (figure 49). CQ 3D values begin at 0.0085 meter and peak slightly at 0.0087 meter in Epoch 2 seconds, then decline to a minimum of 0.0072 meter by Epoch 6 seconds before rising again to 0.0083 meter in Epoch 8 seconds. CQ 2D values show a similar pattern, starting at 0.005 meter, dipping to 0.0042 meter in Epoch 6 seconds, and recovering slightly to 0.0049 meter in Epoch 8 seconds. CQ 1D values follow a comparable trajectory, peaking at 0.0071 meter in Epoch 2 seconds, dropping to 0.0059 meter in Epoch 6 seconds, and then increasing to 0.0068 meter in Epoch 8 seconds. This trend suggests an initial phase of stable measurements, followed by a period of reduced precision—possibly due to environmental or instrumental factors—and a subsequent improvement, reflecting dynamic conditions affecting spatial data quality.

Both Point 1000 and Point 2000 demonstrate highly stable and nearly identical CQ profiles across all three dimensions. The absence of significant deviations or trends suggests that the GNSS system performed consistently across spatial locations during the observed interval. This uniformity supports the theoretical reliability of the system under similar environmental and satellite geometry conditions.

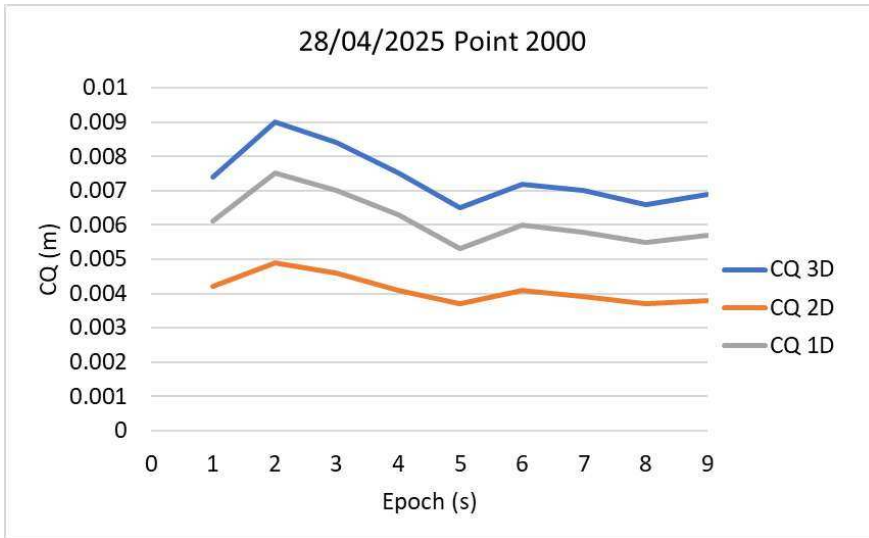


Figure 49: CQ values for HXGN as per the data collected on 28/04/2025 from Epoch 1 second to 9 seconds at point 2000

### Comparison with March measurements at the point 2000

Both datasets exhibit stable and gradually declining patterns in CQ 3D, CQ 2D, and CQ 1D values, indicating similar temporal behavior. However, 2<sup>nd</sup> April measurements consistently show higher magnitudes across all dimensions: for example, CQ 3D values in April range from 0.0095 meter to 0.0111 meter, while March ranges from 0.0065 meter to 0.0090 meter. The same applies to CQ 2D and CQ 1D, where April values are approximately 0.001 meter to 0.003 meter higher than March. Despite this, Epochs 1 second and 2 seconds show similar trend shapes, with both months peaking in CQ 3D and CQ 1D—March at 0.009 meter and 0.0075 meter, April at 0.0106 meter and 0.009 meter respectively—indicating a resemblance in behavior. Overall, while the trend alignment is strong, April measurements reflect higher and more consistent values, suggesting improved precision or different measurement conditions compared to March.

### Comparison with Veneto R. measurements

The comparison of CQ measurements between HXGN and Veneto R. across nine epochs reveals a shared downward trend in CQ 3D, CQ 2D, and CQ 1D values, but with substantial differences in magnitude and variability, and specific epochs where the trend shapes resemble each other. Both datasets show a general decline over time, indicating a common temporal behavior in measurement precision. For example, from Epochs 1 second to 3 seconds, both HXGN and Veneto R. exhibit a gradual decrease in all three dimensions—CQ 3D drops from 0.0074 meter to 0.0084 meter for HXGN and from 0.0246 meter to 0.0257 meter for Veneto R., while CQ 1D follows a similar pattern,

suggesting resemblance in trend despite the magnitude gap. However, the differences become pronounced from Epoch 4 seconds onward, where Veneto R. experiences extreme spikes, especially at Epoch 4 seconds (CQ 3D = 0.2404 meter, CQ 2D = 0.1201 meter, CQ 1D = 0.2082 meter), contrasting sharply with HXGN's stable values (CQ 3D = 0.0075 meter, CQ 2D = 0.0041 meter, CQ 1D = 0.0063 meter). Even in later epochs, Veneto R.'s values remain significantly higher, such as CQ 3D = 0.0162 meter at Epoch 9 seconds versus HXGN's 0.0069 meter. These observations highlight HXGN's superior consistency and precision, while Veneto R.'s measurements reflect greater dispersion and episodic instability, despite some early alignment in trend shape.

## **GDOP**

### **Trend at point 1000**

At Point 1000, the GDOP starts at approximately 1.3, rises sharply to 1.7 at epoch 3 seconds, and then drops back to near its initial value by epoch 5 seconds (figure 50). From epoch 5 seconds to 9 seconds, the GDOP remains relatively stable with minor fluctuations. This trend indicates a brief but pronounced deterioration in satellite geometry, followed by a rapid correction and stabilization. The sharper peak compared to Point 2000 suggests that Point 1000 experienced more dynamic satellite visibility or geometry changes during the early epochs.

### **Comparison with March data at point 1000**

The comparison of GDOP values from HXGN measurements taken in March and on the 28th of April across nine epochs reveals a similar overall trend with distinct differences in magnitude and consistency, and specific epochs where values closely resemble each other. Both datasets show relatively stable GDOP values, fluctuating mildly around a central range, indicating consistent geometric precision over time. However, March values tend to be slightly higher, ranging from 1.4 to 1.7, while April values are more tightly clustered between 1.4 and 1.7, with a noticeable lower baseline. Epochs 6 seconds to 9 seconds show the closest resemblance, where both March and April GDOP values converge around 1.4 to 1.5, suggesting similar satellite geometry during those periods. In contrast, Epochs 1 second to 3 seconds highlight the differences, with March peaking at 1.7 and April gradually rising from 1.4 to 1.7. Overall, while both series follow a comparable trend, April 28<sup>th</sup> measurements reflect slightly improved and more consistent geometric precision compared to March.

### Comparison with Veneto R. measurements at point 1000

The comparison of GDOP between Veneto R. and HXGN across nine epochs reveals a consistent difference in magnitude and a partially aligned trend, with specific epochs showing closer resemblance. Veneto R. GDOP values remain significantly higher throughout, ranging from 2.2 to 2.8. In contrast, HXGN values are consistently lower, ranging from 1.4 to 1.7, reflecting better geometric precision. Both datasets show a relatively stable trend, but Epoch 8s stands out as the point of closest resemblance, where Veneto R. records 2.2 and HXGN 1.4—still different, but both at their lower bounds. The largest gap appears at Epochs 1 second to 3 seconds, where Veneto R. maintains values of 2.7–2.8, while HXGN ranges from 1.4 to 1.7. Overall, while the trend shapes are similar, the magnitude gap is persistent, underscoring HXGN’s superior satellite geometry configuration compared to Veneto R.

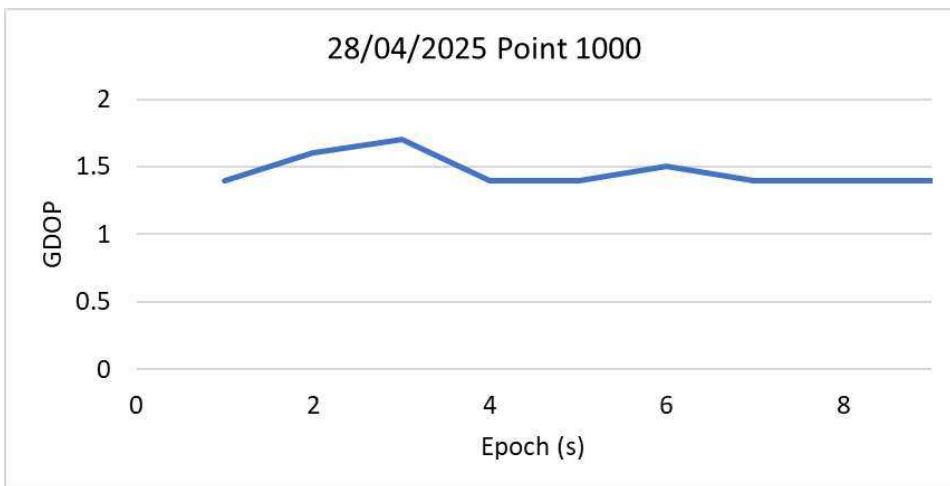


Figure 50: GDOP values for HXGN as per the data collected on 28/04/2025 from Epoch 1 second to 9 seconds at point 1000

### GDOP

#### Trend at point 2000

The GDOP values at Point 2000 (figure 51) begin at approximately 1.4, increase slightly to a peak of 1.6 at epoch 3 seconds, and then gradually decrease back to 1.4 by epoch 9 seconds. This pattern reflects a mild and symmetric fluctuation, suggesting a temporary degradation in satellite geometry followed by a recovery. The overall variation is limited, indicating relatively stable and consistent positioning conditions throughout the interval.

Both points exhibit a peak in GDOP around epoch 3 seconds, though the magnitude and recovery behavior differ. Point 2000 shows a gentler and more symmetrical variation, while Point 1000

experiences a steeper and more transient spike. These differences may be attributed to local environmental factors, satellite constellation geometry, or receiver-specific conditions.

### Comparison with March measurements at point 2000

Both datasets exhibit a relatively stable pattern, with GDOP values fluctuating mildly, indicating consistent geometric precision. However, March values are generally higher, ranging from 1.4 to 1.7, while April values are lower and more consistent, ranging from 1.3 to 1.6. The closest resemblance occurs at Epoch 4 seconds, where both months record a GDOP of 1.6, and at Epoch 3 seconds, where March has 1.5 and April 1.6—showing near alignment. In contrast, Epochs 1 second and 6 seconds to 9 seconds highlight the differences, with March maintaining values around 1.5, while April consistently records 1.3. Overall, while the trend shapes align, April 28 measurements reflect slightly improved and more stable geometric precision compared to March.

### Comparison with Veneto R. measurements at point 2000

Both datasets exhibit fluctuations, but while HXGN maintains a stable and low GDOP range between 1.3 and 1.6, Veneto R. shows extreme variability, ranging from 1.7 to a peak of 12.2 at Epoch 6 seconds, indicating severe geometric dilution of precision. The closest resemblance occurs at Epochs 1s and 3 seconds, where Veneto R. records 1.7 and HXGN 1.3–1.6, showing a similar trend direction despite the magnitude gap. In contrast, Epochs 4 seconds to 7 seconds highlight the most significant divergence, with Veneto R. values spiking to 3.6, 2.6, 12.2, and 3.7 respectively, while HXGN remains steady at 1.3–1.6. These observations underscore HXGN’s superior and consistent satellite geometry, while Veneto R.’s data reflects episodic instability and reduced precision, especially in mid-epochs.

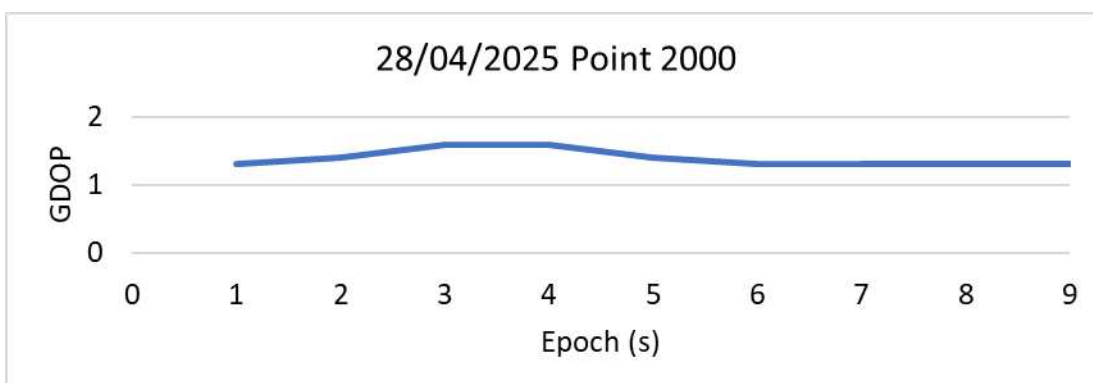


Figure 51: GDOP values for HXGN as per the data collected on 28/04/2025 from Epoch 1 second to 9 seconds at point 2000

## **Distance difference**

### **General trend**

The F12 series begins at approximately 0.005 meter (figure 52), decreases to a minimum of around -0.002 meter at epoch 3 seconds, and then exhibits a steady upward trend, peaking at approximately 0.025 meter by epoch 8 seconds. A slight decline is observed at epoch 9 seconds. This pattern indicates an initial overestimation correction followed by a gradual divergence from the reference distance, suggesting a progressive accumulation of error or drift in the measurement system.

The F32 series starts higher, at approximately 0.025 meter, and follows a similar but more pronounced trend. After a slight initial decrease, it increases steadily to a peak of ~0.04 meter at epoch 7 seconds, followed by a sharp drop by epoch 9 seconds. This behavior suggests a larger and more variable deviation from the reference distance, with a late-stage correction or instability.

While both series exhibit a general increasing trend in distance difference, F32 shows greater magnitude and volatility compared to F12. The divergence between the two polylines becomes more pronounced after epoch 3 seconds due to cartographic deformations.

### **Comparison with March measurements**

Both F12 and F32 series show fluctuating patterns over time, but March values tend to be more stable and consistently positive, while April values exhibit greater variability, including a negative F12 value at Epoch 3 seconds (-0.0011 meter), contrasting sharply with March's 0.0103 meter. F32 values in April also show a steeper rise toward Epochs 7 seconds and 8 seconds, peaking at 0.0401 meter and 0.0391 meter respectively, compared to March's maximum of 0.0288 meter at Epoch 4 seconds. However, Epochs 1 second and 2 seconds show similar trend shapes, with both months presenting moderate F12 and F32 values—e.g., March F12 = 0.0013 and 0.0071, April F12 = 0.0057 meter and 0.0029 meter. Overall, while the trend directions align, April measurements reflect greater dispersion and dynamic range, especially in later epochs, whereas March values are more consistent and centered.

### **Comparison with Veneto R. measurements**

Both datasets exhibit fluctuating patterns, but Veneto R.'s F12 values include negative entries from Epochs 6 seconds to 9 seconds, reaching as low as -0.0222 meter at Epoch 7 seconds, while HXGN's

F12 values remain consistently positive, peaking at 0.0218 meter in the same epoch. Similarly, Veneto R.'s F32 values show a sharp drop to negative at Epoch 7 seconds (-0.0038 meter), whereas HXGN's F32 values steadily increase, peaking at 0.0401 meter at Epoch 7 seconds. The closest resemblance occurs at Epochs 2 seconds and 3 seconds, where both F12 and F32 values from Veneto R. and HXGN are relatively low and close in magnitude—e.g., Veneto R. F12 = 0.0016 meter, HXGN F12 = 0.0029 meter; Veneto R. F32 = 0.0189 meter, HXGN F32 = 0.0216 meter. Overall, while both systems follow a similar oscillating trend, HXGN demonstrates greater stability and consistently positive values, whereas Veneto R. reflects higher variability and occasional instability, especially in later epochs.

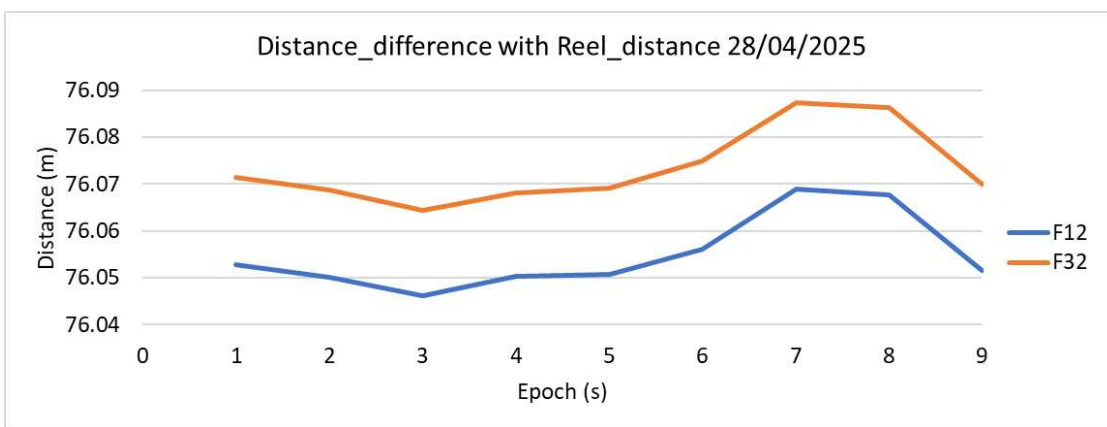


Figure 52: Distance difference values for HXGN as per the data collected on 28/04/2025 from Epoch 1 second to 9 seconds

### Difference in elevation

#### Overall trend

The difference in elevation graph (figure 53) reveals a non-linear and fluctuating trend:

**Initial Peaks:** Elevation differences are relatively high at epochs 1 second and 2 seconds, reaching values near 0.025 meter, indicating early deviations from the reference elevation.

**Mid-Interval Drop:** A notable decline occurs at epoch 5 seconds, where the elevation difference reaches a local minimum, suggesting a temporary alignment or correction in vertical positioning.

**Late Fluctuation:** The elevation difference rises again toward epoch 8 seconds, followed by a slight decline at epoch 9 seconds, indicating continued variability in vertical accuracy.

Overall, the graph demonstrates short-term instability in elevation measurements, with alternating phases of overestimation and correction. These fluctuations may be attributed to satellite geometry

changes and the quality of corrections received by the HXGN. The magnitude of variation, though limited to a few centimeters, is relevant for applications requiring high vertical precision. However, for standard applications, the level of accuracy was very good, since the maximum error was about 2 centimeters.

### **Comparison with March measurements**

An analysis of elevation differences recorded in March and on the 28th of April across nine epochs reveals a nuanced interplay between stability and change in terrain behavior. While both months exhibit alternating positive and negative values—suggesting localized fluctuations—certain epochs show remarkable consistency, such as Epoch 3 seconds (0.0153 meter in March vs. 0.0133 meter in April) and Epoch 5 seconds (−0.0027 meter vs. −0.0017 meter). However, April generally displays higher elevation differences, with a mean of 0.0124 meter compared to 0.0012 meter in March, pointing to intensified terrain dynamics likely influenced by seasonal factors. Notably, Epochs 6 seconds through 8 seconds demonstrate significant shifts, with values transitioning from negative in March (e.g., −0.0167 meter at Epoch 6 seconds) to positive in April (e.g., 0.0013 meter).

### **Comparison with Veneto R. measurements**

Examining the distance difference variations between Veneto R. and the 28th of April across nine epochs reveals a distinct shift in spatial dynamics. Veneto R.'s measurements, averaging 0.0267 meter, consistently surpass those of April, which average 0.0124 meter, indicating a general contraction in distance differences as the season progressed. Epoch-specific comparisons underscore this trend: for instance, Epoch 3 seconds transitions from a substantial 0.0543 meter in March to a modest 0.0133 meter in April, while Epoch 6 seconds drops from 0.0463 meter to 0.0013 meter, reflecting a pronounced reduction. Conversely, a few epochs such as Epoch 7 seconds show an increase, rising from 0.0013 meter to 0.0133 meter, suggesting localized expansion. The overall mean difference of −0.0143 meter supports the notion of a net decrease, with the largest individual shift being 0.0120 meter and the smallest −0.0450 meter. These findings point to a heterogeneous landscape response, where some regions contract while others expand, potentially influenced by environmental or anthropogenic factors.

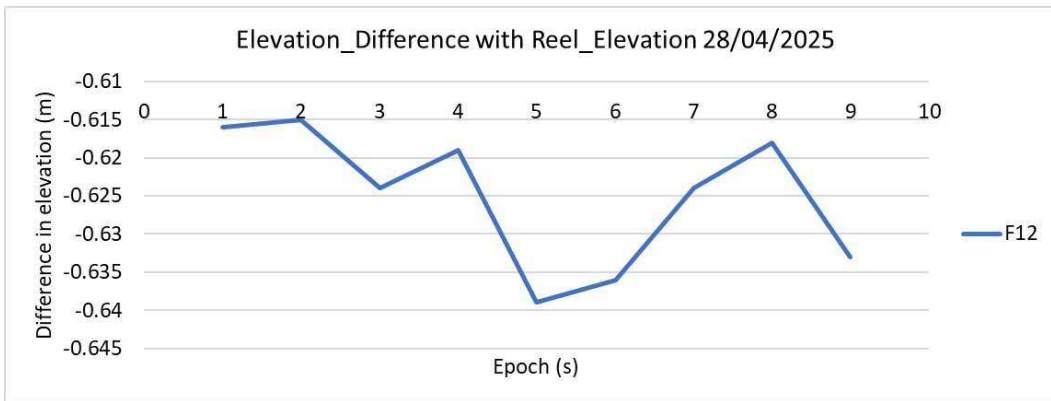


Figure 53: Elevation difference values for HXGN as per the data collected on 28/04/2025 from Epoch 1 second to 9 seconds

### 3.2. Analysis of the performance between the different NRTK and ranking

#### 3.2.1. CQ1D performance and ranking

##### Point 1000

The datasets evaluated from boxplot (figure 54), show that the HXGN dataset from 28th April ranks 1st overall, offering the best combination of precision and consistency. It has a low median value (0.0066), indicating high precision, and the smallest IQR (0.0006), reflecting excellent consistency. The interquartile range is tightly bounded (Q1 = 0.0063, Q3 = 0.0069), and the whiskers (lower = 0.0054, upper = 0.0078) confirm a compact and symmetric distribution. The absence of outliers and a favorable score (0.00438) reinforce its reliability. The HXGN dataset from 19th March, ranked 2nd, shows good precision (median = 0.0055) and moderate consistency (IQR = 0.0038), with a slightly wider spread (Q1 = 0.0033, Q3 = 0.0072) and whiskers extending from -0.00235 to 0.01285. The absence of outliers supports its stability, although the negative lower whisker suggests some skewness. The HXGN dataset from 2nd April, ranked 3rd, presents lower precision (highest median = 0.0108 among HXGN datasets) and moderate consistency (IQR = 0.0021), with a broader interquartile range (Q1 = 0.0098, Q3 = 0.0119) and whiskers from 0.00665 to 0.01505. Its score (0.00796) reflects this trade-off between central tendency and dispersion. Finally, the Veneto R. dataset from 9th April ranks last (4th) due to its low precision (median = 0.0107), poor consistency (widest IQR = 0.0101), and the presence of one outlier. The distribution is highly dispersed (Q1 = 0.0039, Q3 = 0.0141), with extreme whiskers (lower = -0.0114, upper = 0.0293), indicating significant variability and reduced reliability.

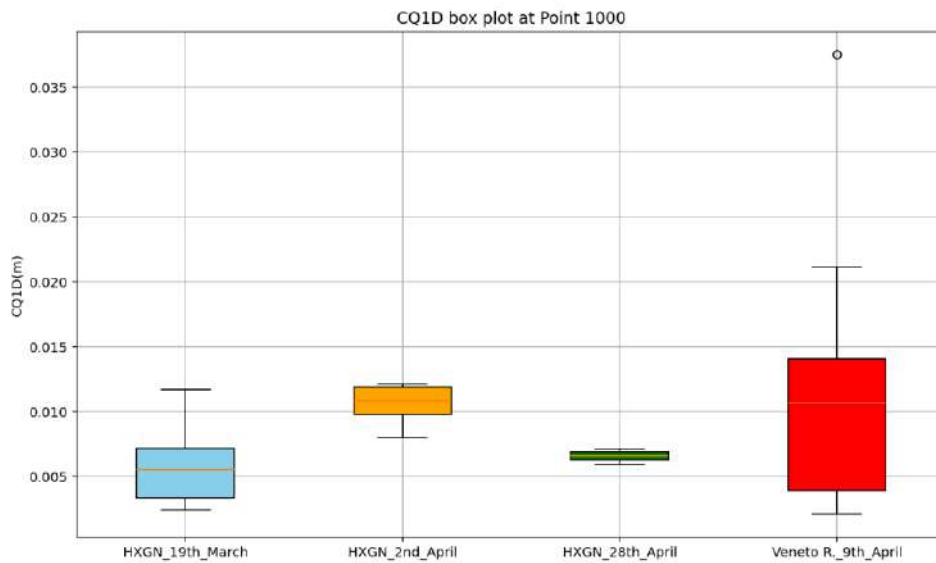


Figure 54: Box plot analysis of CQ1D measurements at point 1000

#### Point 2000

Among the datasets evaluated from box plot (figure 55) the HXGN dataset from 28th April ranks 1st overall, offering the best combination of precision and consistency. It has a low median value (0.006) and a very small IQR (0.0006), indicating both high precision and excellent consistency. The interquartile range is tightly bounded (Q1 = 0.0057, Q3 = 0.0063), and the whiskers (lower = 0.0048, upper = 0.0072) confirm a compact distribution. Despite the presence of one outlier, its overall score (0.10402) remains the most favorable. The HXGN dataset from 24th March, ranked 2nd, shows excellent precision (lowest median = 0.0039) and good consistency (IQR = 0.003), with a stable interquartile range (Q1 = 0.00265, Q3 = 0.00565) and whiskers from -0.00185 to 0.01015. The absence of outliers supports its reliability, although the slightly wider spread compared to 28th April affects its score (0.00449). The HXGN dataset from 2nd April, ranked 3rd, presents lower precision (median = 0.009) but excellent consistency (IQR = 0.0005), with a narrow interquartile range (Q1 = 0.0088, Q3 = 0.0093) and whiskers from 0.00805 to 0.01005. Its score (0.00576) reflects this balance, though the higher median reduces its overall ranking. Finally, the Veneto R. dataset from 30th April ranks last (4th) due to its low precision (highest median = 0.01095), poor consistency (widest IQR = 0.012975), and the presence of three outliers. The distribution is highly dispersed (Q1 = 0.00725, Q3 = 0.012975), with extreme whiskers (lower = -0.0122, upper = 0.0396875), indicating significant variability and reduced reliability.

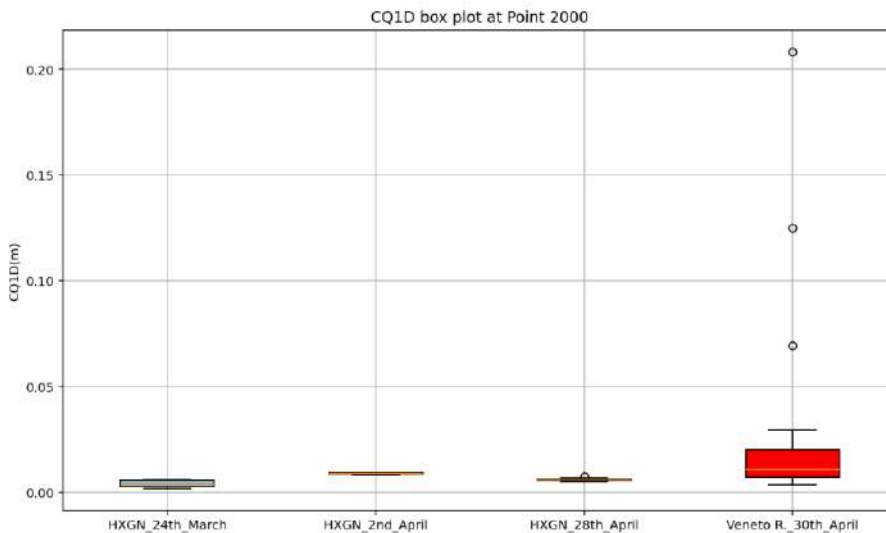


Figure 55: Box plot analysis of CQ1D measurements at point 2000

### 3.2.2. CQ2D performance and ranking

#### Point 1000

Among the datasets evaluated from boxplot (figure 56), the HXGN dataset from 19th March ranks 1st overall, offering the best balance of precision and consistency. It has the lowest median value (0.0034), indicating high precision, and a small IQR (0.00265), reflecting good consistency. The interquartile range (Q1 = 0.00185, Q3 = 0.0045) is compact, and the whiskers (lower = -0.002125, upper = 0.008475) show a reasonably symmetric spread. The absence of outliers and a favorable score (0.00385) confirm its reliability. The HXGN dataset from 2nd April, ranked 2nd, presents moderate precision (median = 0.0068) and good consistency (IQR = 0.0016), with a narrow interquartile range (Q1 = 0.0057, Q3 = 0.0073) and whiskers from 0.0033 to 0.0097. Its score (0.00514) reflects a stable distribution, although slightly less precise than 19th March. The HXGN dataset from 28th April, ranked 3rd, shows acceptable precision (median = 0.0041) and excellent consistency (lowest IQR = 0.0004), but the presence of one outlier and a slightly skewed distribution (whiskers from 0.0032 to 0.0048) contributes to a higher score (0.10272), indicating reduced reliability. Finally, the Veneto R. dataset from 9th April ranks last (4th) due to its low precision (median = 0.00675), poor consistency (widest IQR = 0.006175), and the presence of one outlier. The distribution is highly dispersed (Q1 = 0.00235, Q3 = 0.008525), with extreme whiskers (lower = -0.0069125, upper = 0.0177875), suggesting significant variability and reduced robustness.

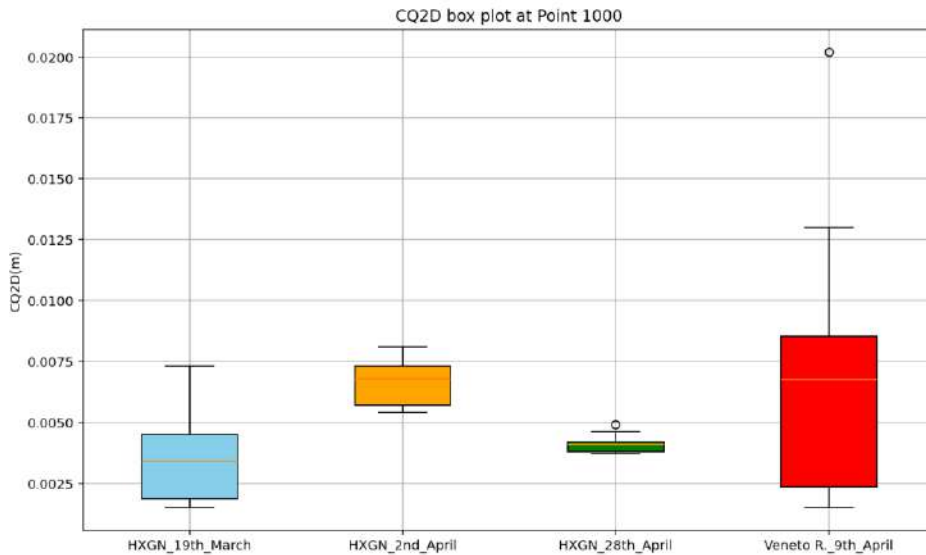


Figure 56: Box plot analysis of CQ2D measurements at point 1000

### Point 2000

Among the datasets evaluated from box plot (figure 57), the HXGN dataset from 24th March ranks 1st overall. It has the lowest median value (0.0024), indicating excellent precision, and a small IQR (0.00165), reflecting strong consistency. The interquartile range (Q1 = 0.00175, Q3 = 0.0034) is compact, and the whiskers (lower = -0.000725, upper = 0.005875) show a symmetric and stable distribution. The absence of outliers and a favorable score (0.00263) confirm its robustness. The HXGN dataset from 2nd April, ranked 2nd, presents moderate precision (median = 0.0055) and excellent consistency (IQR = 0.0006), with a narrow interquartile range (Q1 = 0.005, Q3 = 0.0056) and whiskers from 0.0041 to 0.0065. Its score (0.00368) reflects a stable distribution, although slightly less precise than 24th March. The HXGN dataset from 28th April, ranked 3rd, shows acceptable precision (median = 0.0041) and best consistency (lowest IQR = 0.0004), but the presence of one outlier and a slightly skewed distribution (whiskers from 0.0032 to 0.0048) contributes to a higher score (0.10272), indicating reduced reliability. Finally, the Veneto R. dataset from 30th April ranks last (4th) due to its low precision (highest median = 0.0076), poor consistency (widest IQR = 0.010475), and the presence of two outliers. The distribution is highly dispersed (Q1 = 0.003625, Q3 = 0.0141), with extreme whiskers (lower = -0.0120875, upper = 0.0298125), suggesting significant variability and reduced robustness.

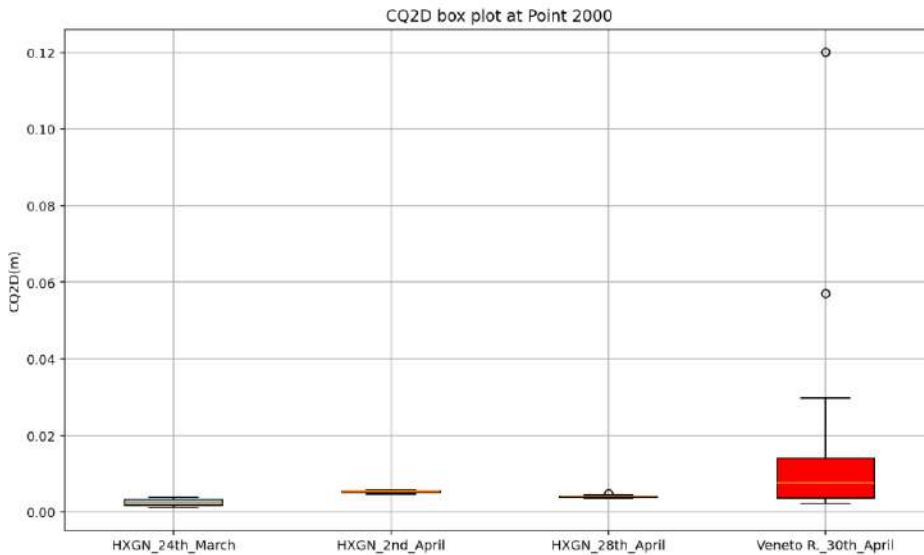


Figure 57: Box plot analysis of CQ2D measurements at point 2000

### 3.2.3. CQ3D performance and ranking

#### Point 1000

Among the datasets evaluated from box plot (figure 58), the HXGN dataset from 28th April ranks 1st overall, offering the best balance of precision and consistency. It has the lowest median value (0.0081), indicating high precision, and the smallest IQR (0.0007), reflecting excellent consistency. The interquartile range is tightly bounded (Q1 = 0.0078, Q3 = 0.0085), and the whiskers (lower = 0.0067, upper = 0.0096) confirm a compact and symmetric distribution. Despite the presence of one outlier, its overall score (0.00536) remains the most favorable. The HXGN dataset from 19th March, ranked 2nd, shows moderate precision (median = 0.0065) and acceptable consistency (IQR = 0.0045), with a slightly wider spread (Q1 = 0.0039, Q3 = 0.0084) and whiskers extending from -0.003 to 0.0152. The absence of outliers supports its stability, although the negative lower whisker suggests some skewness in the distribution. The HXGN dataset from 2nd April, ranked 3rd, presents lower precision (highest median = 0.013 among HXGN datasets) and moderate consistency (IQR = 0.0024), with a broader interquartile range (Q1 = 0.0116, Q3 = 0.014) and whiskers from 0.008 to 0.0176. Its score (0.00944) reflects this trade-off between central tendency and dispersion. Finally, the Veneto R. dataset from 9th April ranks last (4th) due to its low precision (median = 0.0126), poor consistency (widest IQR = 0.0122), and the presence of one outlier. The distribution is highly dispersed (Q1 = 0.0046, Q3 = 0.0167), with extreme whiskers (lower = -0.0137, upper = 0.035), indicating significant variability and reduced reliability.

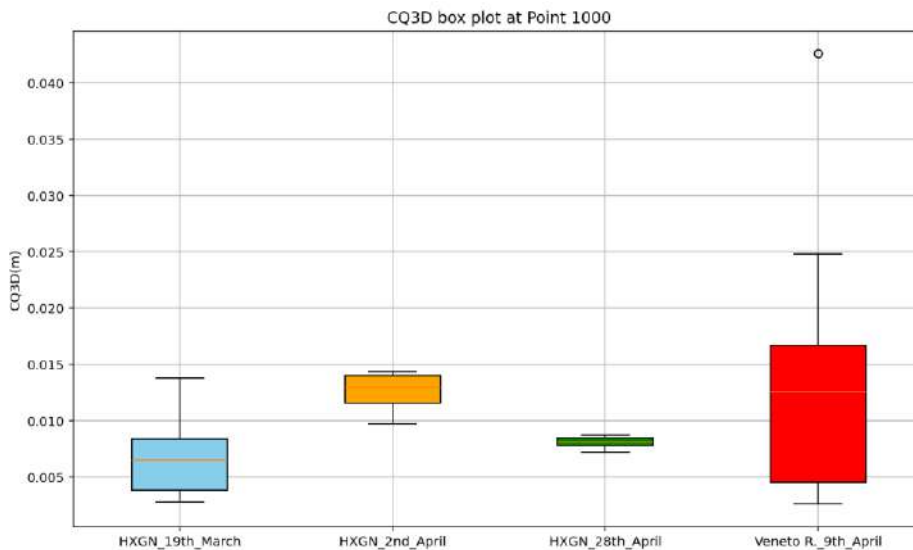


Figure 58: Box plot analysis of CQ3D measurements at point 1000

### Point 2000

The dataset deriving from box plot (figure 59) shows that HXGN 24th March ranks 1st overall, demonstrating the best precision (lowest median = 0.0045) and strong consistency (IQR = 0.00345). The interquartile range spans from Q1 = 0.0032 to Q3 = 0.0067, indicating a compact distribution. The whiskers (lower = -0.002, upper = 0.0118) are reasonably symmetric, and the absence of outliers confirms the robustness of the data. The HXGN dataset from 2nd April, ranked 2nd, shows moderate precision (median = 0.0106) but excellent consistency (IQR = 0.0006), with a tightly packed interquartile range (Q1 = 0.0102, Q3 = 0.0108) and symmetric whiskers (lower = 0.0093, upper = 0.0117). Its score (0.0068) reflects this balance, although the slightly higher median reduces its reliability compared to 24th March. The HXGN dataset from 28th April, ranked 3rd, offers good precision (median = 0.0072) and best consistency (lowest IQR = 0.0005), but the presence of one outlier and a slightly skewed distribution (lower whisker = 0.006, upper = 0.0084) contributes to a higher score (0.10474), indicating less stability. Finally, the Veneto R. dataset from 30th April ranks last (4th) due to its lowest precision (highest median = 0.0134), poorest consistency (widest IQR = 0.0168), and the presence of three outliers. The distribution is highly dispersed (Q1 = 0.0081, Q3 = 0.0249), with extreme whiskers (lower = -0.0171, upper = 0.05), suggesting significant variability and reduced reliability.

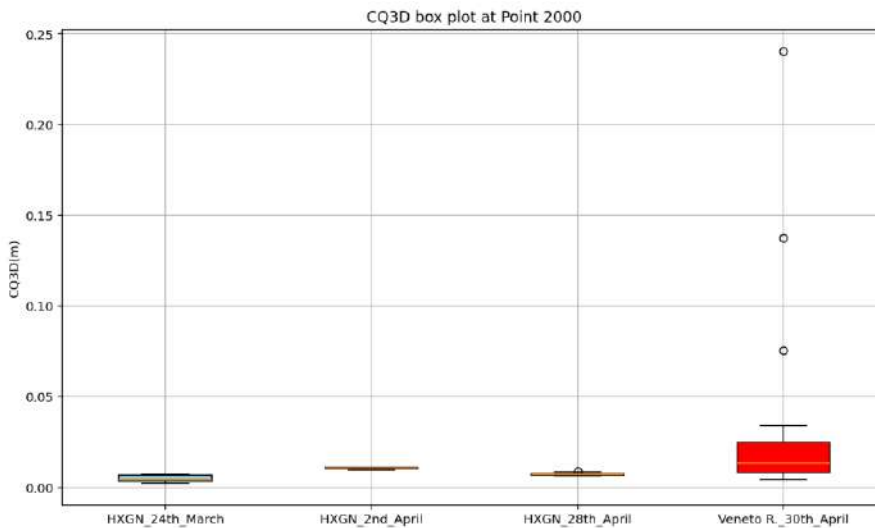


Figure 59: Box plot of CQ3D at point 2000

### 3.2.4. Distance difference performance and ranking

#### F32

When analyzing datasets evaluated from box plot (figure 60), the Veneto R. ones from 9th April ranks 1<sup>st</sup> in the list. Its median value (0.02438) is moderate, and its IQR (0.0109965) reflects acceptable consistency. The interquartile range (Q1 = 0.018493, Q3 = 0.0294895) is reasonably compact, and the whiskers (lower = 0.001998, upper = 0.04598) show a broad but symmetric distribution. Despite the presence of one outlier, its score (0.1222) is the most favorable among the four datasets. The HXGN dataset from 2nd April, ranked 2nd, presents the highest precision (median = 0.0262) and best consistency (lowest IQR = 0.0015), with a tightly bounded interquartile range (Q1 = 0.0252, Q3 = 0.0267) and whiskers from 0.02297 to 0.02888. However, the presence of two outliers and a slightly higher score (0.2167) reduced its overall reliability. The HXGN dataset from 19th March, ranked 3rd, shows good precision (lowest median = 0.01114) but poorest consistency (widest IQR = 0.01524), with a widespread (Q1 = -0.002, Q3 = 0.0133) and whiskers from -0.0248 to 0.0361. The presence of two outliers and a high score (0.21625) indicate significant variability. Finally, the HXGN dataset from 28th April, ranked last (4th), presents moderate precision (median = 0.02267) and low consistency (IQR = 0.00605), with a distribution ranging from Q1 = 0.02156 to Q3 = 0.02761 and whiskers from 0.01249 to 0.03668. The presence of two outliers and the highest score (0.21822) reflects reduced robustness.

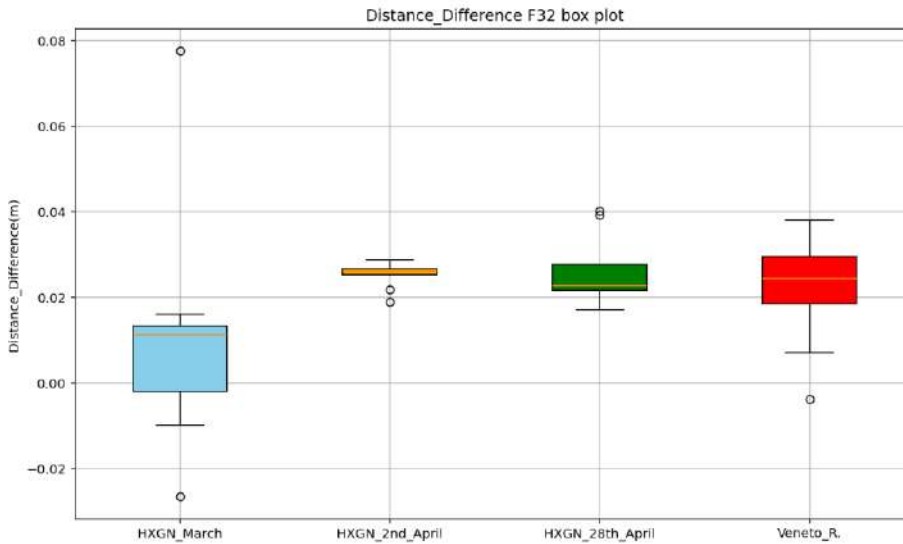


Figure 60: Box plot of distance difference in F32

The comparative analysis between the Veneto R and HXGN average datasets (figure 61) reveals distinct statistical profiles. Veneto R. exhibits a higher median value (0.0244 vs. 0.0141), suggesting generally stronger performance or intensity in its measured variable. However, HXGN shows greater variability, with a wider IQR (0.016 vs. 0.011) and more extreme whiskers (upper: 0.047 vs. 0.04599; lower: -0.0159 vs. 0.002), indicating a broader spread and presence of lower values. HXGN also has more outliers (2 vs. 1), which may reflect anomalies or exceptional cases. Despite these fluctuations, HXGN achieves a higher score (0.22 vs. 0.1222), yet ranks 2nd globally, behind Veneto R., which holds 1st place, due to its more consistent and concentrated data distribution.

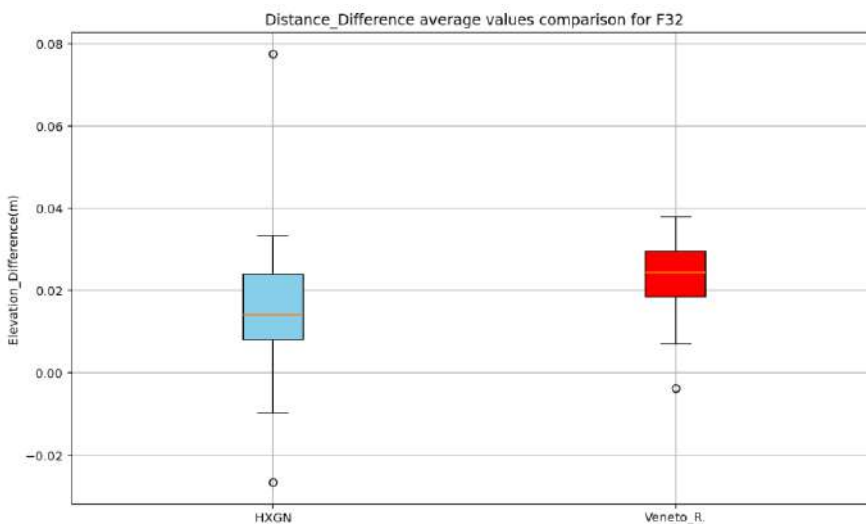


Figure 61: Box plot of distance difference F32 for Veneto R. and HXGN average values

## F12

The Veneto R. dataset from 9th April ranks 1st overall, offering a strong balance between precision and consistency. Its median value (0.006091) is moderate, and its IQR (0.011059) reflects acceptable consistency (figure 62). The interquartile range (Q1 = 0.00068, Q3 = 0.011739) is reasonably compact, and the whiskers (lower = -0.01591, upper = 0.028323) show a broad but symmetric distribution. Despite the presence of one outlier, its score (0.11142) is the most favourable among the four datasets. The HXGN dataset from 28th April, ranked 2nd, presents good precision (median = 0.00436) and moderate consistency (IQR = 0.00583), with a spread from Q1 = 0.00298 to Q3 = 0.00881 and whiskers from -0.005767 to 0.01756. However, the presence of two outliers and a higher score (0.207002) slightly reduce its reliability. The HXGN dataset from 19th March, ranked 3rd, shows low precision (negative median = -0.00698) and poor consistency (widest IQR = 0.01564), with a wide interquartile range (Q1 = -0.02053, Q3 = -0.00489) and whiskers from -0.043993 to 0.01857. The presence of two outliers and a high score (0.2112) indicate significant variability. Finally, the HXGN dataset from 2nd April, ranked last (4th), presents moderate precision (median = 0.00749) and excellent consistency (lowest IQR = 0.00086), with a tightly bounded interquartile range (Q1 = 0.0071, Q3 = 0.00795) and whiskers from 0.00581 to 0.00924. However, the presence of four outliers and the highest score (0.4051) reflect reduced robustness.

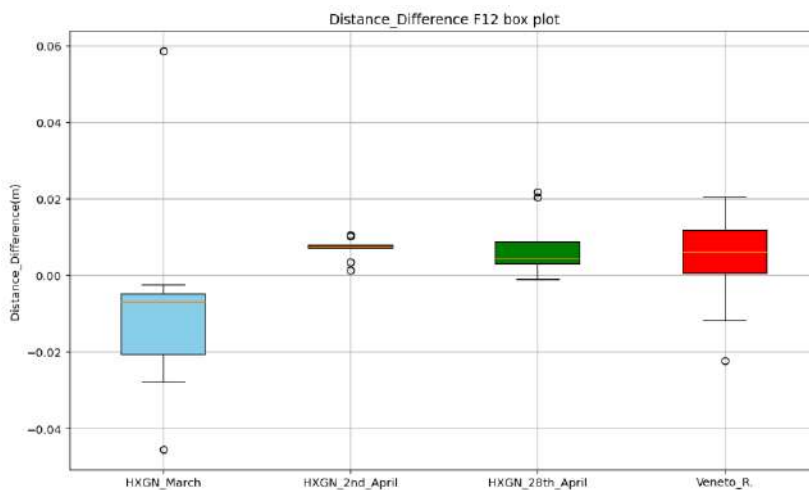


Figure 62: Box plot of distance difference F12

The comparison between Veneto R. and HXGN average values dataset highlights notable differences in central tendency and distribution. Veneto R. has a positive median (0.006091) (figure 63), indicating a generally upward trend, while HXGN shows a negative median (-0.0038), suggesting a slight downward bias. HXGN also displays greater variability, with a wider IQR (0.0166 vs. 0.011059) and more extreme whiskers (upper: 0.0306 vs. 0.028323; lower: -0.0358 vs. -0.01591), reflecting a

broader and more dispersed data range. It also has more outliers (2 vs. 1), which may indicate irregularities or exceptional values. Despite its volatility, HXGN March achieves a higher score (0.2126 vs. 0.11142), yet ranks 2nd globally, behind Veneto R., which maintains 1st place, likely due to its more stable and consistently positive performance.

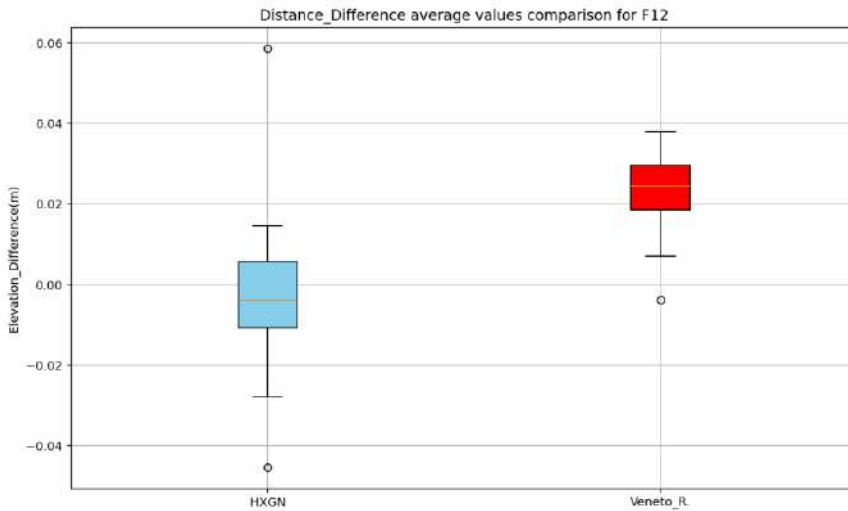


Figure 63: comparison of average values of HXGN and Veneto R. distance difference for F12

### 3.2.5. Elevation difference performance and ranking

Among the datasets evaluated from box plot (figure 64), the HXGN dataset from 28th April ranks 1st overall, offering the best balance of precision and consistency. It has the highest precision (median = 0.0133) and the lowest score (0.01818), indicating strong reliability. Its interquartile range (IQR = 0.015) is moderate, spanning from Q1 = 0.0043 to Q3 = 0.0193, and the whiskers (lower = -0.0182, upper = 0.0418) show a symmetric and controlled spread. The absence of outliers further supports its robustness. The HXGN dataset from 2nd April, ranked 2nd, presents good consistency (IQR = 0.03) and moderate precision (median = -0.0027), with a wide interquartile range (Q1 = -0.0147, Q3 = 0.0153) and whiskers from 0.0603 to 0.0603. Despite the absence of outliers and a favourable score (0.02214), the negative median slightly affects its ranking. The Veneto R. dataset from 9th April, ranked 3rd, shows acceptable precision (median = 0.0003) and moderate consistency (IQR = 0.0245), with a spread from Q1 = -0.0112 to Q3 = 0.0133 and whiskers from -0.04795 to 0.05005. The presence of one outlier and a higher score (0.11748) indicate some variability. Finally, the HXGN dataset from 19th March, ranked last (4th), presents low precision (lowest median = -0.0207) and poorest consistency (widest IQR = 0.0325), with a broad interquartile range (Q1 = -

0.0317, Q3 = 0.0008) and extreme whiskers (lower = -0.08045, upper = 0.04955). The presence of one outlier and a high score (0.12794) reflect reduced reliability.

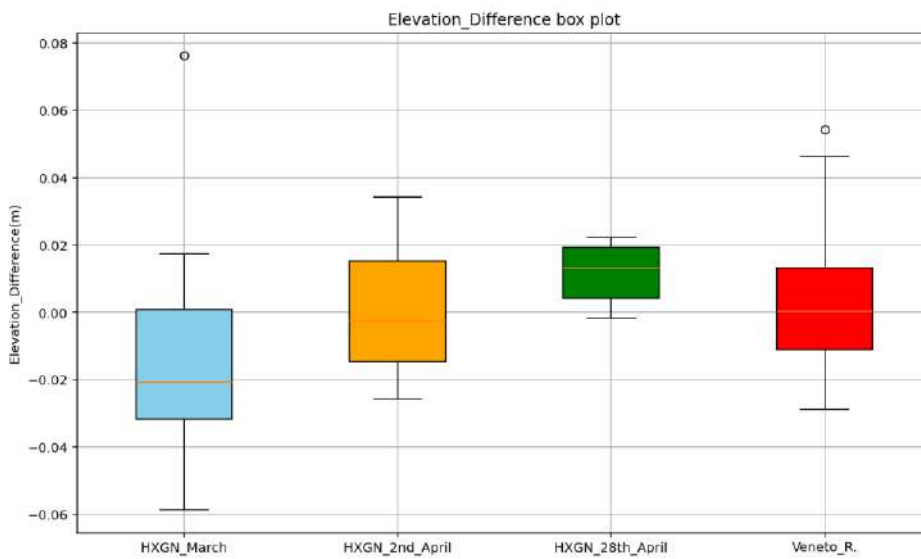


Figure 64: Box plot of distance difference for F32

In this comparison between Veneto R. and HXGN average values (figure 65), the data reveals contrasting characteristics in terms of central tendency and dispersion. Veneto R. has a slightly positive median (0.0003), while HXGN shows a negative median (-0.00645), indicating a downward shift in its core values. HXGN also demonstrates greater variability, with a wider IQR (0.0355 vs. 0.0245) and more extreme whiskers (upper: 0.06456 vs. 0.05005; lower: -0.07745 vs. -0.04795), suggesting a broader and more volatile distribution. Both datasets have one outlier, but HXGN achieves a slightly higher score (0.12614 vs. 0.11748), yet still ranks 2nd globally, behind Veneto R. in 1st place.

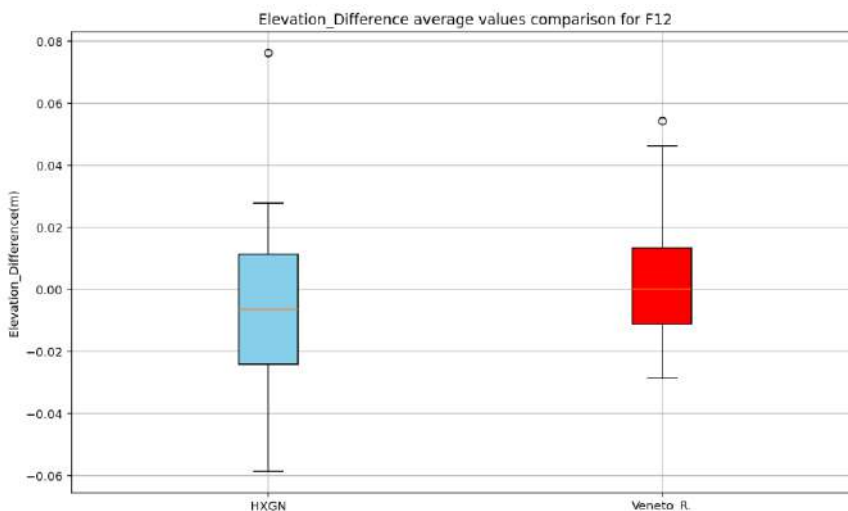


Figure 65: Box plot of elevation difference for F12

### 3.3. Optimization of the utilization of the NRTK network

The most important analyses are related to the differences in distances, and in elevation through F12 referential as it minimizes cartographic deformations. We need to estimate, as best as possible, the distances and differences in elevation between points with minimum acquisition time, to save time and costs of measurements.

Veneto R. achieves its lower distance difference at epochs 360 seconds with an intensity of -0.0007 meter while the HXGN NRTK achieves its lowest distance difference at 5 seconds with an intensity of -0.002366667 meter. Regarding the elevation difference, the Veneto R. reaches its lowest value (0.000698536 meter) at 6 seconds while the HXGN NRTK achieved it at 40 seconds with an intensity of 0.002350576 meter. Thus, the Veneto R. is to one offering the best precision while the time saving is not always optimal. The application of the scalarization technics to Veneto R. distance difference dataset and elevation difference dataset (table 5) shows that optimal epoch that better manage accuracy, deviations and time saving is 7s.

Table 5: Results of scalarization techniques

Epoch	L1 Score	L1 Rank	L2 Score	L2 Rank	L $\infty$ Score	L $\infty$ Rank
7	0.3614	1	0.3614	2	0.3614	2
240	0.3883	2	0.2834	1	0.2437	1
180	0.5910	3	0.5910	5	0.5910	7
420	0.6633	4	0.5751	3	0.5670	6
8	0.8046	5	0.6023	6	0.5422	5
9	0.8093	6	0.5861	4	0.4940	4
600	0.8142	7	0.7140	9	0.7057	12

Epoch	L1 Score	L1 Rank	L2 Score	L2 Rank	L $\infty$ Score	L $\infty$ Rank
480	0.8400	8	0.6525	7	0.6111	8
300	0.9306	9	0.6581	8	0.4728	3
50	0.9510	10	0.9272	18	0.9269	22
360	0.9901	11	0.7348	10	0.6528	9
40	0.9959	12	0.7636	11	0.7067	13
120	1.0436	13	0.8301	14	0.7906	15
10	1.0589	14	0.7759	12	0.6734	11
20	1.0722	15	0.8147	13	0.7469	14
60	1.1420	16	0.9006	16	0.8529	20
30	1.1566	17	1.0122	20	1.0000	23
540	1.2048	18	0.9113	17	0.8313	18
2	1.2198	19	0.8657	15	0.6627	10
5	1.3017	20	0.9553	19	0.8318	19
6	1.4073	21	1.0345	21	0.9036	21

Epoch	L1 Score	L1 Rank	L2 Score	L2 Rank	L $\infty$ Score	L $\infty$ Rank
3	1.5468	22	1.1398	24	1.0000	23
4	1.5551	23	1.1004	22	0.8072	16
1	1.5818	24	1.1188			

#### 4. CONCLUSION

This study evaluated the performance of two NRTK GNSS networks—**Veneto Region NRTK** and **HXGN SmartNet (HXGN)** in Veneto, focusing on positional accuracy, consistency, and optimal observation time. The analysis considered multiple indicators, including CQ metrics (CQ1D, CQ2D, CQ3D), GDOP, and differences in distance and elevation relative to reference measurements obtained through classical topographic methods.

The results demonstrate that **HXGN SmartNet generally provides higher stability and consistency**, with lower median values and fewer outliers across CQ and GDOP metrics. Veneto R., while delivering acceptable performance, exhibited greater variability and occasional extreme deviations, particularly in early epochs and under challenging satellite geometry conditions.

In terms of **distance and elevation differences**, Veneto R. achieved its best precision at 360 seconds for distance (difference of  $-0.0007$  m) and 6 seconds for elevation (difference of  $0.000698536$  m), whereas HXGN reached its minimum distance difference at 5 seconds ( $-0.002366667$  m) and minimum elevation difference at 40 seconds (difference of  $0.002350576$  m). These findings indicate that Veneto R. can offer superior instantaneous precision, but not always with optimal time efficiency.

To identify the best compromise between accuracy and acquisition time, a scalarization approach was applied using three criteria: L1, L2, and L $\infty$  norms. The results indicated that a 7-second epoch represents the optimal setting for the Veneto R.

**Overall, Hexagon HXGN SmartNet stands out as the most consistent and reliable network,** particularly for applications requiring stable performance under varying conditions. Veneto R. remains a strong alternative, especially in scenarios where vertical accuracy is a priority.

Future research should investigate and evaluate performance across diverse environmental conditions. Additionally, expanding the study to other sites within the Veneto Region is recommended, as the current analysis was limited to Padova.

It is worth noting that the Veneto Region NRTK is freely available, with the only requirement being user registration on its website. In contrast, access to the Hexagon HXGN NRTK requires a subscription fee of approximately €500 per year per user. Moreover, the Veneto Region NRTK operates exclusively within the Veneto area, while the Hexagon HXGN SmartNet is international, offering coverage in many countries worldwide—an additional advantage of the Veneto Region NRTK.

## Bibliography

- Alessi, E. M., Schettino, G., Rossi, A., & Valsecchi, G. B. (2018). Solar radiation pressure resonances in Low Earth Orbits. *Monthly Notices of the Royal Astronomical Society*, 473(2), 2407–2414. <https://doi.org/10.1093/mnras/stx2507>
- Barreca, G., Bruno, V., Dardanelli, G., Guglielmino, F., Lo Brutto, M., Mattia, M., Pipitone, C., & Rossi, M. (2020). An integrated geodetic and InSAR technique for the monitoring and detection of active faulting in southwestern Sicily. *Annals of Geophysics*, 63(Vol 63 (2020)). <https://doi.org/10.4401/ag-8327>
- Berber, M., & Arslan, N. (2013). Network RTK: A case study in Florida. *Measurement: Journal of the International Measurement Confederation*, 46(8), 2798–2806. <https://doi.org/10.1016/j.measurement.2013.04.078>
- Biswas, T., Ghosh, S., Paul, A., & Sarkar, S. (2019). Interfrequency Performance Characterizations of GPS During Signal Outages From an Anomaly Crest Location. *Space Weather*, 17(6), 803–815. <https://doi.org/10.1029/2018SW002105>
- Bury, G., Sośnica, K., Zajdel, R., & Strugarek, D. (2020). Toward the 1-cm Galileo orbits: challenges in modeling of perturbing forces. *Journal of Geodesy*, 94(2), 16. <https://doi.org/10.1007/s00190-020-01342-2>
- Cao, L., Chen, H., Chen, Y., Yue, Y., & Zhang, X. (2023). Bio-Inspired Swarm Intelligence Optimization Algorithm-Aided Hybrid TDOA/AOA-Based Localization. *Biomimetics*, 8(2), 186. <https://doi.org/10.3390/biomimetics8020186>
- Căţeanu, M., & Moroianu, M. A. (2024). Performance Evaluation of Real-Time Kinematic Global Navigation Satellite System with Survey-Grade Receivers and Short Observation Times in Forested Areas. *Sensors*, 24(19). <https://doi.org/10.3390/s24196404>
- Chakraborty, S., Ruohoniemi, J. M., Baker, J. B. H., Fiori, R. A. D., Bailey, S. M., & Zawdie, K. A. (2021). Ionospheric Sluggishness: A Characteristic Time-Lag of the Ionospheric Response to Solar Flares. *Journal of Geophysical Research: Space Physics*, 126(4). <https://doi.org/10.1029/2020JA028813>
- Chen, K., Yuan, J., & Luo, X. (2017). Compact dual-band dual circularly polarised annular-ring patch antenna for BeiDou navigation satellite system application. *IET Microwaves, Antennas & Propagation*, 11(8), 1079–1085. <https://doi.org/10.1049/iet-map.2016.1057>
- Chen, W., Tian, Y., Sun, S., & Liu, R. (2023). Safety Assessment for Full Flight between Beidou Radio Determination Satellite Service Airborne Equipment and 5G System. *Electronics*, 12(15), 3350. <https://doi.org/10.3390/electronics12153350>
- Chen, Y., Yuan, Y., Zhang, B., Liu, T., Ding, W., & Ai, Q. (2018). A modified mix-differenced approach for estimating multi-GNSS real-time satellite clock offsets. *GPS Solutions*, 22(3), 72. <https://doi.org/10.1007/s10291-018-0739-5>
- Chieu, V. D., Dung, L. N., Hung, C. V., Quang, V. N., & Son, B. N. (2023). Study on the application of TLS for bridge deflection inspection in Vietnam. *Journal of Science and Technology in Civil Engineering (STCE) - HUCE*, 17(4), 14–25. [https://doi.org/10.31814/stce.huce2023-17\(4\)-02](https://doi.org/10.31814/stce.huce2023-17(4)-02)
- Dardanelli, G., & Maltese, A. (2022). On the Accuracy of Cadastral Marks: Statistical Analyses to Assess the Congruence among GNSS-Based Positioning and Official Maps. *Remote Sensing*, 14(16), 4086. <https://doi.org/10.3390/rs14164086>

- Dunn, P. K., Powierski, A. P., & Hill, R. (2006). Statistical evaluation of data from tractor guidance systems. *Precision Agriculture*, 7(3), 179–192. <https://doi.org/10.1007/s11119-006-9007-8>
- El-Mowafy, A. (2018). Real-Time Precise Point Positioning Using Orbit and Clock Corrections as Quasi-Observations for Improved Detection of Faults. *Journal of Navigation*, 71(4), 769–787. <https://doi.org/10.1017/S0373463317001023>
- Esenbuğa, Ö. G., & Hauschild, A. (2020). Impact of flex power on GPS Block IIF differential code biases. *GPS Solutions*, 24(4), 91. <https://doi.org/10.1007/s10291-020-00996-x>
- Fabris, M., & Floris, M. (2025). Integrated GNSS and InSAR Analysis for Monitoring the Shoulder Structures of the MOSE System in Venice, Italy. *Remote Sensing*, 17(6). <https://doi.org/10.3390/rs17061059>
- Farah, A. (2018). Nequick2 model behaviour for global ionospheric delay mitigation during solar cycle-24. *Artificial Satellites*, 53(4), 127–139. <https://doi.org/10.2478/arsa-2018-0010>
- Farah, A. (2020). Behavior of Broadcast Ionospheric-Delay Models from GPS, Beidou, and Galileo Systems. *Artificial Satellites*, 55(2), 61–76. <https://doi.org/10.2478/arsa-2020-0005>
- Felski, A. (2022). Measuring the Speed of Docking Ship with Total Station. *Communications - Scientific Letters of the University of Zilina*, 24(1), E1–E10. <https://doi.org/10.26552/com.C.2022.1.E1-E10>
- Feng, Y., & Wang, J. (2008). GPS RTK Performance Characteristics and Analysis. In *Journal of Global Positioning Systems* (Vol. 7, Issue 1).
- Giagkiozis, I., & Fleming, P. J. (2015). Methods for multi-objective optimization: An analysis. *Information Sciences*, 293, 338–350. <https://doi.org/10.1016/j.ins.2014.08.071>
- Glavačević, K., Marić, I., Domazetović, F., Šiljeg, A., Pedić, G., Jurjević, L., & Panda, L. (2025). Applicability of network real time kinematic (NRTK) approach in soil erosion measurement at different temporal and spatial scales. *Applied Geomatics*. <https://doi.org/10.1007/s12518-025-00612-y>
- Google. (2025). *Google Earth Pro*.
- Gu, Y., Wada, Y., Hsu, L.-T., & Kamijo, S. (2016). SLAM with 3Dimensional-GNSS. *2016 IEEE/ION Position, Location and Navigation Symposium (PLANS)*, 190–197. <https://doi.org/10.1109/PLANS.2016.7479701>
- Guan, X., Xu, Y., & Xing, C. (2021). A Method for Rapid Measurement of the Deformation and Spatial Attitude of Large Radar Antennas Inside Radomes. *IEEE Access*, 9, 64686–64695. <https://doi.org/10.1109/ACCESS.2021.3076000>
- Gümüş, K., & Selbesoğlu, M. O. (2019). Evaluation of NRTK GNSS positioning methods for displacement detection by a newly designed displacement monitoring system. *Measurement: Journal of the International Measurement Confederation*, 142, 131–137. <https://doi.org/10.1016/j.measurement.2019.04.041>
- GÜNDÜZ, N., & BULUT, A. S. (2017). Öğretmen Adaylarının Geometrik Cisimler Konusundaki Bilgi Düzeyleri, Problem Çözme Düzeyleri ve Tutumlarının İncelenmesi. *İnönü Üniversitesi Eğitim Fakültesi Dergisi*, 1–1. <https://doi.org/10.17679/inuefd.323363>
- Guochang Xu. (2007). *GPS* (2nd ed.). Springer Berlin Heidelberg. <https://doi.org/10.1007/978-3-540-72715-6>

- Hoi, T. Van, Lanh, N. T., Truong, N. X., Duc, N. H., & Duong, B. G. (2016). Design of a Front-End for Satellite Receiver. *International Journal of Electrical and Computer Engineering (IJECE)*, 6(5), 2282. <https://doi.org/10.11591/ijece.v6i5.pp2282-2290>
- Hsu, L.-T., Gu, Y., Huang, Y., & Kamijo, S. (2016). Urban Pedestrian Navigation Using Smartphone-Based Dead Reckoning and 3-D Map-Aided GNSS. *IEEE Sensors Journal*, 16(5), 1281–1293. <https://doi.org/10.1109/JSEN.2015.2496621>
- Huang, J., Li, X., Li, X., Wu, J., Zhang, K., Yuan, Y., & Zhang, W. (2025). Real-time outlier detection of satellite orbit and clock products using reverse error estimation. *GPS Solutions*, 29(1), 2. <https://doi.org/10.1007/s10291-024-01753-0>
- Hugentobler, U., & Montenbruck, O. (2017). Satellite Orbits and Attitude. In *Springer Handbook of Global Navigation Satellite Systems* (pp. 59–90). Springer International Publishing. [https://doi.org/10.1007/978-3-319-42928-1\\_3](https://doi.org/10.1007/978-3-319-42928-1_3)
- Im, S. B., Hurlebaus, S., & Kang, Y. J. (2013). Summary Review of GPS Technology for Structural Health Monitoring. *Journal of Structural Engineering*, 139(10), 1653–1664. [https://doi.org/10.1061/\(ASCE\)ST.1943-541X.0000475](https://doi.org/10.1061/(ASCE)ST.1943-541X.0000475)
- Imad, M., Grenier, A., Zhang, X., Nurmi, J., & Lohan, E. (2023). Ionospheric Error Models for Satellite-Based Navigation—Paving the Road towards LEO-PNT Solutions. *Computers*, 13(1), 4. <https://doi.org/10.3390/computers13010004>
- Jamieson, M., & Gillins, D. T. (2018). Comparative Analysis of Online Static GNSS Postprocessing Services. *Journal of Surveying Engineering*, 144(4). [https://doi.org/10.1061/\(ASCE\)SU.1943-5428.0000256](https://doi.org/10.1061/(ASCE)SU.1943-5428.0000256)
- Janicka, J., Tomaszewski, D., Rapinski, J., Jagoda, M., & Rutkowska, M. (2020). The Prediction of Geocentric Corrections during Communication Link Outages in PPP. *Sensors*, 20(3), 602. <https://doi.org/10.3390/s20030602>
- Janssen, V. (2009). *International Global Navigation Satellite Systems Society IGNSS Symposium*.
- Janssen, V., & Haasdyk, J. (2011). *International Global Navigation Satellite Systems Society IGNSS Symposium*.
- Jeong, G.-S., & Kong, S.-H. (2015). Pseudo-Correlation-Function Based Unambiguous Tracking Technique for CBOC (6,1,1/11) Signals. *Journal of Positioning, Navigation, and Timing*, 4(3), 107–114. <https://doi.org/10.11003/JPNT.2015.4.3.107>
- Ji, G., Shin, H., & Won, J. (2021). Analysis of multi-constellation GNSS receiver performance utilizing 1st side-lobe signal on the use of SSV for KPS satellites. *IET Radar, Sonar & Navigation*, 15(5), 485–499. <https://doi.org/10.1049/rsn2.12052>
- Jiang, Y., & Li, W. (2022). *An Efficient Fault Detection and Exclusion Method for Ephemeris Monitoring*. <https://doi.org/10.21203/rs.3.rs-1904859/v1>
- Joseph, A. (2011). Sea-Level Measurements From Coasts and Islands. In *Tsunamis* (pp. 253–332). Elsevier. <https://doi.org/10.1016/B978-0-12-385053-9.10016-X>
- Kalooop, M. R., Yigit, C. O., El-Mowafy, A., Dindar, A. A., Bezcioglu, M., & Hu, J. W. (2019). Hybrid Wavelet and Principal Component Analyses Approach for Extracting Dynamic Motion Characteristics from Displacement Series Derived from Multipath-Affected High-Rate GNSS Observations. *Remote Sensing*, 12(1), 79. <https://doi.org/10.3390/rs12010079>

- Keshavarzi, H., Lee, C., Johnson, M., Abbott, D., Ni, W., & Campbell, D. L. M. (2021). Validation of Real-Time Kinematic (RTK) Devices on Sheep to Detect Grazing Movement Leaders and Social Networks in Merino Ewes. *Sensors*, 21(3), 924. <https://doi.org/10.3390/s21030924>
- Kim, H., Yun, H., Hwang, J., & Hong, S. (2017). A Static Displacement Monitoring System for VLBI Antenna Using Close-Range Photogrammetry. *Applied Sciences*, 7(11), 1125. <https://doi.org/10.3390/app7111125>
- Kizil, U., & Tisor, L. (2011). Evaluation of RTK-GPS and Total Station for applications in land surveying. *Journal of Earth System Science*, 120(2), 215–221. <https://doi.org/10.1007/s12040-011-0044-y>
- Kovář, P. (2020). Start Acceleration of the Space GPS Receiver. *International Journal of Electronics and Telecommunications*, 745–752. <https://doi.org/10.24425/ijet.2020.134036>
- Lau, L. (2021). GNSS multipath errors and mitigation techniques. In *GPS and GNSS Technology in Geosciences* (pp. 77–98). Elsevier. <https://doi.org/10.1016/B978-0-12-818617-6.00009-3>
- Leclère, J., & Landry, R. (2019). Galileo E5 Signal Acquisition using Intermediate Coherent Integration Time. *Journal of Navigation*, 72(3), 555–574. <https://doi.org/10.1017/S0373463318001054>
- Leica geosystems. (2021). *Rover GNSS Leica Viva GS16*. Leica Viva GS16 Data Sheet.
- Li, H., & Li, X. (2025). Fast estimation and timely service of the GNSS satellite clock errors for support of 1 Hz real-time precise point positioning applications. *Journal of Geodesy*, 99(7), 58. <https://doi.org/10.1007/s00190-025-01985-z>
- Li, W., Rius, A., Fabra, F., Martín-Neira, M., Cardellach, E., Ribó, S., & Yang, D. (2016). The Impact of Inter-Modulation Components on Interferometric GNSS-Reflectometry. *Remote Sensing*, 8(12), 1013. <https://doi.org/10.3390/rs8121013>
- Li, X., Han, J., Li, X., Huang, J., Shen, Z., & Wu, Z. (2023). A grid-based ionospheric weighted method for PPP-RTK with diverse network scales and ionospheric activity levels. *GPS Solutions*, 27(4), 191. <https://doi.org/10.1007/s10291-023-01522-5>
- Li, Y., Huang, J., Jiang, S.-H., Huang, F., & Chang, Z. (2017). A web-based GPS system for displacement monitoring and failure mechanism analysis of reservoir landslide. *Scientific Reports*, 7(1), 17171. <https://doi.org/10.1038/s41598-017-17507-7>
- Lösler, M., Eschelbach, C., Mähler, S., Guillory, J., Truong, D., & Wallerand, J.-P. (2023). Operator-software impact in local tie networks. *Applied Geomatics*, 15(1), 77–95. <https://doi.org/10.1007/s12518-022-00477-5>
- Lubeigt, C., Ortega, L., Vilà-Valls, J., Lestarquit, L., & Chaumette, E. (2021). On the Impact and Mitigation of Signal Crosstalk in Ground-Based and Low Altitude Airborne GNSS-R. *Remote Sensing*, 13(6), 1085. <https://doi.org/10.3390/rs13061085>
- Luo, Y., Chen, J., Xi, W., Zhao, P., Qiao, X., Deng, X., & Liu, Q. (2016). Analysis of tunnel displacement accuracy with total station. *Measurement*, 83, 29–37. <https://doi.org/10.1016/j.measurement.2016.01.025>
- Maciuk, K. (2018). GPS-only, GLONASS-only and Combined GPS+GLONASS Absolute Positioning under Different Sky View Conditions. *Tehnicki Vjesnik - Technical Gazette*, 25(3). <https://doi.org/10.17559/TV-20170411124329>

- Mansur, G. B., & Ferreira, L. D. D. (2019). ERROR BEHAVIOR OF ATOMIC CLOCKS ABOARD GPS SATELLITES. *Boletim de Ciências Geodésicas*, 25(4). <https://doi.org/10.1590/s1982-21702019000400027>
- Marhoon, H. M., Basil, N., & Abdalnabi, H. A. (2023). *IoT-Based Low-Cost Children Tracker System*. <https://doi.org/10.21203/rs.3.rs-2476137/v1>
- Matonti, F., Miller, A., & Wnuk, J. (2025). *ITRF2020 usage and maintenance in a global dense network for commercial applications*. <https://doi.org/10.5194/egusphere-egu24-16881>
- Matonti, F., Wnuk, J., & Miller, A. (2025, March 15). Updating a large and dense GNSS Network to ITRF2020-u2023. *EGU General Assembly 2025*. <https://doi.org/10.5194/egusphere-egu25-16128>
- Murray, J. R., & Svarc, J. (2017). Global Positioning System Data Collection, Processing, and Analysis Conducted by the U.S. Geological Survey Earthquake Hazards Program. *Seismological Research Letters*, 88(3), 916–925. <https://doi.org/10.1785/0220160204>
- NGUYEN, H. D. Q., PHAM, Q. N., TRAN, V. D., NGUYEN, Q. L., & NGUYEN, T. G. (2025). Application of Outlier Detection Methods in GNSS Time Series Analysis. *Inżynieria Mineralna*, 3(2). <https://doi.org/10.29227/IM-2024-02-95>
- Panetier, A., Bossier, P., & Khenchaf, A. (2023). Sensitivity of Shipborne GNSS Estimates to Processing Modeling Based on Simulated Dataset. *Sensors*, 23(14), 6605. <https://doi.org/10.3390/s23146605>
- Park, S. G., Cho, D. J., & Park, C. (2012). Carrier Phase Based Navigation Algorithm Design Using Carrier Phase Statistics in the Weak Signal Environment. *Journal of Positioning, Navigation, and Timing*, 1(1), 7–14. <https://doi.org/10.11003/JKGS.2012.1.1.007>
- Paziewski, J. (2020). Recent advances and perspectives for positioning and applications with smartphone GNSS observations. *Measurement Science and Technology*, 31(9), 091001. <https://doi.org/10.1088/1361-6501/ab8a7d>
- Pesce, V., Hermosin, P., Rivolta, A., Bhaskaran, S., Silvestrini, S., & Colagrossi, A. (2022). Navigation. In *Modern Spacecraft Guidance, Navigation, and Control: From System Modeling to AI and Innovative Applications* (pp. 441–542). Elsevier. <https://doi.org/10.1016/B978-0-323-90916-7.00009-3>
- Pintor, P., Lopez-Martinez, M., Gonzalez, E., Safar, J., & Boyle, R. (2023). Testing Galileo High-Accuracy Service (HAS) in Marine Operations. *Journal of Marine Science and Engineering*, 11(12), 2375. <https://doi.org/10.3390/jmse11122375>
- Pipitone, C., Maltese, A., Lo Brutto, M., & Dardanelli, G. (2023). A Review of Selected Applications of GNSS CORS and Related Experiences at the University of Palermo (Italy). In *Remote Sensing* (Vol. 15, Issue 22). Multidisciplinary Digital Publishing Institute (MDPI). <https://doi.org/10.3390/rs15225343>
- Pirsiavash, A., Broumandan, A., Lachapelle, G., & O'Keefe, K. (2018). GNSS Code Multipath Mitigation by Cascading Measurement Monitoring Techniques. *Sensors*, 18(6), 1967. <https://doi.org/10.3390/s18061967>
- Pratiwi, N., Herdiwijaya, D., Ahmad, N., Hidayat, T., & Ikhsan, M. I. (2025). *Modeling of BRIsat Orbital Parameters Due to Solar Radiation Pressure* (pp. 170–178). [https://doi.org/10.1007/978-981-96-1344-1\\_18](https://doi.org/10.1007/978-981-96-1344-1_18)

- Pratiwi, N., Herdiwijaya, D., Hidayat, T., & Ikhsan, M. I. (2024). Comparison of the SRP spherical model between LEO and GEO satellites. *Journal of Physics: Conference Series*, 2734(1), 012012. <https://doi.org/10.1088/1742-6596/2734/1/012012>
- Qi, J., Chen, J., & Geng, Y. (2014). Unambiguous Synchronization Scheme for GNSS BOC(n,n) Signals. *Journal of Networks*, 9(8). <https://doi.org/10.4304/jnw.9.8.2224-2231>
- Quan, Y., Lau, L., Roberts, G. W., Meng, X., & Zhang, C. (2018). Convolutional Neural Network Based Multipath Detection Method for Static and Kinematic GPS High Precision Positioning. *Remote Sensing*, 10(12), 2052. <https://doi.org/10.3390/rs10122052>
- Radicioni, F., Stoppini, A., Tosi, G., & Marconi, L. (2022). Multi-constellation Network RTK for Automatic Guidance in Precision Agriculture. *2022 IEEE Workshop on Metrology for Agriculture and Forestry (MetroAgriFor)*, 260–265. <https://doi.org/10.1109/MetroAgriFor55389.2022.9965046>
- Revert Calabuig, N., Laarossi, I., Álvarez González, A., Pérez Nuñez, A., González Pérez, L., & García-Minguillán, A. C. (2023). Development of a Low-Cost Smart Sensor GNSS System for Real-Time Positioning and Orientation for Floating Offshore Wind Platform. *Sensors*, 23(2), 925. <https://doi.org/10.3390/s23020925>
- Rosengren, A. J., Alessi, E. M., Rossi, A., & Valsecchi, G. B. (2015). Chaos in navigation satellite orbits caused by the perturbed motion of the Moon. *Monthly Notices of the Royal Astronomical Society*, 449(4), 3522–3526. <https://doi.org/10.1093/mnras/stv534>
- Rysbekov, K., Huayang, D., Kalybekov, T., Sandybekov, M., Idrissov, K., Zhakypbek, Y., & Bakhmagambetova, G. (2019). Application features of the surface laser scanning technology when solving the main tasks of surveying support for reclamation. *Mining of Mineral Deposits*, 13(3), 40–48. <https://doi.org/10.33271/mining13.03.040>
- Sánchez, L., & Brunini, C. (2009). *Achievements and Challenges of SIRGAS* (pp. 161–166). [https://doi.org/10.1007/978-3-642-00860-3\\_25](https://doi.org/10.1007/978-3-642-00860-3_25)
- Schmölter, E., Berdermann, J., Jakowski, N., Jacobi, C., & Vaishnav, R. (2018). Delayed response of the ionosphere to solar EUV variability. *Advances in Radio Science*, 16, 149–155. <https://doi.org/10.5194/ars-16-149-2018>
- Setti, P. T., da Silva, C. M., & Alves, D. B. M. (2025). Assessing GNSS ionospheric models at low latitudes: BDGIM, NeQuick-G, and Klobuchar. *GPS Solutions*, 29(1). <https://doi.org/10.1007/s10291-024-01761-0>
- Shim, D.-S., & Jeon, J.-S. (2018). An Unambiguous Delay-And-Multiply Acquisition Scheme for GPS L1C Signals. *Sensors*, 18(6), 1739. <https://doi.org/10.3390/s18061739>
- Šiaudinytė, L., & Grattan, K. T. V. (2016). Uncertainty evaluation of trigonometric method for vertical angle calibration of the total station instrument. *Measurement*, 86, 276–282. <https://doi.org/10.1016/j.measurement.2015.10.037>
- Sofos, I., Vescoukis, V., & Tsakiri, M. (2017). VGI in surveying engineering: Introducing collaborative cloud land surveying. *Journal of Spatial Information Science*, 15. <https://doi.org/10.5311/JOSIS.2017.15.320>

- Sośnica, K., Bury, G., Zajdel, R., Kazmierski, K., Ventura-Traveset, J., Prieto-Cerdeira, R., & Mendes, L. (2021). General relativistic effects acting on the orbits of Galileo satellites. *Celestial Mechanics and Dynamical Astronomy*, 133(4), 14. <https://doi.org/10.1007/s10569-021-10014-y>
- Sun, L., Huang, W., Gao, S., Li, W., Guo, X., & Yang, J. (2020). Joint Timekeeping of Navigation Satellite Constellation with Inter-Satellite Links. *Sensors*, 20(3), 670. <https://doi.org/10.3390/s20030670>
- Suzuki, T. (2019). Mobile robot localization with GNSS multipath detection using pseudorange residuals. *Advanced Robotics*, 33(12), 602–613. <https://doi.org/10.1080/01691864.2019.1619622>
- Tao Zeng, Dongyang Ao, Cheng Hu, Tian Zhang, Feifeng Liu, Weiming Tian, & Kuan Lin. (2015). Multiangle BSAR Imaging Based on BeiDou-2 Navigation Satellite System: Experiments and Preliminary Results. *IEEE Transactions on Geoscience and Remote Sensing*, 53(10), 5760–5773. <https://doi.org/10.1109/TGRS.2015.2430312>
- Tavasci, L., Nex, F., & Gandolfi, S. (2024). Reliability of Real-Time Kinematic (RTK) Positioning for Low-Cost Drones' Navigation across Global Navigation Satellite System (GNSS) Critical Environments. *Sensors*, 24(18), 6096. <https://doi.org/10.3390/s24186096>
- Teunissen, P. J. G. (2019). A new GLONASS FDMA model. *GPS Solutions*, 23(4), 100. <https://doi.org/10.1007/s10291-019-0889-0>
- Thoelert, S., Antreich, F., Enneking, C., & Meurer, M. (2019). *BeiDou 3 Signal Quality Analysis and its Impact on Users*. 909–924. <https://doi.org/10.33012/2019.16738>
- Unipd, CISAS 'G. Colombo,' & Regione del Veneto. (2008). *RETE DELLE STAZIONI PERMANENTI GPS NEL TERRITORIO DEL VENETO*.
- Vaishnav, R., Jacobi, C., Berdermann, J., Codrescu, M., & Schmölder, E. (2021). Role of eddy diffusion in the delayed ionospheric response to solar flux changes. *Annales Geophysicae*, 39(4), 641–655. <https://doi.org/10.5194/angeo-39-641-2021>
- Valente, D. S. M., Momin, A., Grift, T., & Hansen, A. (2020). Accuracy and precision evaluation of two low-cost RTK global navigation satellite systems. *Computers and Electronics in Agriculture*, 168. <https://doi.org/10.1016/j.compag.2019.105142>
- VENETO.INFO. (2025, May 7). *Mappa Veneto*.
- Walter, T. (2017). Satellite Based Augmentation Systems. In *Springer Handbook of Global Navigation Satellite Systems* (pp. 339–361). Springer International Publishing. [https://doi.org/10.1007/978-3-319-42928-1\\_12](https://doi.org/10.1007/978-3-319-42928-1_12)
- Wang, A., Chen, J., Zhang, Y., Wang, J., & Wang, B. (2019). Performance Evaluation of the CNAV Broadcast Ephemeris. *Journal of Navigation*, 72(5), 1331–1344. <https://doi.org/10.1017/S037346331900016X>
- Wang, Y., & Shen, J. (2024). *A Study on SBAS-RTK Integrated Positioning Technologies* (pp. 3–12). [https://doi.org/10.1007/978-981-99-6932-6\\_1](https://doi.org/10.1007/978-981-99-6932-6_1)
- Wanninger, L. (2003). Virtual reference stations (VRS). *GPS Solutions*, 7(2), 143–144. <https://doi.org/10.1007/s10291-003-0060-8>

- Wardhani, I. S., Nusantara, T., Parta, I. N., & Permadi, H. (2023). The Model of Geometry Learning With Spatial Skills Features: Is It Possible? *Journal of Higher Education Theory and Practice*, 23(14). <https://doi.org/10.33423/jhetp.v23i14.6397>
- Wulansari, M., Maulida, P., & Muslim, B. (2023). Ionospheric Disturbance in Indonesia during Solar Flare using GPS Observations. *IOP Conference Series: Earth and Environmental Science*, 1276(1). <https://doi.org/10.1088/1755-1315/1276/1/012019>
- Xi, R., Chen, Q., Meng, X., Jiang, W., An, X., & He, Q. (2020). A Multi-GNSS Differential Phase Kinematic Post-Processing Method. *Remote Sensing*, 12(17), 2727. <https://doi.org/10.3390/rs12172727>
- Yan, Z., Zhao, K., Li, W., Kang, C., Zheng, J., Yang, H., & Du, S. (2022). Topology Design for GNSSs Under Polling Mechanism Considering Both Inter-Satellite Links and Ground-Satellite Links. *IEEE Transactions on Vehicular Technology*, 71(2), 2084–2097. <https://doi.org/10.1109/TVT.2021.3135563>
- Yeh, T.-K., Hwang, C., Xu, G., Wang, C.-S., & Lee, C.-C. (2009). Determination of global positioning system (GPS) receiver clock errors: impact on positioning accuracy. *Measurement Science and Technology*, 20(7), 075105. <https://doi.org/10.1088/0957-0233/20/7/075105>
- Yu, F., Tong, J., Peng, Y., Chen, L., & Wang, S. (2023). A Case Study on the Application of 3D Scanning Technology in Deformation Monitoring of Slope Stabilization Structure. *Buildings*, 13(7), 1589. <https://doi.org/10.3390/buildings13071589>
- Yu, J., & Wang, G. (2017). Introduction to the GNSS geodetic infrastructure in the Gulf of Mexico Region. *Survey Review*, 49(352), 51–65. <https://doi.org/10.1080/00396265.2015.1108069>
- Yu, J., Yan, B., Meng, X., Shao, X., & Ye, H. (2016). Measurement of Bridge Dynamic Responses Using Network-Based Real-Time Kinematic GNSS Technique. *Journal of Surveying Engineering*, 142(3). [https://doi.org/10.1061/\(ASCE\)SU.1943-5428.0000167](https://doi.org/10.1061/(ASCE)SU.1943-5428.0000167)
- Yu, S., & Liu, Z. (2021). Tropical cyclone-induced periodical positioning disturbances during the 2017 Hato in the Hong Kong region. *GPS Solutions*, 25(3), 109. <https://doi.org/10.1007/s10291-021-01112-3>
- Yue, Z., Sun, H., Zhong, R., & Du, L. (2021). Method for Tunnel Displacements Calculation Based on Mobile Tunnel Monitoring System. *Sensors*, 21(13), 4407. <https://doi.org/10.3390/s21134407>
- Zaminpardaz, S., Teunissen, P. J. G., & Khodabandeh, A. (2021). GLONASS-only FDMA+CDMA RTK: Performance and outlook. *GPS Solutions*, 25(3), 96. <https://doi.org/10.1007/s10291-021-01132-z>
- Zhang, H., Zhao, J., Yu, J., Yu, R., Liu, W., Wang, D., & Liu, D. (2023a). Performance Analysis of Beidou Precise independent point location considering ISB parameters in complex Transmission Line Environment. *Journal of Physics: Conference Series*, 2503(1), 012052. <https://doi.org/10.1088/1742-6596/2503/1/012052>
- Zhang, H., Zhao, J., Yu, J., Yu, R., Liu, W., Wang, D., & Liu, D. (2023b). Performance Analysis of Beidou Precise independent point location considering ISB parameters in complex Transmission Line Environment. *Journal of Physics: Conference Series*, 2503(1), 012052. <https://doi.org/10.1088/1742-6596/2503/1/012052>
- Zhang, W., Zhang, J., Zuo, X., Li, H., Pan, G., & Wang, J. (2025). New data processing methods for network RTK positioning: improving ionospheric uncertainty management during ionospheric scintillations. *GPS Solutions*, 29(2), 72. <https://doi.org/10.1007/s10291-025-01832-w>

Zhou, M., Liu, X., Guo, J., Zhang, Q., Liu, Z., Ji, B., & Ouyang, Y. (2020). Epoch-by-epoch phase difference method to evaluate GNSS single-frequency phase data quality. *Revista Internacional de Métodos Numéricos Para Cálculo y Diseño En Ingeniería*, 36.  
<https://doi.org/10.23967/j.rimni.2020.09.003>

Zuo, W., Guo, C., Liu, J., Peng, X., & Yang, M. (2018). A Police and Insurance Joint Management System Based on High Precision BDS/GPS Positioning. *Sensors*, 18(1), 169.  
<https://doi.org/10.3390/s18010169>